



**Politecnico di Torino**

---

FACOLTÀ DI INGEGNERIA

Corso di Laurea Magistrale in Ingegneria Matematica

Master course in Mathematical Engineering

MASTER'S THESIS

**Modeling the multi-scale behavior of active clays using the  
Discrete Element Method (DEM)**

Candidate:

**Paolo Rapino**

Supervisor:

**Prof. Guido Musso**

Research supervisor:

**Prof. Vanessa Magnanimo**



# Contents

<b>Introduction</b>	<b>I</b>
<b>1 Mechanical behaviour of active clays</b>	<b>1</b>
1.1 Mineralogy . . . . .	1
1.1.1 The 1:1 structure . . . . .	4
1.1.2 The 2:1 structure . . . . .	4
1.2 Ion distributions in clay-water systems: double-layer theory . . . . .	7
1.2.1 Mathematical description . . . . .	7
1.3 Evidences of the influence of the pore fluid chemistry on the mechanical behaviour of active clays . . . . .	9
1.3.1 Remoduled bentonite . . . . .	10
1.3.2 Compacted bentonite . . . . .	13
<b>2 Discrete Element Method DEM</b>	<b>17</b>
2.1 Granular materials and DEM . . . . .	17
2.2 Soft-Particle Discrete Element Method . . . . .	19
2.2.1 Linear Normal Contact Model . . . . .	20
2.2.2 Adhesive, Elasto-Plastic Normal Contact Model . . . . .	21
<b>3 Clusters</b>	<b>23</b>
3.1 Creation of a single cluster . . . . .	24
3.2 One dimensional compression for a single cluster . . . . .	27
3.2.1 Study of size effects . . . . .	29
3.2.2 Strain rate effect . . . . .	29
3.3 Workable characteristics . . . . .	31
<b>4 Mechanical loading</b>	<b>34</b>
4.1 Parameter calibration . . . . .	34
4.2 Single porosity: preliminary study . . . . .	38
4.2.1 Numerical simulation . . . . .	41
4.3 Compression of clusters with water-like fluid . . . . .	47
4.3.1 Numerical simulation . . . . .	49
4.3.2 Results analysis . . . . .	55
4.4 Validation: compression of clusters with salt water-like fluid . . . . .	55
<b>5 Chemical loading</b>	<b>61</b>
5.1 Single chemical load . . . . .	62
5.2 Chemical loading cycle on normal consolidated samples . . . . .	65
5.3 Chemical loading cycle on overconsolidated samples . . . . .	69

5.4 Comparison of different numerical and chemical loading paths . . .	72
<b>6 Conclusions and future work</b>	<b>80</b>
<b>A MercuryDPM</b>	<b>81</b>
A.1 Software overview . . . . .	81
A.2 Implementation of the cluster creation process inside MercuryDPM	84
<b>B GrainLearning toolbox</b>	<b>86</b>
<b>Bibliography</b>	<b>88</b>
<b>Acknowledgements</b>	<b>89</b>

# Introduction

Granular materials, i.e. agglomerations of discrete, macroscopic particles, are omnipresent in both industry and nature. They range from natural materials like snow, sand, soil, coffee, rice and coal to artificial materials such as medicinal tablets, catalysts or animal feed: they are, indeed, the second most manipulated raw materials after water. Furthermore, they are involved in physical phenomena like sandstorms, avalanches and earthquakes, concerning respectively sand, snow and soil. The distinction between granular materials and fine particulates (or molecules) is obviously made taking into account the size of their constituent particles: the constituents that compose granular material must be large enough such that their movement is not subject to thermal fluctuations. Thus, the lower size limit for granular materials can be defined as  $1\mu m$ . On the other hand, there is no upper size limit, considering that the physics of granular materials have been applied to the formation of solar systems, galaxies and the universe. When studying this kind of matter, the massively high number of degrees of freedom takes to wildly non-linear behaviour. For this reason, it is quite challenging to characterize such materials with a continuum mechanics approach (for example Finite element method, FEM): considering a continuum model, indeed, movements and rotations of particles inside the material are not considered; thus, in order to capture its micro-mechanical behaviour, it is needed to couple the model with complex contact laws. Differently, when using Discrete Element Method (DEM) this is not needed and capturing the micro-mechanical behaviour of those materials is quite easy. For this reason throughout this study DEM has been used in order to simulate the changes to the micro- and macro-scale of active clays, when mechanical loads are applied to a sample. Furthermore, given the good results obtained when simulating experimental tests of uniaxial compression, chemical loads have been simulated, with particular stress on the relation between micro- and macro-porosity.

# Chapter 1

## Mechanical behaviour of active clays

When taking into account the mechanical behaviour of active clays many are the factors that play an important role in its characterization: clays are in fact composed by solid particles, liquid and gas; furthermore particles are very small in size, given that the upper size limit is  $d = 2\mu m$  and in order to see them it is necessary the aid of the electron microscope. Particle shapes also vary with a wide range going from nearly spherical, bulky grains to thin, flat plates and long streamlined needles. Finally, also the chemical composition needs to be considered as humidity and short range chemical interactions can make a significant difference in the mechanical response of clays. Mineralogy is the primary factor controlling all of this characteristics and a knowledge of the role of minerals in a soil provides an intuitive insight of its behavior. For this reasons in this chapter clays mineralogy and the role of chemical interactions will be discussed, before characterising the mechanical behaviour of active clays.

### 1.1 Mineralogy

Clay minerals in soils belong to the mineral family termed phyllosilicates. This family also contains other layer silicates such as serpentine, pyrophyllite, talc, mica, and chlorite. One important property of this kind of soil is that its particles have a residual negative charge that is balanced by the adsorption of cations from solution. Regarding their structure it consists in combinations of simple structural units, which could be for example silicon tetrahedron with the aluminum or magnesium octahedron, both defined below. What characterises each mineral group is the stacking of these sheets or units and the way in which two successive two- or three-sheet layers are held together; therefore in order to properly characterize clay minerals it is necessary to define the sheets that can compose them.

#### **Silica Sheet**

The silica structure is formed by multiple interconnected tetrahedral units. In figure 1.1 the way multiple silica tetrahedra are assembled is displayed: by

shearing three oxygens out of the four of which they are composed, an hexagonal net is formed. This structure is based on a single plane and for this reason the only oxygen which is not shared in each tetrahedron points in the same direction, i.e. perpendicularly to the base plane. There is no limit to the repetition of this scheme.

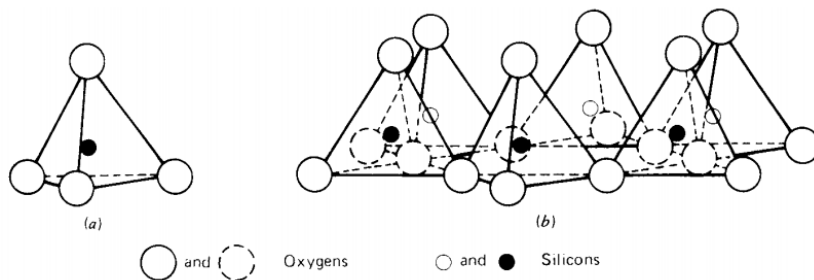


**Figure 1.1:** Silicon tetrahedron and silica tetrahedra arranged in a hexagonal network [8].

### Octahedral Sheet

As can be seen in figure 1.2 (a), the octahedral unit is composed by six oxygens or hydroxyls and one aluminium or magnesium. When composed by a trivalent cation, such as aluminium, the octahedral structure in figure 1.2 (b) forms the mineral called gibbsite which is called gibbsite sheet if united with silica sheets. Coherently, when composed by a divalent cation, for example magnesium, the octahedral structure forms the mineral called brucite which is called brucite sheet if united with silica sheets.

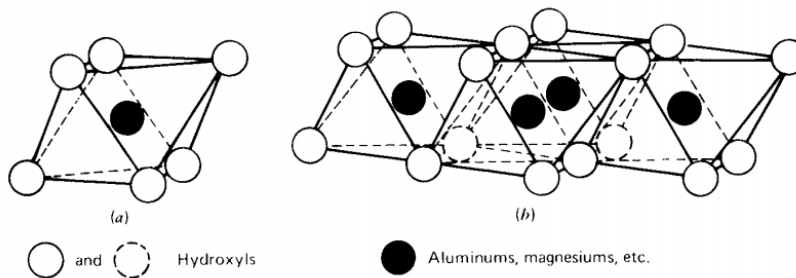


**Figure 1.2:** Octahedral unit and sheet structure of octahedral units [8].

### Pattern and classification of the clay minerals

A simple representation of the schemes discussed above is shown in figure 1.3: it is important to notice that this kind of visualization is useful in order to understand the structure obtained, but it is not reliable when considering the relative size between sheets. Furthermore, the picture shows an idealized structure: in reality minerals are characterized by substitutions and mixed-layer

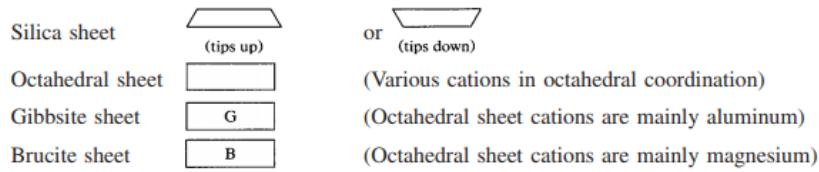


**Figure 1.3:** Schematic representation of simple mineral sheets [8].

structures. For this reasons this approach, called *building block*, is useful just to understand conceptual models. This being said, a good representation of this approach is shown in Figure 1.4: in particular in the last line different groups of clays are represented. Another advantage of this kind of grouping is that minerals that share crystal structure also have similar mechanical and engineering properties. Minerals can be divided into different categories according to their

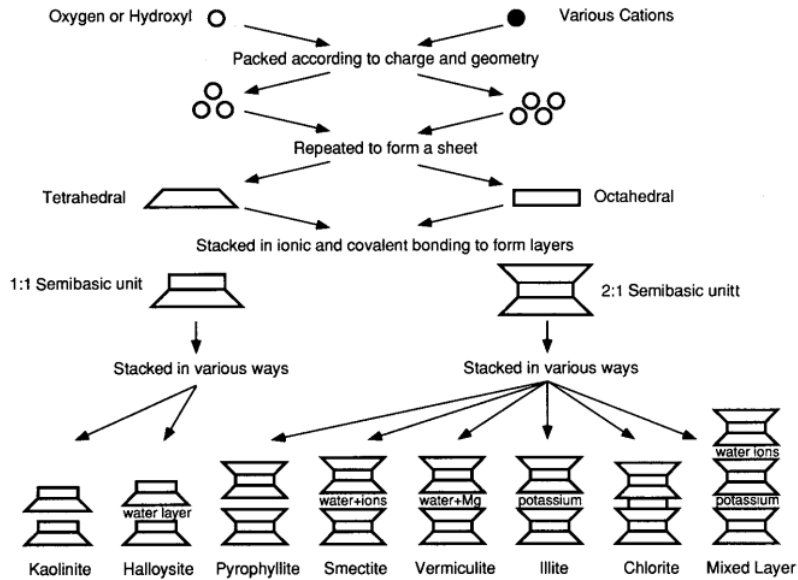


**Figure 1.4:** Synthesis pattern for the clay minerals [8].

complexity, since they can be made of multiple sheets, ranging from two to four. The two-sheet minerals, as briefly stated before, are composed by a silica sheet and an octahedral sheet. The three-sheet minerals are composed of either a dioctahedral or trioctahedral sheet between two silica sheets. Finally, the four-sheet structure is now briefly introduced: it can be found in the mineral called chlorite and it is composed by a 2:1 layer plus an interlayer hydroxide sheet. Other than these possibilities clay-like materials with no clear crystal structure could also be found; those materials are referred to as allophane or noncrystalline clay.

### 1.1.1 The 1:1 structure

Minerals whose structure is composed by one silica sheet and one octahedral sheet alternating are called 1:1 structure minerals. One main example of this particular material is *kaolinite*, as can be seen in Figure 1.5. Between different layers, sheets are connected by van der Waals forces and hydrogen bonds. It is important to notice that this kind of bonding is strong enough not to have swelling in presence of water. Characterising also the octahedral sheet there are

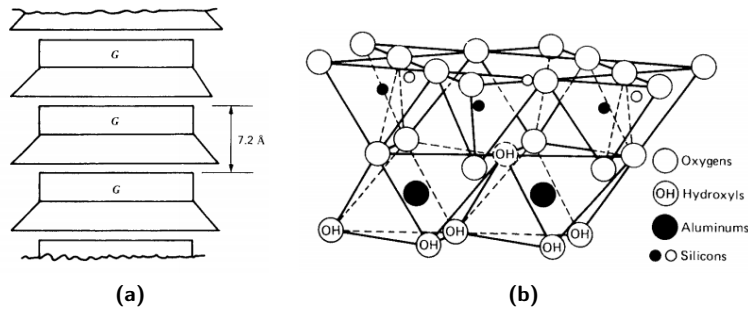


**Figure 1.5:** Scheme of kaolinite structure: (a) sheet scheme, (b) diagrammatic chemical scheme [8].

two possibilities in the resulting mineral: when it is brucite, in fact, the result is in the serpentine subgroup, otherwise if it is gibbsite the mineral is in the kaolinite subgroup. Anyway the former is quite rare and often is found mixed with other minerals like kaolinite or illite and for this reason is hard to identify. As stated before, even if they are pretty useful in order to understand the structure of these minerals, schemes like the one portrayed in Figure 1.5 are extremely simplified: in reality there are some differences in the distances among oxygens in kaolinite minerals and this results in a triclinic and not monoclinic structure. Furthermore, different members in the kaolinite groups can be obtained with changes in the stacking of layers and also with different positions of aluminium ions within the available sites in the octahedral sheet.

### 1.1.2 The 2:1 structure

Minerals whose structure is composed by two silica sheet around one octahedral sheet are called 2:1 structure minerals. One main example of this particular material is *smectite*, as can be seen in Figure 1.7. In both the silica sheets oxygens point toward the center of the cell and they are shared with the octahedral sheet. Between different cells the bonding is obtained by van der Waals forces but also by cations: in particular cations manage to balance charge deficiencies in the structure. This kind of bonding is weak and can be easily separated by the absorption of water or other polar liquids. Finally it is now important to define another property of this structure: when the solid particles composing the clay are very small in size ( $d < 2\mu\text{m}$ ) and the pore fluid is distilled water or a different polar fluid, the weak inter-layer bonds are easily separated and the clay swells; this behaviour is absent in case the polar fluid is a saline solution, as will be seen in section 1.2; clays that present this kind of behaviour are called *active clays*.

In the next pages a characterisation of some 2:1 minerals will be provided, dividing them in active minerals and inactive minerals.

### inactive minerals

A clay can be called inactive (or non-active) when its activity  $a_c$  is below 0.75, with

$$a_c = \frac{I_p}{\text{Content (\%) of clay size fraction} < 2\mu\text{m}}$$

$$I_p = w_L - w_P, w_L = \text{liquid limit}, w_P = \text{plastic limit}$$

Where the liquid limit is the percentage of water at which clay starts behaving like a liquid, while the plastic limit is the water moisture content at which a thread of soil with 3.2mm diameter begins to crumble. In this case swelling minerals are probably not present inside the clay and its swelling potential is very low. Examples of this clay mineral are illite and kaoline.

**Illite** The basic structural unit of this mineral is made by three layers, with the silica layers around a gibbsite one. All the silica tips point towards the center and are in common with the gibbsite layer. One out of four of the silica positions are instead filled by aluminium, creating a charge deficiency, which is balanced by potassium between different structural units; a scheme of this structure is shown in Figure 1.6. As stated before, this kind of scheme representation doesn't

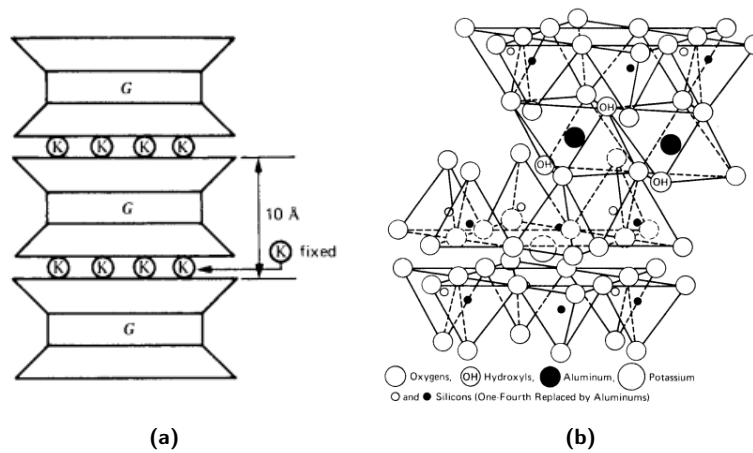


**Figure 1.6:** Scheme of illite structure: (a) sheet scheme, (b) diagrammatic chemical scheme [8].

match with reality, where imperfections are often present. In particular in illite the stacking has some randomness and some illite may contain magnesium and iron other than aluminum in the octahedral sheet. Regarding its morphology, illite is composed by very small and fragile particles mixed with other materials, both clay- and non clay-like.

## Active minerals

A clay can be called active when its activity  $a_c$  is over 1.25, with  $a_c$  defined as before. In this case there is a strong chance swelling minerals are present inside the clay and it has a high swelling potential. Examples of this kind of clays are smectite and bentonite; the latter will be the focus of this work.

**Smectite** Smectite minerals have a structure consisting in an octahedral gibbsite sheet between two silica sheets as shown in Figure 1.7 with both sheet scheme and chemical scheme. Silica sheets' tips are made by oxygens and they all point toward the center of the unit cell; furthermore these oxygens are in common with the octahedral sheets. Between different layers van der Waals forces balance the charge deficiency that are present in the structure. In case of absorption of water (or other polar liquids) this forces are easily overcome given that they are very weak. Smectite minerals are characterised by the widely

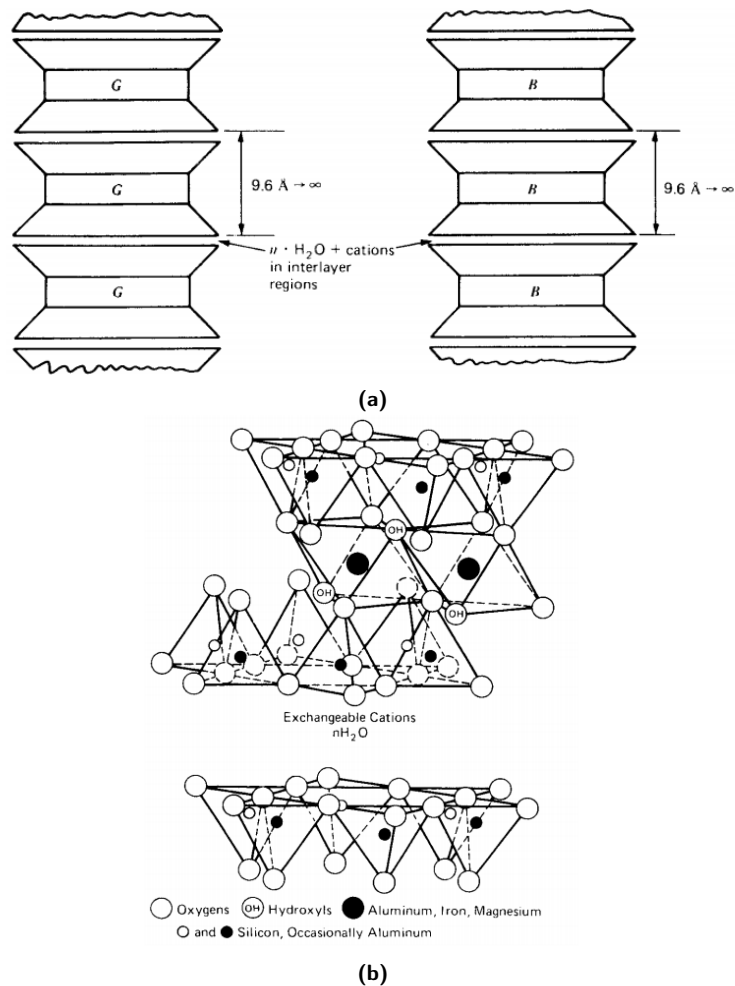


**Figure 1.7:** Scheme of smectite structure: (a) sheet scheme, (b) diagrammatic chemical scheme [8].

presence of isomorphous substitution for silicon and aluminum by other cations. In particular, aluminium may be substituted by magnesium, iron, zinc, nickel, lithium, or other cations. Regarding its morphology, smectite comes in very small and thin particles and its shape can be associated with the one of little films.

**Bentonite** Similarly to smectite, bentonite is a highly swelling clay material. It is used in many engineering processes, one example being its employ as drilling mud, but also in slurry walls in the clarification process of beer and wine. Bentonite is a very plastic, colloidal and expanding material with a liquid limit that can overcome the 500%. For these reasons, if it is present in large quantity in soft shale or as a seam in rock formations, it can be cause of continuing slope instability (one example of this phenomenon could be found in Portuguese bend, California). Moreover, high swelling capacity, low permeability and high absorption capacity make it a material suitable to be used as a barrier for the disposal of nuclear waste, as well as being normally used in landfills. In this work a great focus will be placed on this particular soil mineral and on its behaviour.

## 1.2 Ion distributions in clay-water systems: double-layer theory

On the surfaces of negatively charged clay particles adsorbed cations are tightly held; furthermore, cations in excess of those needed to neutralize the electronegativity clay particles and associated anions are present as salt precipitates. These cations try to diffuse away throughout the pore fluid because of their high concentration near the surfaces of particles. At the same time, the negative electrical field originating in the particle surfaces and ion-surface interactions oppose to this behaviour. The charged surface and the distributed charge in the adjacent phase are together termed the *diffuse double layer*. The most cited ionic distribution theory was developed by Gouy (1910) and Chapman (1913); their study was later extended by Derjaguin and Landau (1941) and Verwey and Overbeek (1948) with the description of repulsive forces among colloidal particles and stability of colloidal suspensions. Their theory is now referred to as *DVLO*.

### 1.2.1 Mathematical description

Taking into account platy clay particles the assumption of diffusive double layer on planar surfaces is reasonable: from now on the theory will be based on this assumption. Furthermore a few simplifying hypotheses are made:

- ions in the double layer are considered as point charges, and there are no interactions between them;
- charge on the particle surface is uniformly distributed;
- the particle surface is a plate that is large relative to the thickness of the double layer (one-dimensional condition);

- the permittivity of the medium adjacent to the particle surface is independent of position.

The concentration of ions (ions/ $m^3$ ) of type  $i$ , here defined as  $n_i$ , in a force field at equilibrium is given by the Boltzmann equation:

$$n_i = n_{i0} \exp\left(\frac{E_{i0} - E_i}{kT}\right) \quad (1.1)$$

The subscript 0 represents the reference state, taken to be at a large distance from the surface,  $E$  is the potential energy,  $T$  is temperature (K), and  $k$  is the Boltzmann constant (the gas constant per molecule) ( $1.38 \cdot 10^{-23} JK^{-1}$ ). The potential energy of an ion in an electric field  $E_i$  is

$$E_i = v_i e \Psi$$

where  $v_i$  is the ionic valence,  $e$  is the electronic charge ( $1.602 \cdot 10^{-19} C$ ), and  $\Psi$  is the electrical potential at the point. Potential varies with distance from a charged surface in the manner shown by Figure 1.8.

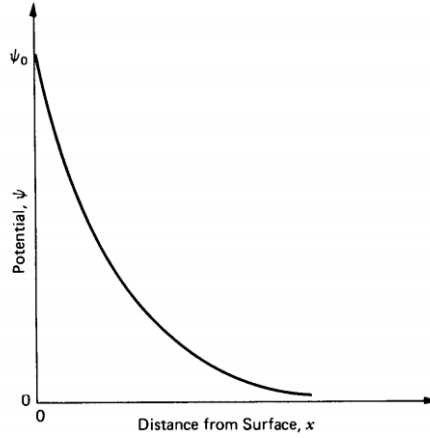


**Figure 1.8:** Variation of electrical potential with distance from a charged surface [8].

Considering then the one-dimensional Poisson equation, which relates potential, charge, and distance

$$\frac{d^2 \Psi}{dx^2} = -\frac{\rho}{\epsilon} \quad (1.2)$$

where  $\epsilon$  is the static permittivity of the medium ( $C^2 J^{-1} m^{-1}$  or  $Fm^{-1}$ ) and  $\rho$  is the charge density, defined as:

$$\rho = e \sum_i v_i n_i \quad (1.3)$$

Substituting Eq. 1.1 in Eq. 1.3 it is possible to obtain a relation between density  $\rho$  and ions concentration  $n_i$ :

$$\rho = e \sum_i v_i n_{i0} \exp\left(\frac{E_{i0} - E_i}{kT}\right) \quad (1.4)$$

Finally, substituting Eq. 1.4 in Eq. 1.2 it is possible to obtain:

$$\frac{d^2\Psi}{dx^2} = -\frac{e}{\epsilon} \sum v_i n_{i0} \exp\left(\frac{-v_i e \Psi}{kT}\right) \quad (1.5)$$

which is the differential equation for the electric double layer adjacent to a planar surface. This equation describes a roughly exponential decay of potential with distance from the surface. The center of gravity of the diffuse charge is at a distance  $x = 1/K$  from the surface, where  $K$  is defined as

$$K^2 = \frac{2n_0 e^2 v^2}{\epsilon kT}$$

and so:

$$\frac{1}{K} = \left( \frac{\epsilon kT}{2n_0 e^2 v^2} \right)^{\frac{1}{2}} \quad (1.6)$$

This distance is a measure of the *thickness* of the double layer. According to Equation 1.6, the value of  $1/K$  depends on the characteristics of the dissolved salts and the fluid phase which are influenced, obviously, by the type of clay and the conditions in pore solution. Breaking down each factor controlling  $1/K$ , we have:

- particle surface charge;
- surface potential;
- specific surface;
- dissolved ion interactions and concentration.

Regarding ion concentration, it is possible to say, according to Equation 1.6, that  $1/K$  varies inversely with the square root of  $n_0$ . Moreover, in the hypothesis of constant surface charge, an increase in electrolyte concentration reduces surface potential and the decrease of potential is faster, resulting in a thinner diffusive layer. Applying these considerations to clay behaviour it is possible to say that an increase in concentration, and so in electrical potential, between different clay particles (here considered as flat plates) leads to a decrease in repulsive forces and to an increase of the flocculation phenomenon. This kind of behaviour has large influence on clay swelling: it in fact depends, at least in part, on electrolyte concentration in the water. This topic has great importance for the present work and will be dealt with in depth in the next section.

### 1.3 Evidences of the influence of the pore fluid chemistry on the mechanical behaviour of active clays

As anticipated in the previous section, there is a strong causality effect between the pore fluid composition and the changes in the behaviour of clays. In particular it is possible to modify the mechanical behaviour of active clays changing the chemical composition of the pore fluid. In this section this phenomenon will be characterised considering a volume element of bentonite, prepared in two different ways:

- *remoduled bentonite*: the sample is prepared mixing it with distilled water, obtaining a clay with an high water content (ratio of water mass to solid mass).
- *compacted bentonite*: the sample is compacted at a low water content by applying a mechanical load; it is afterwards saturated with some solution (distilled water or saline solution).

Particular stress during this characterisation will be put on the effects that chemical changes in the interstitial fluid have on the volume of clay samples macroscopically and on whether or not these effects are reversible; moreover, also of great importance it will be the analysis of the role played by the structure (compacted or remoduled) and by the previous mechanical loading history on the chemical and mechanical behaviour. After this short dissertation it will be possible to acknowledge that the type of response is analogous when considering compacted clay or remoduled clay but results are strongly influenced by the micro-structure.

### 1.3.1 Remoduled bentonite

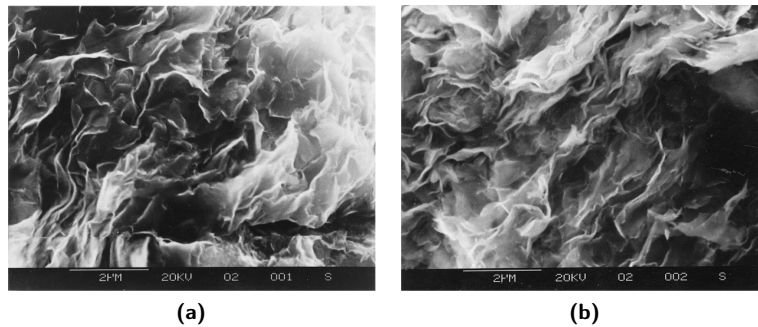


**Figure 1.9:** SEM images of Ponza bentonite: (a) sample saturated with a  $NaCl$  solution and then exposed to distilled water, (b) sample saturated with distilled water [3].

The remoduled bentonite whose behaviour will be discussed in this paragraph is the Ponza bentonite characterised by Di Maio in [3]. It is a material with 80% of clay fraction and a plasticity index of 320%. Two SEM (*Scanning Electron Microscope*) images of this particular material are shown in Figure 1.9: on the left it is possible to see a sample firstly exposed to a saturated solution of  $NaCl$  and subsequently to distilled water, while on the right a sample exposed on distilled water; it is interesting to notice that it is not possible to recognize aggregates and the structure of the sample is uniform in both cases, unlike what, as will be shown in the next section, it is possible to observe in a compacted material (Fig. 1.13). Taking into account its mechanical behaviour, in Figure 1.10 it is shown the process of repeated cell fluid changes on this particular bentonite: keeping the stress constant at 40  $KPa$  and changing from distilled water to  $NaCl$  causes a major change in strain percentage which implies a change in void ratio. These macroscopic changes are directly influenced by the microscopic behaviour: adding a  $NaCl$  saline solution to the sample causes an increase in ion concentration

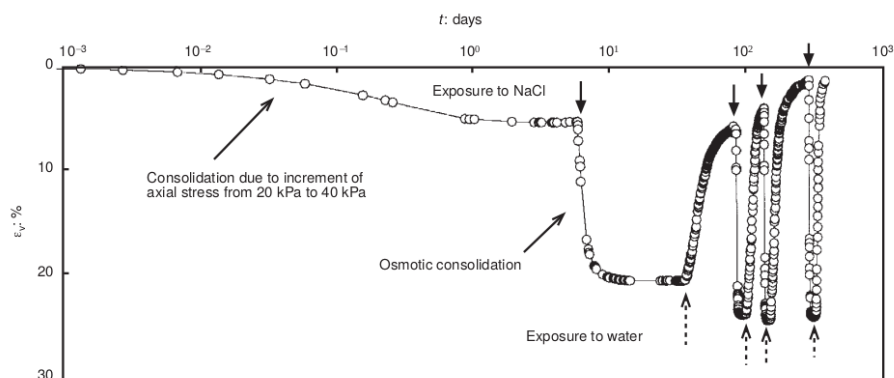


**Figure 1.10:** Osmotic volumetric strain produced by repeated cell fluid replacements. After an initial mechanical load, stress is kept constant at 40 *KPa* [3].

of the interstitial fluid and so, as seen in the previous section, a decrease of the double layer thickness and of the repulsive forces among particles. These microscopical behaviour is responsible for the macroscopic volume decrease. On the contrary, changing interstitial fluid from saline solution to distilled water causes a decrease in ions concentration and consequently an increase in the repulsive forces, leading to a macroscopic increase of volume. These changes are obviously not immediate and indeed are characterized by a long transition phase in which the void ratio increases or decreases. It is also important to remark that multiple cycles of substitutions in pore fluid lead to an amplification of strain ranges and consequently volume changes; this effect expresses that changes in void ratio don't depend only on the chemical composition of the pore fluid but also on the previous chemical loading history of the clay: even if this phenomenon is currently under study, it is due to progressive substitution of heterocations initially present in the natural bentonite by  $Na^+$ , increasing the double layer thickness and so repulsive forces among particles. One more factor influencing the phenomenon of swelling in clays is the level of stress applied on the sample. In Figure 1.11 it is possible to observe how different mechanical loads affect the process: each one of the five plots shows the process of exposing bentonite to *NaCl* and re-exposing it to distilled water for different values of stress. For relatively small values of stress, like in Figure 1.11 (a) and (b), respectively 40 *KPa* and 160 *KPa*, it is possible to observe an almost complete recovery in strain percentage, with the latter reaching a plateau before the former. With a significant value of stress, like in Figure 1.11 (c), where it is equal to 320 *KPa*, results are different: after 30 days the process can be considered completed but there hasn't been a complete recovery in volume, with a residual strain of about 7% from a maximum being around 13%. Finally, Figure 1.11 (d) and (e) show a situation where recovery is almost absent, with values of stress of 640 *KPa* and 960 *KPa*. It is interesting to remark, moreover, that each one of the five plots of Figure 1.11 have something in common: while the gain in strain after changing pore fluid to *NaCl* is quite fast, the same cannot be said when the bentonite is re-exposed to distilled water; the reason behind this is that, because of repulsive forces in the micro structure, the average pore size is bigger when pore fluid is distilled water and this facilitates the motion of fluids.

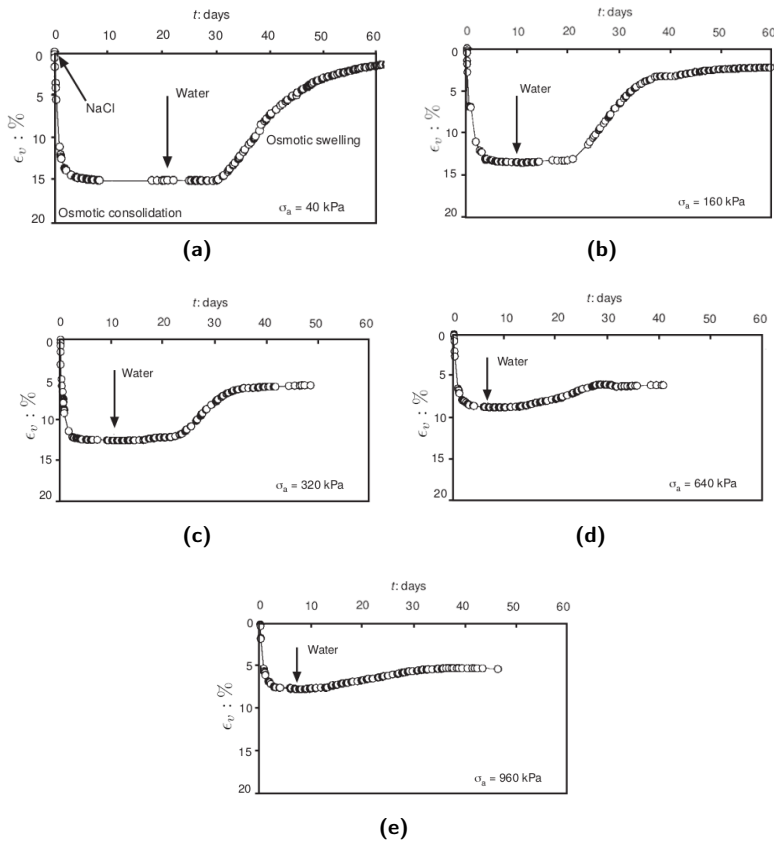


**Figure 1.11:** Strain percentage results obtained with chemical load for different values of uniaxial stress [3].

Contrarily, when distilled water is added, bentonite micro-structure is tighter, with smaller pores, which are not easily reached by the "new" fluid (i.e. distilled water). Concluding this paragraph, figure 1.12 shows a comparison between mechanical loadings for both distilled water and *NaCl* saturated samples and a combination of mechanical and chemical loading. In particular, in the top plot, after a mechanical compression reaching  $1200\text{ KPa}$  the sample was exposed to *NaCl* and, once at equilibrium, loaded up to  $2500\text{ KPa}$ . Subsequently, it was unloaded to  $40\text{ KPa}$  and re-exposed to water. The comparison shows that, while the unloading curve is parallel to the *NaCl* mechanical loading, after re-exposing to distilled water the sample was able to reach the unloading curve of distilled water mechanical load. The bottom plot of Figure 1.12 shows the same process but exposing the sample to *NaCl* at a lower stress: results are similar to the ones obtained in the top plot. Furthermore, Figure ref fig1: 12 shows some interesting properties related to the behavior of the clay when the interstitial fluid changes: first of all, it is evident that the interstitial fluid influences the compressibility of the material, the latter being bigger in the case of distilled water; secondly, the saline solution introduced in a structure prepared with distilled water does not allow to obtain the same compressibility as the one of the material prepared with saline solution from the beginning.

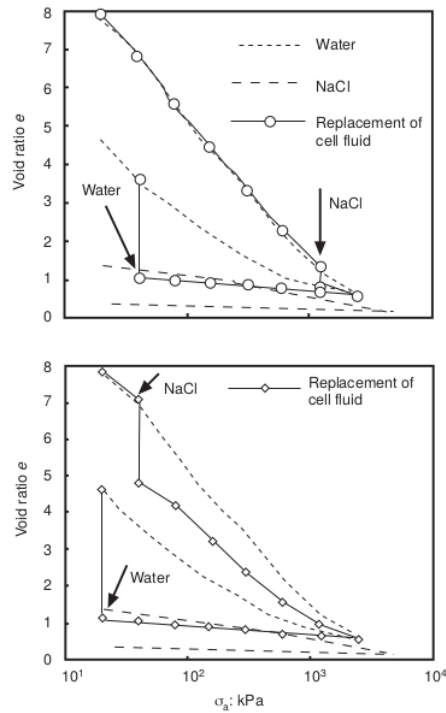


**Figure 1.12:** Comparisons of consolidation and swelling for four samples: one in distilled water, one saturated with *NaCl* and two with replacement of cell fluid [3].

### 1.3.2 Compacted bentonite

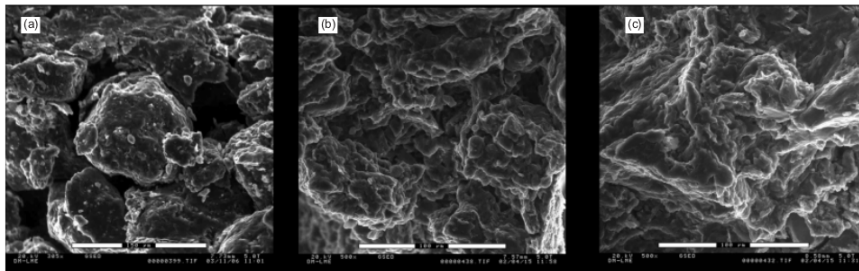


**Figure 1.13:** ESEM pictures of statically compacted FEBEX samples: (a) as-compacted at hygroscopic water content, (b) after saturation with 0.5 mol/l *NaCl* solution; (c) after saturation with distilled water. Black bar is  $150\mu\text{m}$  in (a) and  $100\mu\text{m}$  in (b) and (c) [5].

The compacted bentonite whose behaviour is discussed in this paragraph is the FEBEX bentonite, which is studied in the context of radioactive waste disposed by the Spanish Nuclear Agency: this material has a content of montmorillonite higher than 90%, a liquid limit of  $102 \pm 4\%$  and a plastic limit of  $53 \pm 3\%$ . Analysing the three ESEM (*Environmental Scanning Electron Microscope*) images in Figure 1.13 it is easy to understand the changes in micro-structure caused

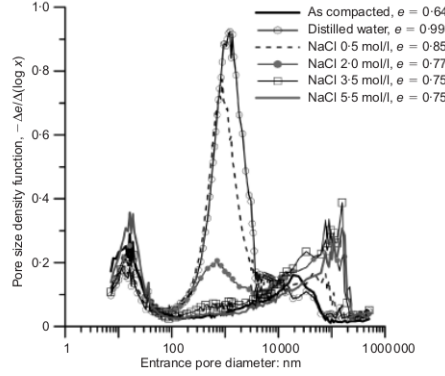


**Figure 1.14:** MIP pore size distributions of bentonite saturated with *NaCl* solutions having different concentrations [5].

by different preparations of samples and different pore fluids: in image (a) it is possible to distinguish different aggregates of clay particles, while in image (c) it is not. This effect is mainly due to pore fluid: the presence of a saline solution as interstitial fluid causes a shortening in the double layer and so a drop down of repulsive forces, making it possible for clay micro-particles to flocculate. Figure 1.14 shows the differences in pore size caused by different interstitial fluids measured by MIP (*Mercury Intrusion Porosimetry*) test. Switching from distilled water to an *NaCl* saline solution makes the distribution change largely: if indeed the distilled water distribution has only one mode, the saline solution one is bimodal. Starting from these observations, micro- and macro-pores will hereby defined, and consequently micro and macro porosity or void ratio. Pores inside a single clay aggregate will be denoted with the word micro-pore, while macro-pore will refer to all voids among different clay aggregates. Given the difficulty of dividing the two categories, a few assumptions will be made:

- it is supposed the existence of a single size threshold between the two categories, without taking into account pore shape;
- The mode of the distilled water distribution will be used as a deciding criterion;

This way, from now on every pore that is on the left side of the distilled water distribution mode will be considered a micro-pore, while each one on the right will be considered a macro-pore. Consequently it is important to define micro and macro void ratio,  $e^m$  and  $e^M$  respectively. For  $e$ ,  $e^m$  and  $e^M$  holds:

$$e = \frac{V_V}{V_S}, \quad e^m = \frac{V_{V^m}}{V_S}, \quad e^M = \frac{V_{V^M}}{V_S(1 + e^m)},$$

where  $V^m$  is the volume of micro-pores,  $V^M$  is the volume of macro-pores,  $V_V$  is the total volume of pores,  $V_V = V_{V^m} + V_{V^M}$  and  $V_S$  is the total volume of solids. The term  $1 + e^m$  in the last equation is needed because macro void ratio is defined as the volume of macro-pores over the total volume of aggregates, which is the volume of solids plus the volume of micro-pores [2]. It is now possible to

define  $e$  starting from  $e^m$  and  $e^M$ :

$$e = \frac{V_V}{V_S} = \frac{V_{V^m} + V_{V^M}}{V_S} = e^m + e^M (1 + e^m) = e^m + e^M + e^m e^M$$

Taking into account the mechanical behaviour of FEBEX bentonite, Figure 1.15 shows the process of swelling for different pore fluids, measuring different stress responses. As it is possible to see, when the swelling process is concluded, higher

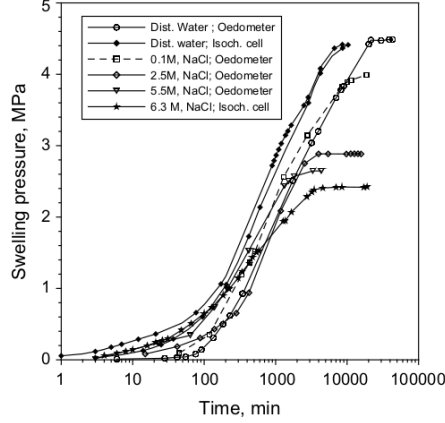


**Figure 1.15:** Evolution of swelling pressures measured for different  $NaCl$  concentration in the pore fluid [4].

$NaCl$  concentrations are associated with lower values of swelling pressure: the suppression of the thickness of the double layer corresponds to a smaller swelling potential. Vice versa, distilled water saturated clay shows a greater swelling potential and a great residual swelling pressure. Furthermore, four different types of FEBEX bentonite samples were exposed to salinisation-desalinisation cycles in [6], in an attempt of investigate the role of the type of structure (matrix as due to remoduled conditions or aggregated as due to compaction). Two different loading histories were applied to the remoduled samples ( $MC$  samples in Table 1.1) and two different initial densities were imposed on compacted samples ( $C$  samples in Table 1.1). Mechanically consolidated samples  $MC1$  and  $MC2$  are

Sample	Initial void ratio	Void ratio at saturation	Applied vertical net stress (KPa)
C1	0.87	1.23	200
C2	0.60	0.84	200
MC1	1.35	1.35	200
MC2	1.25	1.25	500

**Table 1.1:** Testing conditions of FEBEX samples. [6]

obtained loading slurries of FEBEX powder and distilled water with a vertical net stress of  $1500KPa$ . The stress was then reduced to  $200KPa$  for  $MC1$  and  $500KPa$  for  $MC2$  in order to obtain the desired void ratio and the mechanical

conditions imposed during the chemical cycling. Figure 1.16 shows a chemical

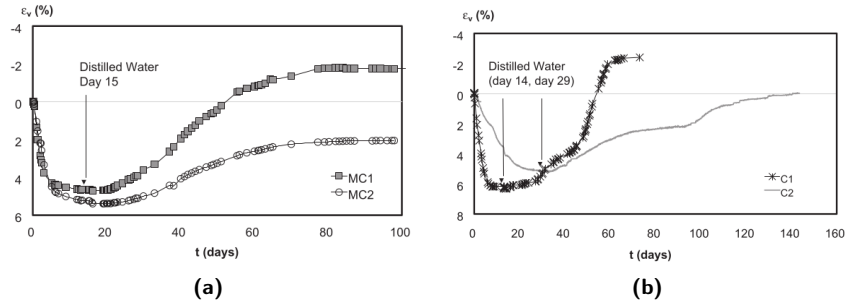


**Figure 1.16:** Deformations imposed by the chemical cycle on FEBEX bentonite samples [6].

cycle made with a constant mechanical load for each one of the for bentonite samples described in Tabular 1.1. In Figure 1.16 (a) the two MC samples are compared: for MC1, after it is re-exposed to distilled water, there is a complete volume recovery and moreover it swells more than what previously consolidated, while the opposite holds for MC2. In both cases irreversible strains are present. In Figure 1.16 (b) the two C samples are compared: the curve representing the process of C1 is completely analogous to the one representing MC1 while C2 shows an almost reversible behaviour.

## Chapter 2

# Discrete Element Method DEM

In this chapter an overview of the Discrete Element Method will be given. In particular, after a section in which granular materials properties will be discussed along with the reasons why it is convenient to simulate those kind of materials with DEM, the basis of the method will be provided, taking into account its mathematical formulation and its possibilities. A particular stress will be put in the contact model that has been used in numerical simulations exposed in next chapters. Finally, a brief introduction to the code used for the implementation will also be provided.

### 2.1 Granular materials and DEM

Granular materials, i.e. agglomerations of discrete, macroscopic particles, are omnipresent in both industry and nature. They range from natural materials like snow, sand, soil, coffee, rice and coal to artificial materials such as medicinal tablets, catalysts or animal feed: they are, indeed, the second most most manipulated raw materials after water. Furthermore, they are involved in physical phenomena like sandstorms, avalanches and earthquakes, concerning respectively sand, snow and soil. The distinction between granular materials and fine particulates (or molecules) is obviously made taking into account the size of their constituent particles: the constituents that compose granular material must be large enough such that their movement is not subject to thermal fluctuations. Thus, the lower size limit for granular materials can be defined as  $1\mu m$ . On the other hand, there is no upper size limit, considering that the physics of granular materials have been applied to the formation of solar systems, galaxies and the universe. When studying this kind of matter, the massively high number of degrees of freedom takes to wildly non-linear behaviour. For this reason, it is quite challenging to characterize such materials with a continuum mechanics approach (for example FEM): considering a continuum model, indeed, movements and rotations of particles inside the material are not considered; thus, in order to capture its micro-mechanical behaviour, it is needed to couple the model with complex contact laws. Differently, when using DEM this is not needed and capturing the micro-mechanical behaviour of those materials is quite easy.

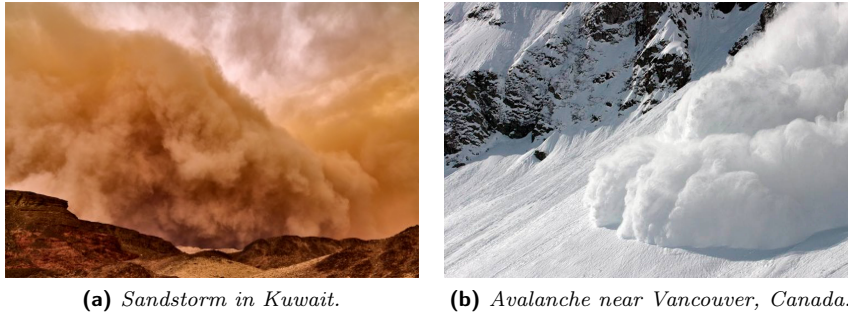


**Figure 2.1:** Sandstorms and Avalanches are both characterised by the convection of granular materials (sand and snow).

The DEM (Discrete Element Method) consists in simulating the interactions among a large number of discrete particles or bodies. During numerical simulations particles are free to move, rotate, get and loose contact with each other. In DEM, even if simple contact laws and simple particle shapes (e.g. spheres) are adopted, it is still possible to capture salient response characteristics of granular material behaviour. Moreover, given the simplicity of the model, it is possible to involve in the simulation a relatively large number of particles without heavily increasing the computational cost of the simulation. The usage of this method has been exponentially increasing during the last decade, as can be seen in Figure 2.2a. The main reason behind this is the increasing in computational power: when it was firstly formulated and published by Cundall and Strack (1979) it was very difficult to simulate large number of particles because of the lack in computational power, but today it is possible to easily simulate systems with up to  $10^5$  particles. In Figure 2.2b it is possible to notice that the increase in usage of DEM has been particularly relevant in the soil mechanics framework.

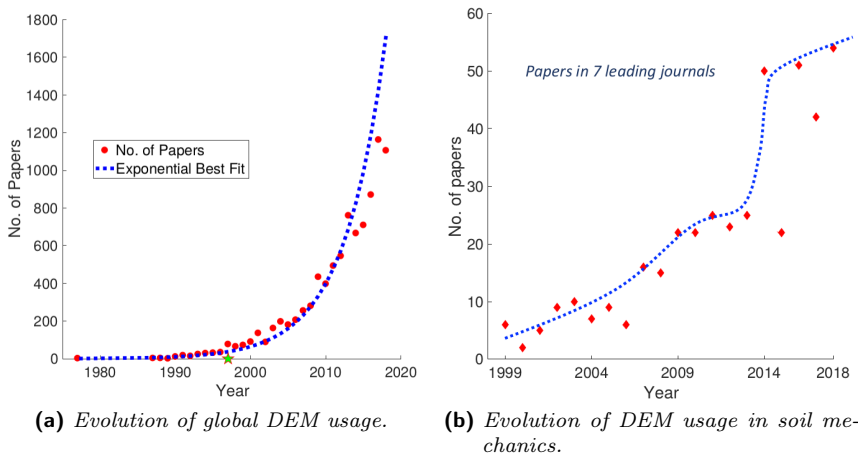


**Figure 2.2:** Evolution over time of DEM method: the increasing over the last 20 years is exponential.

Two main reasons can be considered when taking into account the usage of DEM in soil mechanics (or more in general in geotechnical fields): the first

one is the possibility to simulate physical laboratory tests, for example applying loads and deformations to virtual samples, monitoring and analysing particle scale mechanism. It is indeed very difficult (and in some cases impossible) to access information like particle positions and orientation, micro void ratio, the evolution of contact forces, etc., during a physical laboratory test. The second motivation for the usage of DEM in soil mechanics is that it allows the analysis of the mechanism involved in large-displacement problems in geomechanics, which cannot be easily modelled using a continuum approach model, such as FEM.

## 2.2 Soft-Particle Discrete Element Method

When taking into account the mesostructure of granular material it can be defined as grains that deform under stress. Given the extreme difficulty of realistically modelling shapes and their deformation, a few simplifying assumptions are made: firstly particles are all convex and in particular they will be spheres and secondly the interaction force will be related to the overlap  $\delta$  of two particles as a first order approximation, as can be seen in figure 2.3.

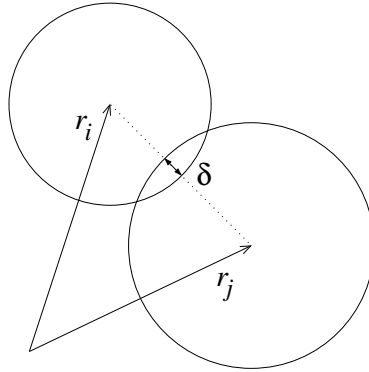


**Figure 2.3:** Two particle contact with overlap  $\delta$ .

Knowing the total force  $\vec{f}_i$  acting on particle  $i$ , either due to the contact with other particles and boundaries or from external forces (e.g. gravity), the problem is reduced to the integration of Newton's equations of motion, for the translational and rotational degrees of freedom,

$$m_i \frac{d^2}{dt^2} \vec{r}_i = \vec{f}_i + m_i \vec{g}, \quad \text{and} \quad I_i \frac{d}{dt} \vec{\omega}_i = \vec{t}_i, \quad (2.1)$$

with  $m_i$  the mass of particle  $i$ ,  $\vec{r}_i$  its position,  $\vec{f}_i = \sum_c \vec{f}_i^c$  the total force acting on it due to contacts with other particles or with the walls,  $\vec{g}$  the acceleration due to volume forces like gravity,  $I_i$  the spherical particle's moment of inertia,  $\vec{\omega}_i$  its angular velocity and  $\vec{t}_i = \sum_c \left( \vec{l}_i^c \times \vec{f}_i^c + \vec{q}_i^c \right)$  the total torque, where  $\vec{q}_i^c$  are torques/couples at contacts other than the torques due to the tangential force, e.g., due to rolling and torsion, and  $\vec{l}_i^c$  the vector from the particle's centre of mass to the contact point. After computing all forces, accelerations and velocities of each particle are computed and their velocities and positions are updated, then

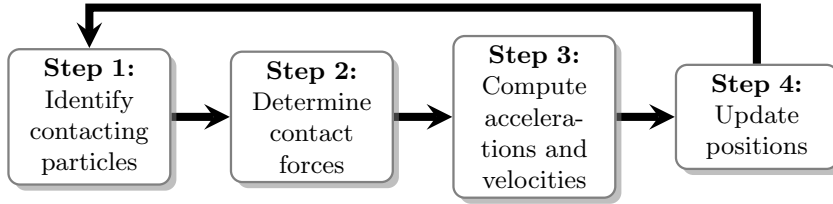


**Figure 2.4:** Flow chart of the DEM algorithm.

the algorithm starts back with a new time step identifying contacting particles (a scheme of the algorithm is shown in Figure 2.4).

If the simplifying hypothesis of no long-range interactions is adopted, two spherical particles  $i$  and  $j$ , with radii  $a_i$  and  $a_j$ , respectively, interact only if they are in contact, that is, their overlap

$$\delta = (a_i + a_j) - (\vec{r}_i - \vec{r}_j) \cdot \vec{n} \quad (2.2)$$

is positive,  $\delta > 0$ , with the unit vector  $\vec{n} = \vec{n}_{ij} = (\vec{r}_i - \vec{r}_j)/|\vec{r}_i - \vec{r}_j|$  pointing from  $j$  to  $i$ . Note that the force on particle  $i$ , from particle  $j$ , at contact  $c$ , can be decomposed into a normal and a tangential part as  $\vec{f}^c := \vec{f}_{ij}^c = f^n \vec{n} + f^t \vec{t}$ : in the following section  $f^n$  and  $f^t$  will be characterised.

### 2.2.1 Linear Normal Contact Model

The contact model used to define  $f^n$  takes into account excluded volume and dissipation, yet it is quite simple. The normal force is indeed defined based on the spring dashpot model [12]:

$$f^n = k\delta + \gamma_0 v_n, \quad (2.3)$$

with a spring stiffness  $k$ , a viscous damping  $\gamma_0$ , and the relative velocity in normal direction  $v_n = -\vec{v}_{ij} \cdot \vec{n} = -(\vec{v}_i - \vec{v}_j) \cdot \vec{n} = \dot{\delta}$ . With this model particle interactions are considered as a damped harmonic oscillator. As such, the half-period of a vibration around an equilibrium position can be computed, obtaining a typical response time on the contact level,

$$t_c = \frac{\pi}{\omega}, \quad \text{with } \omega = \sqrt{(k/m_{ij}) - \eta_0^2}, \quad (2.4)$$

with the eigenfrequency of the contact  $\omega$ , the rescaled damping coefficient  $\eta_0 = \gamma_0/(2m_{ij})$ , and the reduced mass  $m_{ij} = m_i m_j / (m_i + m_j)$ . Computing the velocity at the half period of the oscillation, it is also possible to obtain the coefficient of restitution,

$$r = -v'_n / v_n = \exp(-\pi \eta_0 / \omega) = \exp(-\eta_0 t_c), \quad (2.5)$$

which quantifies the ratio of relative velocities after and before the collision. The contact duration in Eq. (2.4) is also of practical technical importance, since the integration of the equations of motion is stable only if the integration time-step

$\Delta t_{\text{DEM}}$  is much smaller than  $t_c$ . Taking into account the tangential force  $f^t$ , it is defined based on  $f^n$ , coupling the two via Coulomb's law:

$$f^t \leq f_C = \mu f^n$$

where  $\mu$  is the sliding friction coefficient. Defining the tangential displacement here, anyway, it is not easy: it is indeed necessary to *rotate* the spring obtained above projecting it on the tangential plane. This way it is possible to define a tangential spring  $\vec{\zeta}$  starting from the one defined in the previous iteration  $\vec{\zeta}'$  of the method:

$$\vec{\zeta} = \vec{\zeta}' - \vec{n} (\vec{n} \cdot \vec{\zeta}')$$

where  $|\vec{\zeta}| = |\vec{\zeta}'|$  thanks to rotation. It is now possible to state the tangential the tangential contact law as:

$$\vec{f}^t = -k_t \vec{\zeta} - \gamma_t \vec{v}_t, \quad (2.6)$$

where  $k_t$  is the tangential stiffness,  $\gamma_t$  is tangential dissipation, and  $\vec{v}_t = \vec{v}_{ij} - \vec{n} (\vec{n} \cdot \vec{v}_{ij})$ .

### 2.2.2 Adhesive, Elasto-Plastic Normal Contact Model

In this section a different contact model will be defined: the adhesive, elasto-plastic normal contact model. It is a simplified version of more complicated nonlinear-hysteretic models which take into account plasticity; in particular this contact model is able to describe plastic deformations that take place at the contact point defining two different forces in loading and unloading. Figure 2.5 shows a scheme of the loading and unloading process.

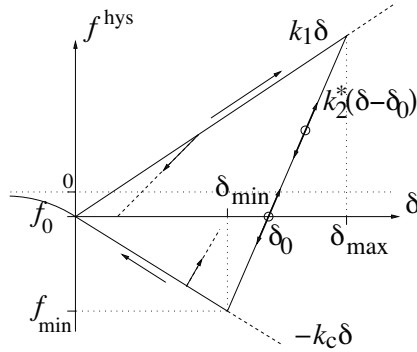


**Figure 2.5:** Scheme of the adhesive, elasto-plastic normal contact model.

When two particles get in contact, force increases linearly with overlap, having a slope  $K_1$ , until the overlap  $\delta_{max}$  is reached. When unloading yet the slope is different, being equal to  $K_2^*$ , resulting in a situation of overlap  $\delta = \delta_0 > 0$  when  $F = 0$ ;  $\delta_0$  will be a parameter of fundamental importance in this work, as will be seen in the next chapter, and from now on it will be referred to as *penetration depth max*. In addition to that, the model hides a nonlinear feature: when unloading from a generic  $\delta < \delta_{max}$  the slope  $K$  will be  $K_2^* \geq K \geq K_1$

proportionally with  $\delta$ . The repulsive (hysteretic) force can thus be defined as

$$f^{\text{hys}} = \begin{cases} k_1\delta & \text{for loading,} & \text{if } k_2^*(\delta - \delta_0) \geq k_1\delta \\ k_2^*(\delta - \delta_0) & \text{for un/reloading,} & \text{if } k_1\delta > k_2^*(\delta - \delta_0) > -k_c\delta \\ -k_c\delta & \text{for unloading,} & \text{if } -k_c\delta \geq k_2^*(\delta - \delta_0) \end{cases}, \quad (2.7)$$

with  $k_2^* \geq k_1 > 0$ . If after the unloading phase (and so after reaching an equilibrium overlap  $\delta_{eq}$ ) the overlap is decreased ( $\delta < \delta_{eq}$ ) the force will become negative, and so attractive until the minimum force  $-k_c\delta_{\min}$  is reached at the overlap  $\delta_{\min} = (k_2^* - k_1)\delta_{\max}/(k_2^* + k_c)$ . From this point on, if the process of unloading continues, the attractive force will become  $f^{\text{hys}} = -k_c\delta$ , because of the switch on the adhesive branch with slope  $-k_c$ .

## Chapter 3

# Clusters

In order to get a good characterization of dual porosity problems simple spherical particles are not enough representative: even if it is very simple to use them in a simulation, changes in micro- and macro-structure can't be simulated. In this study usual spherical elementary particles will be substituted by clusters [9]. The term cluster in this context is used to define a collection of particles "glued" together forming a single unit: particles indeed are pulled together thanks to the cohesive force of the elasto-plastic normal contact model discussed above.

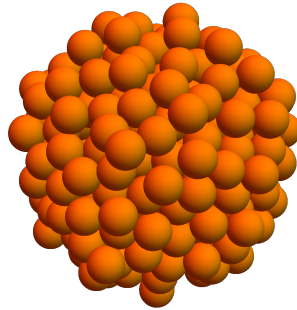


**Figure 3.1:** Example of a cluster composed by 300 particles.

When modelling soil (but also particles of pharmaceutical interest or catalysts for example) this particular entity has a series of characteristic that makes it quite appealing:

- relative positions among particles are not fixed: the complex internal structure inside the cluster can, for this reason, change during the simulation, modelling variation of the micro structure;
- changes in the shape of the cluster can be useful to characterize changes in the meso-structure of the material;

- even if the complex internal structure can't be known *a priori*, it is possible to analytically determine the void fraction of the cluster, influencing not only dimensions but also the stiffness of the cluster;
- differently from multi-spheres and super-quadrics, which are different possible approaches both able to define complex structures, clusters are breakable, deformable and there is no need to compute their rigid body dynamics.

These are the reasons why the study proposed in this work is carried on with the usage of clusters and in this chapter their properties will be explained.

### 3.1 Creation of a single cluster

As explained in Chapter 2, thanks to the adhesive elasto-plastic normal contact model, if two particles collide, after the collision their overlap is greater than zero (given that no external forces are applied). Moreover, its value can be known *a priori*: if indeed during the process the overlap gets bigger than  $\delta_{max}$ , at the end it will be equal to  $\delta_0$ . This is the central idea behind the creation of a single cluster. In order to create a single cluster, a separate DEM simulation is needed and this are the principal steps required:

- firstly, particles are placed into an empty domain with random spherical coordinates

$$\begin{aligned}
 R &= \sqrt[3]{rand(0,1)} \cdot \frac{L}{2} \\
 \theta &= \pi \cdot rand(0,2) \\
 \phi &= arccos rand(0,1)
 \end{aligned}$$

where:  $R$ ,  $\theta$  and  $\phi$  are the spherical coordinates,  $rand(a,b)$  is a uniform distributed random number in the interval  $(a,b)$  and  $L$  is the dimension of the cubic domain. As can be seen  $R$  and  $\phi$  are rescaled with the cubic root and the arc cosine respectively: this has been done in order to get a particle distribution as uniform as possible inside the domain.

- a force pointing towards the center of the domain is then applied to each particle: the magnitude of the force and the duration of this process are computed so that each interaction will have a final overlap  $\delta : \delta > \delta_{max}$ : firstly a maximum value for the force  $F_{max}$  and the total time  $T$  are calculated

$$\begin{aligned}
 F_{max} &= \delta_{max} k_2^* \\
 T &= \bar{k}_1^{-1} \sqrt[2]{\frac{\bar{k}_2 m L}{F_{max}}}
 \end{aligned}$$

where  $\bar{k}_1 = 5$  and  $\bar{k}_2 = 100$  are two safety factors and  $m$  is the mass of a single particle. After that, the force applied to the particles  $f$  depends on time  $t$  and on their distance from the center of the domain  $d$ , such as:

$$f(d,t) = F_{max} \frac{d}{r} \frac{t}{T}$$

where  $r$  is the radius of the micro-particle composing the cluster;

- after compressing, force is slowly removed; in this process, which takes a total time  $T$ , the value of the force applied to a single particle is also depending on time  $t$  and distance from the center of the domain  $d$ :

$$f(d, t) = F_{max} \frac{dT - t}{T}$$

- finally, for a few time steps velocities are damped until the value of the ratio between kinetic energy and potential energy is smaller than  $10^{-8}$ : this is done in order to be sure of the stability of the cluster after its creation.

At the end of this process, the average overlap among the particles of the cluster  $\bar{\delta}$  will be:

$$\bar{\delta} = \frac{1}{M} \sum_{j=0}^M \delta_j \simeq \delta_0$$

with  $\delta_j$  being the overlap in the  $j$ -th interaction and  $M$  being the total number of interactions. Before proceeding with the presentation of clusters' properties it is necessary, given their discrete nature, to state a proper way to define clusters dimensions, and in particular their radius  $R$ . Taking into account a cluster composed by  $N$  particles  $P_i$ , with position  $\mathbf{p}_i$ ,  $i = 1, \dots, N$ , all having radius  $r$  (i.e. with no size dispersity) and all with the same density, it is possible to define its center of mass  $\mathbf{C}$  as

$$\vec{C} = \frac{1}{N} \sum_1^N \vec{p}_i,$$

where  $\mathbf{p}_i$  is the position of the  $i$ -th particle's center. Similarly, it is possible to define the distance from the center of mass of the farthest particle  $\bar{d}$  as

$$\bar{d} = \max_i \left\| \vec{p}_i - \vec{C} \right\|.$$

After this definitions, it is now possible to state the measure for the cluster radius used in this work: considering the particles  $P_j$ , with  $j = 1, \dots, n$ ,  $n \leq N$  whose distance  $d_j$  from the center of mass  $\mathbf{C}$  is  $d_j = \|\mathbf{p}_j - \mathbf{C}\| > \bar{d} - r$ , cluster radius  $R$  can be defined as:

$$R = \frac{1}{n} \sum_{j=1}^n d_j \quad (3.1)$$

Clusters can be created taking into account many different properties, such as particles dispersity, sliding friction, normal and tangential stiffness, etc., but when considering its dimension  $R$  and volume ratio  $\zeta$  two properties are the most important:  $\delta_0$ , which is the penetration depth max, and obviously the number of particles  $N$ . Considering this two properties it is indeed possible to analytically determine the relative cluster radius  $\hat{R} = R/r$  and also its volume ratio  $\zeta$ . In order to do so, a few geometrical considerations are required. Before proceeding it is necessary to specify that throughout this discussion no size dispersity among the elementary particles will be considered and every radius is set to be unitary

( $r = 1$ ). In this way the radius of the cluster will be equal to its relative radius and the same can be stated for the penetration depth max:

$$R = \hat{R} = \frac{R}{r}, \quad \text{with } r = 1$$

$$\delta_0 = \hat{\delta}_0 = \frac{\delta_0}{r}, \quad \text{with } r = 1$$

If a particular value for the cluster radius will be needed it can be simply computed according to the radius of the elementary particle, as  $R = r\hat{R}$ . It is also important to point out that in the pair  $(N, \delta_0)$  only the first one is an extensive quantity, while the second is intensive and the same can be said about  $(R, \zeta)$ . For this reason, the relation between  $\zeta$  and  $\delta_0$  will be independent from  $R$  and  $N$  and they will be linked from their spacial arrangement. Finally, entering into details, for a homogeneous and isotropic bulk,  $\zeta$  can be calculated in the limit of  $\delta_0 \rightarrow 0$  as the ratio between the total volume of single elementary particles and the total volume of the cluster [9]

$$\zeta \xrightarrow{\delta_0 \rightarrow 0} \zeta_0 = \frac{NV_P}{V_0} = \frac{N}{R_0^3} \quad (3.2)$$

where  $R_0$  is the radius of the cluster when  $\delta_0 \rightarrow 0$ ,  $V_0$  its volume and  $V_P$  is the volume of a single elementary particle. Increasing  $\delta_0$  leads to an increasing of  $\zeta$  as well. With the previous assumptions  $\zeta_0$  is constant and independent from the cluster size, and represents the packing of the elementary particles inside the cluster. For  $\delta_0 \rightarrow 0$  the cluster radius will also become independent on the average overlap, and by re-arranging Eq. 3.2 the following relation is obtained [9]:

$$R \xrightarrow{\delta_0 \rightarrow 0} R_0 = \sqrt[3]{\frac{N}{\delta_0}}$$

Given the cluster homogeneity and isotropy, crossing a cluster in radial direction  $\zeta$  represent the possibility of finding at least one particle in a single point; moreover the number of particles on a diameter  $n$  is proportional to  $\zeta_0$  and  $2R_0$ , that is  $n \approx \zeta_0 R_0$ . Compressing a cluster of a quantity  $\Delta = 2(R_0 - R)$  would result in an average particle deformation of  $\delta = \frac{\Delta}{2N}$ , where the 2 factor in the lower member of the fraction accounts for each particle for being overlapped twice in the direction of compression. Combining these last statements, a measure of  $R$  depending on the overlap is obtained:

$$R = R_0 - R_0 \zeta_0 \delta$$

As explained before, during compression particles are pushed together so that at the end of the process  $\delta = \bar{\delta}_0 \simeq \delta_0$ . Then it holds

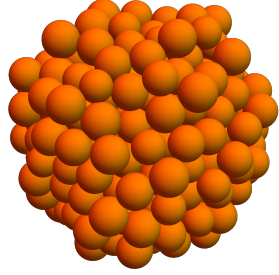
$$R = R_0 - R_0 \zeta_0 \delta_0 = \sqrt[3]{\frac{N}{\delta_0}} (1 - \zeta_0 \delta_0) \quad (3.3)$$

Similarly for the solid fraction, approaching linearly because of small overlaps between particles, it holds:

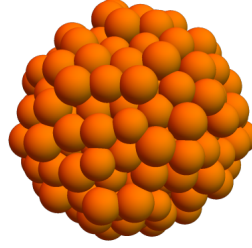
$$\zeta = \zeta_0 + 3\zeta_0^2 \delta_0, \quad (3.4)$$

where  $\zeta_0 = 0.58$  has been empirically determined. Concluding, it is interesting to notice, as stated before, that variations in values of  $R$  and  $\zeta$  can be also produced by changing the value of sliding friction coefficient  $\mu$ , tangential stiffness  $k_t$  and cohesive stiffness  $k_c$  but their contribution is small and can be neglected.

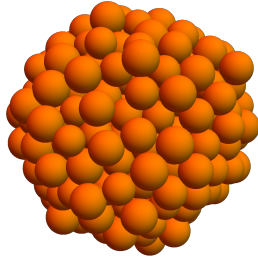
### 3.2 One dimensional compression for a single cluster



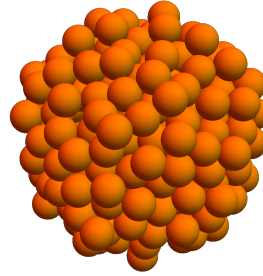
(a)  $\mu = 0.5, \delta = 0.1, \sigma_s = 1.2.$



(b)  $\mu = 0.5, \delta = 0.3, \sigma_s = 1.2.$



(c)  $\mu = 0.0, \delta = 0.1, \sigma_s = 1.2.$



(d)  $\mu = 0.5, \delta = 0.1, \sigma_s = 1.0.$

**Figure 3.2:** Picture of the four different clusters mentioned before: as can be seen the major difference in shape occurs when changing values of penetration depth  $\max \delta_0$  (b).

In the previous section variations in solid fraction and cluster radius have been defined and in particular an analytic relation between them and plasticity depth was shown. Anyway, considering the cluster as a single entity, other physical and mechanical properties can be studied. Since a single cluster is made by several elementary particles its behaviour and the results obtained when a stress is applied to it are very different from what is obtained when compressing a single elementary particle. Its discrete nature and the frictional and cohesive interactions among the elementary particles led to a mechanical behaviour which is far apart from the one of the single particle. For these reasons a parameter called *equivalent cluster stiffness*  $k_{eq}$  is now defined:

$$k_{eq} = \frac{1}{Z} \int_0^{\bar{Z}} F(z) dz$$

**Table 3.1:** Values obtained for equivalent stiffness  $k_{eq}$  and radius  $R$  in uniaxial compression of a single cluster.

$\mu$	$\delta_0$	$\sigma_s$	$R$	$\frac{k_{eq}}{\frac{KN}{m}}$	Figure
0.5	0.1	1.2	80.4	8.01	3.2a
0.5	0.3	1.2	71.0	39.7	3.2b
0.0	0.1	1.2	80.2	3.46	3.2c
0.5	0.1	1.0	79.5	6.04	3.2d

where  $F$  is the force measured during a uniaxial compression,  $z$  is the vertical displacement and  $\bar{Z}$  is the total vertical displacement (here  $\bar{Z} = 0.3R$ ). This parameter, anyway, is useful to characterize differences among different clusters, but is not related to other results in this study. Various simulations were performed in which a single cluster was compressed uniaxially in order to measure the dependency of  $k_{eq}$  and  $R$  from some basic parameter, such as: sliding friction  $\mu$ , particle size dispersity  $\sigma_s$  and penetration depth max  $\delta_0$ . Micro parameters and output results are shown in Table 3.1, in which the stiffness of a single microparticle is set to  $10\frac{KN}{m}$ . As can be seen, while changing  $\mu$  and  $\sigma_s$  lead to minor changes in radius and stiffness, changing the value of the penetration depth max  $\delta_0$  leads to major changes both in radius and stiffness. The same can be said when taking into account the appearance and shape of those clusters, shown in Figure 3.2. The steps needed to create and use clusters with the MercuryDPM software are shown in Appendix A.2 along with a few useful lines of code.

One more important step, in the characterization of one dimensional compression of clusters, is to define the effect of size and strain rate on results: as will be seen these parameters not only modify the shape of the simulation and its computational time, but also the reliability and the accuracy of the obtained results. In the next sections the outcome obtained for different values of strain rate and cluster size will be shown and the chosen values will be defended, but before proceeding it is necessary to state the definition of stress for a DEM simulation. Stress tensor in a DEM simulation with a set  $M$  of interactions among particles is defined as [13]:

$$\sigma_{ij} = \frac{1}{V} \sum_{m \in M} f_i l_j \quad (3.5)$$

where  $V$  denotes the volume of the simulation,  $m$  denotes a single interaction in the set  $M$ ,  $\vec{f}$  is the force transmitted by the contact, defined in Eq. 2.7 and  $\vec{l}$  is the branch vector connecting the two centers of the particle being in contact in interaction  $m$ . Isotropic stress and vertical stress will be consequently defined respectively as:

$$\sigma_I = \frac{tr\sigma}{3}, \quad \sigma' = \sigma_{ZZ}$$

### 3.2.1 Study of size effects

The size of a single cluster composing the domain of the simulation can influence results not only because of a change in the shape of the domain but also because clusters composed by a different number of particles behave differently. For this reason, in this section the size of a cluster will be characterized by the number  $N$  of particles composing it, instead of its relative radius  $\hat{R}$ . In figure 3.3 it is shown a comparison in the results of a single cluster compression, for clusters made by a number of particles that varies from 50 to 350. The value

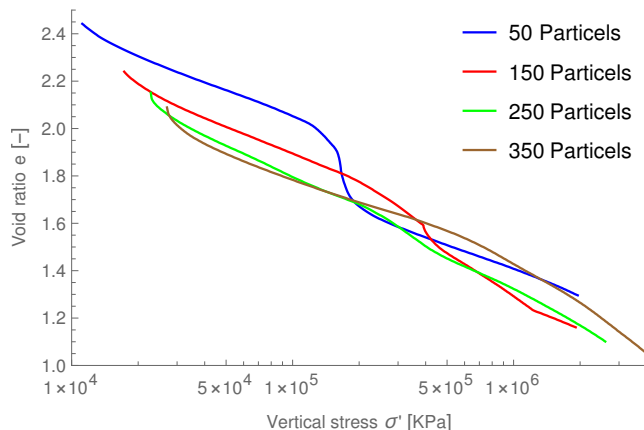


**Figure 3.3:** Compression comparison for different clusters sizes.

of stress showed are obtained imposing  $k_1 = 10^3$ ,  $k_2 = 5 \cdot 10^3$ ,  $k_c = inf$ . As can be seen the uniaxial compression of a single cluster does not present significant differences with the variation of the size; nevertheless it is interesting to notice the presence of jumps in the stress values in each of the four cases: this is because of internal breakages which occur during the compression. Given the absence of significant differences among these results the present work will be carried on using clusters composed by 50 particles: this way, for the same total number of elementary particles (and so a similar computational time), it will be possible to simulate more clusters, reducing the fluctuations given by breakages and possible inhomogeneities within the domain.

### 3.2.2 Strain rate effect

Similarly to what has been done for cluster size, it is also important to verify the influence of strain rate  $\dot{\epsilon}$  on the simulation. All the simulations proposed in this work are indeed performed compressing the computational domain with a constant strain rate (as will be seen in detail in Chapter 4). Before proceeding with the results it is important to clarify that values for strain rate defined from now on are defined as strain per iteration and not strain per time:

$$\dot{\epsilon} = \frac{L^{n+1} - L^n}{L^n}$$

where  $L$  represents the simulation domain length and the superscripts  $n$  and  $n + 1$  refers respectively to the  $n$ -th and  $n + 1$ -th time step and not to the

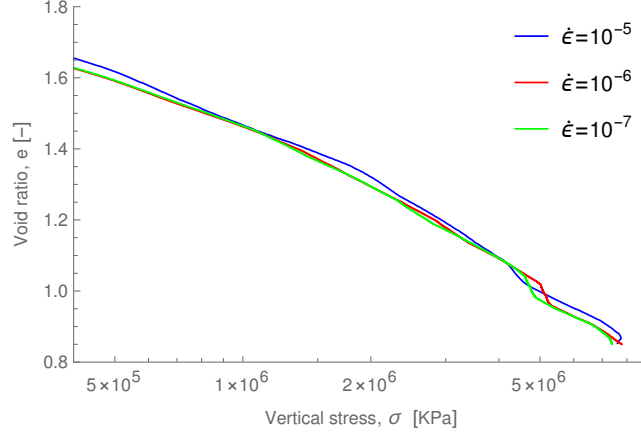


**Figure 3.4:** Comparison of results for compression in a single cluster with three different strain rate values.

simulation time. In Figure 3.4 it is shown a comparison of a compression process with three different strain rate values:  $10^{-5}$ ,  $10^{-6}$  and  $10^{-7}$ . As can be seen, also in this case it is not possible to find significant differences. Nevertheless, it is important to remember that an oedometric compression, which is what will be simulated in the next chapter, is a very slow process and it can indeed be considered as static. When such a test is simulated with DEM it is necessary to verify two more requirements:

- the first one involves the ratio between the kinetic energy  $K$  and elastic energy  $U$  of the discrete system; it is good practice to verify that

$$\frac{K}{U} \leq 10^{-5}, \quad K = \sum_{i=1}^N \frac{1}{2} m_i \|\mathbf{v}_i\|_2^2, \quad U = \sum_{j=1}^M \frac{1}{2} k_1 \delta_j^2$$

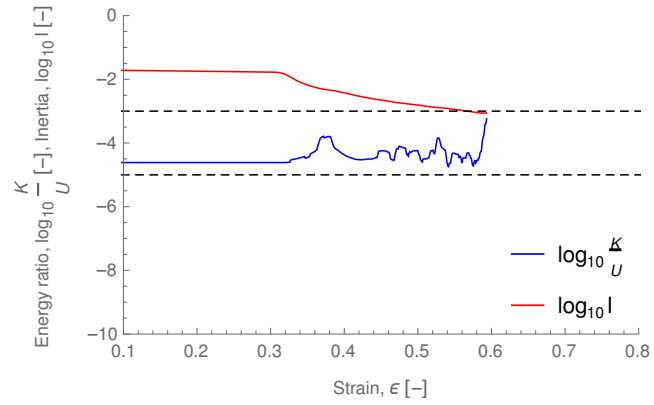
where  $N$  is the total number of particles in the system,  $m_i$  and  $\mathbf{v}_i$  are mass and velocity of the  $i$ -th particle,  $M$  is the total number of interactions in the system and finally  $\delta_j$  is the  $j$ -th interaction.

- the second one involves the inertia  $I$  of the discrete system; similarly in this case it is good practice to verify that

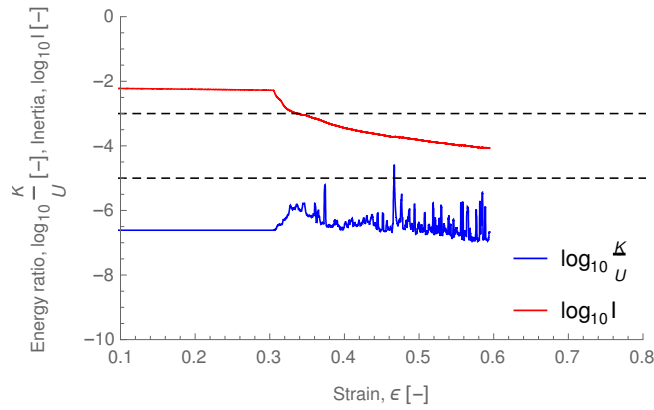
$$I = \frac{-2r\dot{\epsilon}}{\sqrt{\frac{\sigma_Z}{\rho}}} \leq 10^{-3}$$

where  $\sigma_Z$  represents the stress in the vertical ( $Z$ ) direction in the system and  $\rho$  is the density of a single particle.

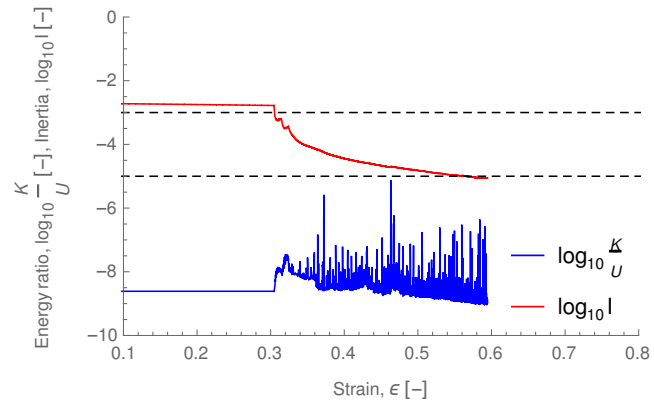
In Figure 3.5 it is shown a comparison among these values for each one of the studied strain rate values. As can be seen, while for  $\dot{\epsilon} = -10^{-6}$  and  $\dot{\epsilon} = -10^{-7}$  the requirements listed above are respected, when  $\dot{\epsilon} = -10^{-5}$  the inertia and energy ratio values are higher than the desired ones. For this reason the value use for strain rate in this work will be  $\dot{\epsilon} = -10^{-6}$ . Following the considerations made in the previous sections, the clusters in this work will be made by 50 particles and the strain rate applied to the domain will be  $\dot{\epsilon} = -10^{-6}$ .



(a)  $\dot{\epsilon} = -10^{-5}$ .



(b)  $\dot{\epsilon} = -10^{-6}$ .



(c)  $\dot{\epsilon} = -10^{-7}$ .

**Figure 3.5:** Comparison of energy ratio  $\frac{K}{U}$  and inertia  $I$  values for the three different strain rates.

### 3.3 Workable characteristics

In the previous section strain rate and size of the cluster were studied. It is important to notice, anyway, that those parameters are related more to

the simulation than to the cluster itself. In this section the two main factors influencing the cluster shape and size will be discussed and analysed: mass fraction and cluster radius.

### Mass fraction

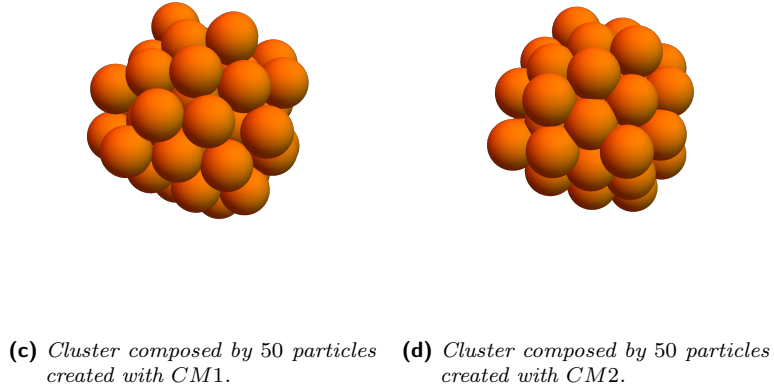
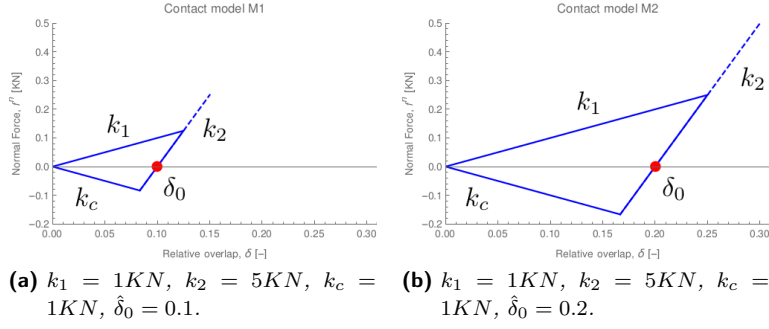


**Figure 3.6:** Contact models M1 and M2 and corresponding 50 particles clusters.

The first parameter that needs to be studied is the mass fraction of a single cluster. When simulating soil or powders or any structure characterised by dual porosity, i.e. a structure composed by discrete agglomerations with internal porosity, micro void ratio is defined by the void ratio of a single cluster. As discussed in Section 3.1 the mass fraction of a single cluster can be defined starting from the average overlap among the particles composing the cluster as:

$$\zeta = \zeta_0 + 3\zeta_0^2\delta_0$$

A natural consequence of this behaviour is that the mass fraction of a single cluster is directly related to the contact model specified in the simulation. In Figure 3.6 two different contact models  $CM1$  and  $CM2$  are shown by their scheme: while  $k_1 = 1KN$ ,  $k_2 = 5KN$  and  $k_c = 1KN$  for both contact models, relative penetration depth max  $\hat{\delta}_0$  is different, being  $\hat{\delta}_0 = 0.1$  for  $CM1$  and  $\hat{\delta}_0 = 0.2$  for  $CM2$ . In addition two clusters created with  $CM1$  and  $CM2$  are shown.

### Cluster radius

The radius of a cluster depends on more than one parameter: it is affected by the number of particles  $N$ , by the average overlap among particles  $\hat{\delta}$  and by the radius of a single particle  $r$ . It is important to notice however that the first one of these parameters is already fixed: the total number of particles composing a cluster will be set to  $N = 50$  throughout this study. Regarding the value of the average overlap among particles, it is directly controlled by the value of penetration depth *max delta*, and so by the contact model. This same parameter anyway will be tuned in order to define the mass fraction of the cluster, given that it is the only parameter that can fulfill this purpose. For these reasons the radius of a cluster will be only tuned modifying the radius of a single particle  $r$ . This way if a certain mass fraction  $\bar{\zeta}$  is needed, the required  $\delta_0$  will be:

$$\hat{\delta}_0 = \frac{\bar{\zeta} - \zeta_0}{3\zeta_0^2}$$

and consequently the relative cluster radius will be:

$$\hat{R} = \sqrt[3]{\frac{N}{\hat{\delta}_0}} (1 - \zeta_0 \hat{\delta}_0)$$

Remembering that the normalised cluster radius  $\hat{R}$  is defined as  $\hat{R} = \frac{R}{r}$  the desired value for the cluster radius is easily obtained as:  $R = r\hat{R}$

## Chapter 4

# Mechanical loading

In this chapter the results obtained by the numerical simulations of mechanical compression of clays will be shown. In particular, after a first section in which the inadequacy of a single porosity model in reproducing experimental results relating to the uniaxial compression of a clay will be shown, the double porosity simulations will be characterized: chosen micro-parameters will be presented, obtained after a first phase of calibration, and the numerical results will be compared directly with the experimental tests. Finally, the validation of the numerical model will be proposed, obtained by simulating experimental data coming from the uniaxial compression of the same clay sample, placed under different chemical conditions. Throughout the discussion, great importance will be given to the relationship between the behavior of the clay at the micro-scale and the macroscopic behaviour under the effects of mechanical loads.

### 4.1 Parameter calibration

A great problem encountered during the simulations was to define the parameters that could better define the experimental data. The number of parameters that can be defined is indeed large; a few examples of parameters that can be tuned are:  $k_1$ ,  $k_2$ ,  $k_c$ , friction  $\mu$ , tangential stiffness  $k_t$  and particles size dispersity  $D_s$ ; with such a large set of parameters, finding the values that better approximate the experimental values is very complicated; moreover, using clusters to simulate clay particles agglomerates, each one of those parameters can be defined taking into account the interaction both between particles belonging to the same cluster and between particles belonging to different clusters. This way the set of parameters becomes:  $k_1^i, k_2^i, k_c^i, \mu^i, k_t^i, D_s^i$  and  $k_1^I, k_2^I, k_c^I, \mu^I, k_t^I, D_s^I$  where superscripts  $i$  and  $I$  define intra-cluster and inter-cluster interactions respectively (this will not be true in case of single porosity simulations, where only inter-cluster parameters will come into consideration). In addition to this, some parameters may have a greater influence on the simulation than other, or it is possible that some parameters may have a minimal influence on the simulation results to the point that it is convenient to fix them. Therefore, a software called GrainLearning [7] was used to calibrate parameters: it is a Python language written toolbox based on an iterative Bayesian filter able to find optimal parameters for DEM simulations, which are often characterised by

**Table 4.1:** Void ratio  $e$  and vertical stress  $\sigma'$  measured during uniaxial compression of FEBEX bentonite samples obtained by [4], taking into account two different interstitial fluid compositions.

<i>Distilled water</i>		<i>Saline Solution</i> <i>5.5M NaCl</i>	
$e$	$\sigma'$ [KPa]	$e$	$\sigma'$ [KPa]
0.96	500	0.72	500
0.93	1000	0.68	1000
0.85	2000	0.60	2000

nonlinearities and whose parameters are usually difficult to calibrate. Starting from results obtained by a set of simulations computed with random values, the first iteration of the GrainLearning will provide a new set of values on which simulations will be computed again and so on. If the set of parameters chosen is able to define the problem sufficiently accurately, the optimal values will be obtained after about three iterations, which means running simulations four times. Further explanation about GrainLearning and its properties can be found in Appendix B.

### Experimental data

The first objective of this study is the reproduction of experimental data obtained from the mechanical compression of a FEBEX clay sample. In particular the experimental data refers to two different samples: one saturated with distilled water, while the other one with a 5.5M concentration of *NaCl* saline solution. Changes in void ratio and vertical stress are presented for both samples in Table 4.1. In order to get a better representation of the data they have been interpolated with a polynomial in order to get a compression curve. Experimental points and compression curves are represented in Figure 4.1.

### Dimensions of clay aggregates

The first step in order to set parameters for the numerical simulation is to define a radius  $r$  for particles. Considering that in this preliminary study no micro-porosity is taken into account, a single spherical particle represent a single clay agglomerate: for this reason, in order to define a good measure for  $r$  it is necessary to define an acceptable value for the average size of a clay particle. In order to do so, the two MIP (Mercury Intrusion Porosimetry) tests for FEBEX clay shown in Figure 4.2 were taken into account; these tests were carried out on two different samples: the first one obtained after the preparation for compaction and the second one after the introduction of distilled water into the sample. As it is possible to see, after the swelling process, the curve changes from having two modes to having only one. Moreover, it is safe to say that the swelling caused by distilled water is larger than the one that would be obtained substituting a saline solution. For these reasons, as a threshold between micro and macropores it has been chosen 1000nm, corresponding to the value for which the PSD (*Pore*

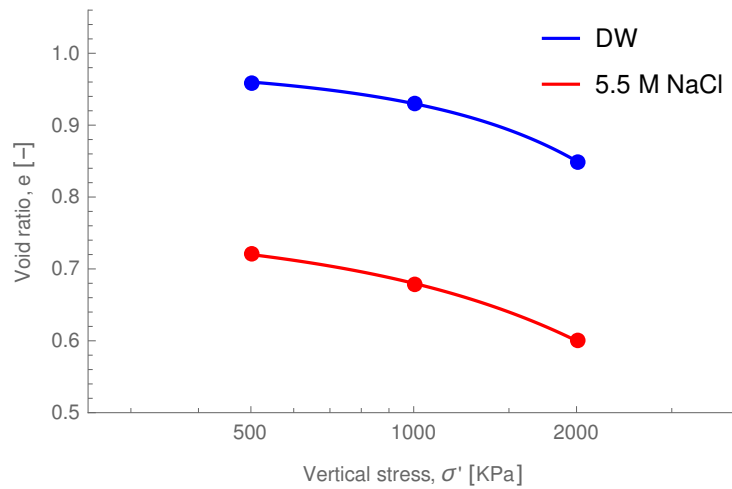


**Figure 4.1:** Experimental compression data and compression curve.

*Size Distribution*) curve has a maximum: it is indeed a good representation of the maximum value for micropores and of the minimum value for macropores. Starting from this value it is possible to define the value of the average diameter

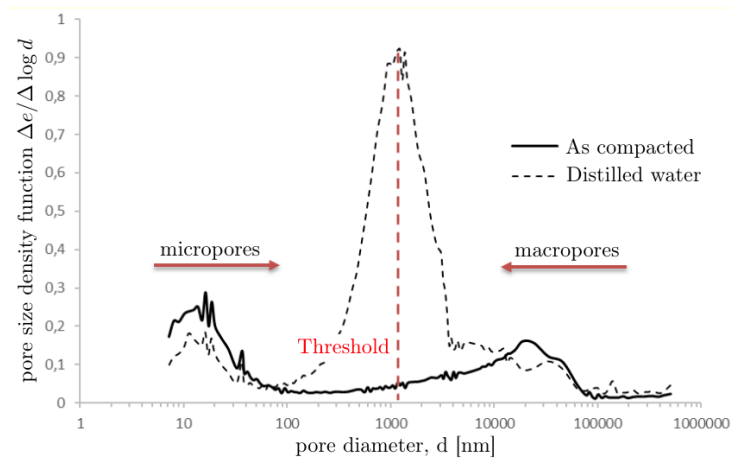


**Figure 4.2:** PSD variation obtained after swelling and assessment of the threshold between micro and macro void ratio. [5]

for macropores  $\bar{d}$ . This value can be computed considering that during the execution of MIP tests mercury is injected with a pressure value that increases linearly with time: as the pressure increases smaller pores are traced. It is then possible to associate a generic pressure  $p_i$  to a particular pore diameter  $d_i$ , which corresponds also to an incremental void fraction  $\Delta e_i$ . Defining  $n$  pore families it is possible to characterise the cumulative curve shown in Figure 4.3: to each  $\Delta e_i$  increment corresponds a different pore family having diameter  $d_i$ . Starting

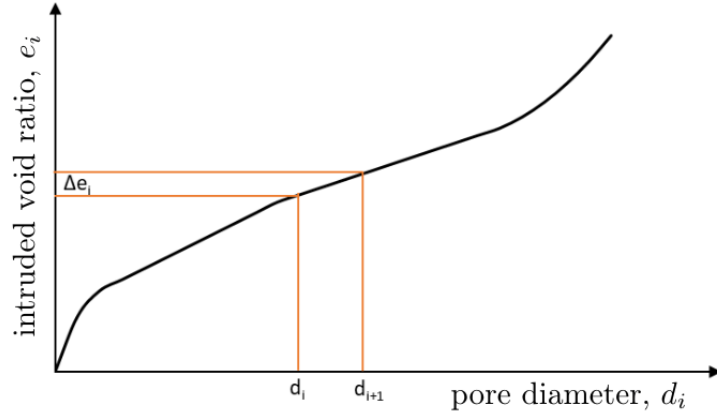


**Figure 4.3:** Intruded void ratio cumulative curve.

from these considerations it holds:

$$\sum_{i=1}^n \Delta e_i d_i = \sum_{i=1}^n \bar{d} \Delta e_i ;$$

considering that the total variation of void ratio  $e$  can be defined as:

$$e = \sum_{i=1}^n \Delta e_i ,$$

it is now possible to define a measure for the average pore diameter as  $\bar{d}$ :

$$\bar{d} = \frac{1}{e} \sum_{i=1}^n d_i \Delta e_i . \quad (4.1)$$

One more step is necessary for this study: given that in this work clay aggregates are represented as spherical objects, the average clay aggregate dimension has to be computed over macro void ratio  $e_M$ , and the same has to be done for the average pore dimension:

$$\bar{d}_M = \frac{1}{e_M} \sum_{j=1}^m d_j \Delta e_j , \quad (4.2)$$

where  $m$  is the number of macropore families and  $e_M$  is the total variation of macro void ratio

$$e_M = \sum_{j=1}^m \Delta e_j .$$

All results obtained from these considerations are shown in Table 4.2, both for distilled water and 5.5M NaCl saline solution. In order to define relationships between the pore diameter, from now on referred to as  $d_{pore}$ , and the aggregate diameter,  $d_{agg}$ , and considering that the study will be carried out representing clay aggregates as spherical objects, the values for  $e_M$  shown in Table 4.2 have been compared with those of some regular fabrics, such as: cubic, tetrahedral,

**Table 4.2:** Values of the average pore diameters and void ratio obtained by MIP tests.

	$\bar{d}$ [nm]	$e$	$e_M$	$e_m$
<i>Distilled water</i>	$2.50 \cdot 10^4$	0.99	0.37	0.45
<i>NaCl 5.5M</i>	$8.10 \cdot 10^4$	0.75	0.46	0.20

pyramidal, tetrahedral cubic, sphenoidal tetragonal. The only fabrics matching this values are the tetrahedral cubic for distilled water, having  $e_M = 0.35$  and a ratio between the two diameter  $d_{pore}/d_{agg} = 0.23$ , and the pyramidal for NaCl 5.5M saline solution, having  $e_M = 0.43$  and a ratio between the two diameter  $d_{pore}/d_{agg} = 0.46$ . Therefore it holds:

$$d_{agg}^{H_2O} = \frac{d_{pore}^{H_2O}}{0.23} = 110\mu m ,$$

where the superscript  $H_2O$  indicates distilled water as interstitial fluid. Regarding the diameter of the aggregate with saline solution as interstitial fluid,  $d_{agg}^{NaCl}$ , considering that

$$V_{agg} = V_s(1 + e_m) ,$$

it is possible to define the following ratio

$$\frac{d_{agg}^{H_2O}}{d_{agg}^{NaCl}} = \sqrt[3]{\frac{1 + e_m^{H_2O}}{1 + e_m^{NaCl}}} = 0.94 ,$$

from which

$$d_{agg}^{NaCl} = 0.94d_{agg}^{H_2O} = 100\mu m .$$

Throughout this work, based on the studies just carried out, the radius of clay aggregates in the case of distilled water  $r^{H_2O}$  and saline solution  $r^{NaCl}$  will be

$$r^{H_2O} = 55\mu m, \quad r^{NaCl} = 50\mu m . \quad (4.3)$$

$$r^{H_2O} = 55\mu m, \quad r^{NaCl} = 50\mu m .$$

## 4.2 Single porosity: preliminary study

Before proceeding with the double porosity numerical tests, some single porosity simulations were carried out to verify the ability of these tests to reproduce the experimental data. The expression *single porosity tests* here indicates those numerical simulations in which the micro-porosity of clay aggregates is not taken into account. The latter will then be simulated through single spherical, non-deformable elementary particles. The simulation will be performed through the following steps:

- deposition: particles are placed in the domain with no interactions among them; they are then free to settle and rearrange thanks to the application of the strain rate that makes them deposit;

**Table 4.3:** Results of experimental tests of FEBEX bentonite, taking into account macro void ratio  $e_M$  and micro void ratio  $e_m$ .

<i>Distilled water</i>				<i>Saline Solution 5.5M NaCl</i>			
$e$	$e_M$	$e_m$	$\sigma'$ [KPa]	$e$	$e_M$	$e_m$	$\sigma'$ [KPa]
0.96	0.35	0.45	500	0.72	0.43	0.2	500
0.93	0.33	0.45	1000	0.68	0.40	0.2	1000
0.85	0.28	0.45	2000	0.60	0.33	0.2	2000

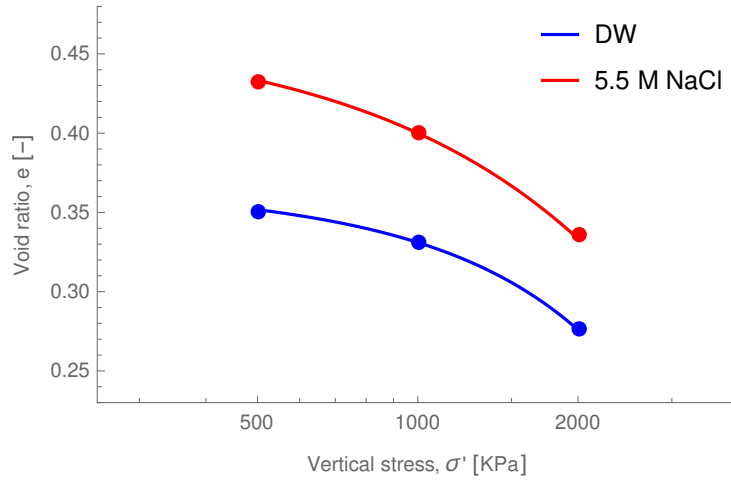


**Figure 4.4:** Experimental compression data and compression curve for single porosity simulations.

- isotropic compression: the sample is compressed isotropically thanks to periodic boundaries in order to get the void ratio value corresponding to that of the beginning of the experimental tests;
- uniaxial compression: this is the last part of the numerical simulation; particles are compressed uniaxially in vertical direction until the value of void ratio is equal to the one of the experimental test.

In Table 4.3 experimental data have been rescaled in order to take into account only macro void ratio. In the same way as the original ones, they have been interpolated to obtain a larger dataset. The results are shown in Figure 4.4. Considering now simulation parameters, with a few preliminary simulations it has been discovered that  $k_c$  had quite a low influence on simulation results and the same could be told about  $k_2$ . Considering moreover the negligibility of van der Waals' attractive forces compared to the Coulomb repulsive forces the following choice have been made:

$$k_1 = k_2 \Rightarrow k_c = 0, \delta = 0.$$

Therefore four parameters have been tuned in this simulation:

- particle size dispersity  $D_s$ , ranging from 1.2 to 10: in particular, starting from the average particle radius  $r$ , the radius of the  $i$ -th particle will be computed randomly as:

$$r_i = r \text{ rand} \left( \frac{2}{1 + D_s}, \frac{2D_s}{1 + D_s} \right) ;$$

- loading stiffness  $k_1$ , ranging from  $0.1KN$  to  $5KN$ : this parameter has no real limits, other than being positive, so the range has been set as large as possible;
- sliding friction coefficient  $\mu$ , ranging from 0 to 0.3: considering values in table 4.3 in case of distilled water the starting point of the simulation is  $e_M = 0.35$ ; this value is very low even if compared to random close packing values ( where  $e \simeq 0.66$ ). The small interval for  $\mu$  here has been set in order to get a system as dense as possible.
- relative tangential stiffness  $rk_t$ , ranging from 0 to 1: this parameters sets the ratio between  $k_n$  and  $k_1$  in a contact between two particles as

$$rk_t = \frac{k_n}{k_1} .$$

As a value for strain rate  $\dot{\epsilon}$  the same results obtained for cluster strain rate were used, given that the strain process is the same in the two simulations; differently, for the number of particles  $N$  a study was carried out in order to verify that the number of particles in the simulation is large enough. In Figure 4.5 a confrontation among simulations having the same micro-parameters but different number of particles is shown. As it is possible to notice, there is no

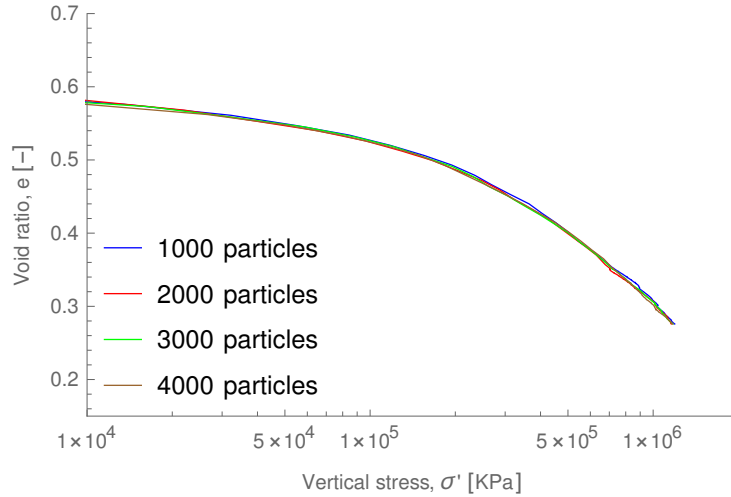


**Figure 4.5:** Confrontation among simulations having number of particles ranging from 1000 to 4000.

great difference in results, and instead they are almost perfectly overlapped. For this reason in single porosity simulations the number of particles will be set to  $N = 1000$ .

### 4.2.1 Numerical simulation

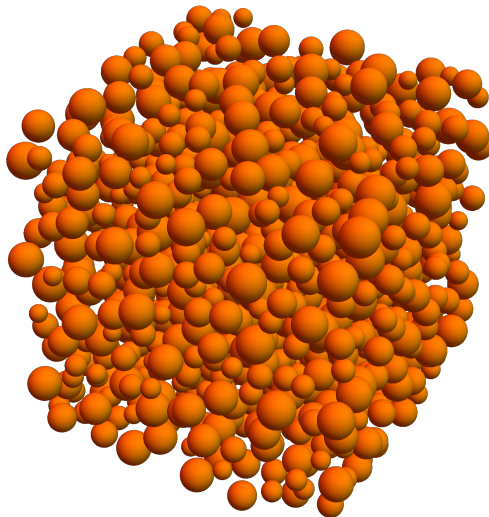


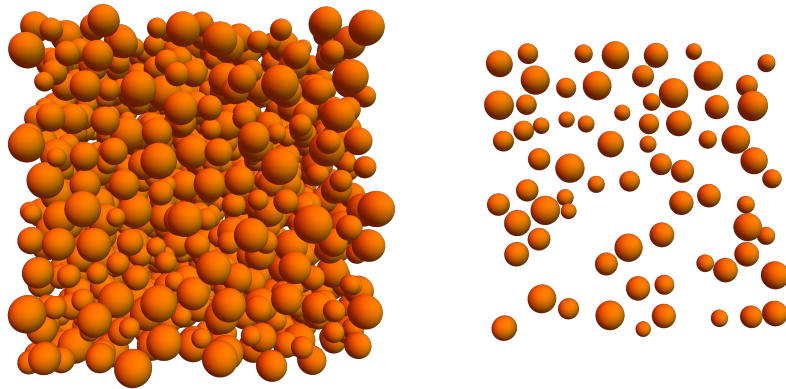
**Figure 4.6:** 3D view of the numerical simulation.

In this section single porosity numerical simulations will be studied with particular interest in the results obtained thanks with GrainLearning. In Figure 4.6 it is possible to see an isometric view of the computational domain; it is important to remark here that the domain is defined by periodic boundaries: each particle placed at the edge of the domain can for this reason be in touch with a particle placed on the opposite side. This way no walls are present in the simulation and the edge effects are minimized. In Figure 4.7 all principal stages of the simulation are shown with a frontal view:

- first row, stage 1: it is possible to see particles in the initial state; no interactions are present and the domain is in a gas-like state, Figure 4.7a and 4.7b;
- second row, stage 2: jamming point; particles have got into contact but interaction forces are still low, Figure 4.7c and 4.7d;
- third row, stage 3: starting of uniaxial compression; the system has void ratio  $e_{M_0} = 0.35$ , Figure 4.7e and 4.7f;
- fourth row, stage 4: ending of simulation; the domain is not a cube anymore and void ratio  $e_{M_0} = 0.28$ , Figure 4.7g and 4.7h.

For each stage, moreover, a section is shown, showing only particles placed in a *slice* of the domain having width  $L = 2r$ . In order to get the best results, three iterations of GrainLearning were necessary, after which no improvement were detected. In figure 4.8 the new parameterizations obtained after each iteration are shown: in this study, for each iteration of GrainLearning 70 numerical simulations have been run simultaneously. In all three subplots the blue points

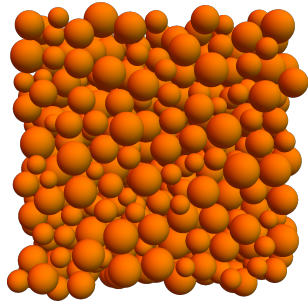
indicate the numerical values used for the simulations just performed, while the orange ones represent the new parameters with which the numerical simulations will subsequently be launched. For this reason blue points of Figure 4.8b match orange points of Figure 4.8a and blue points of Figure 4.8c match orange points of Figure 4.8b; blue points in figure 4.8a and orange points in 4.8c represent respectively the random starting set of values and the final best set of values. Finally the best three solutions obtained by the third and last iteration are shown in Figure 4.9. As it is possible to notice, with this model it is not possible to obtain good results.



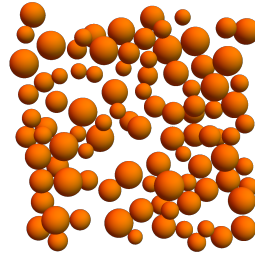
(a) *Front view of stage 1.*

(b) *Section of stage 1.*

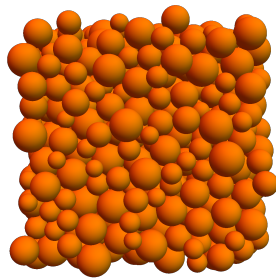
**Figure 4.7:** 3D plot frontal view of compression stages.



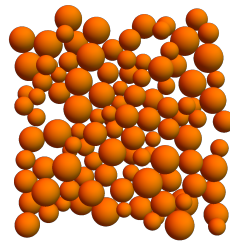
**(c)** *Front view of stage 2.*



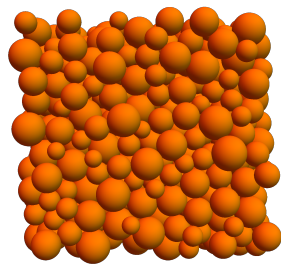
**(d)** *Section of stage 2.*



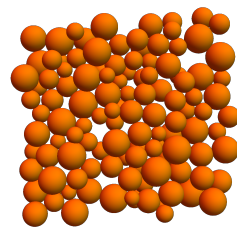
**(e)** *Front view of stage 3.*



**(f)** *Section of stage 3.*

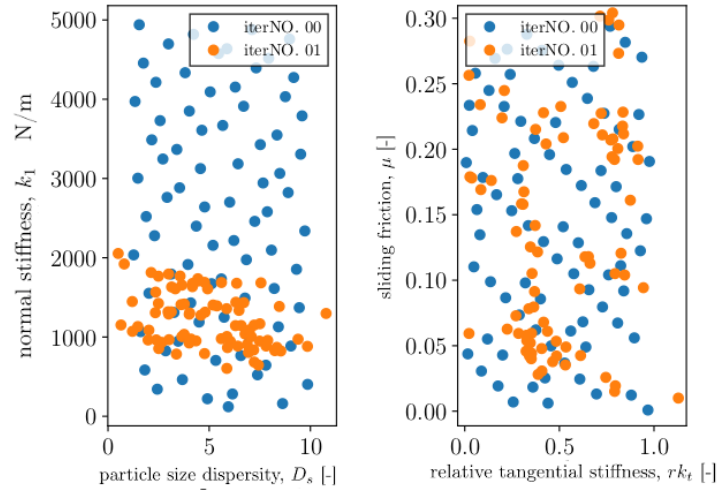


**(g)** *Front view of stage 4.*

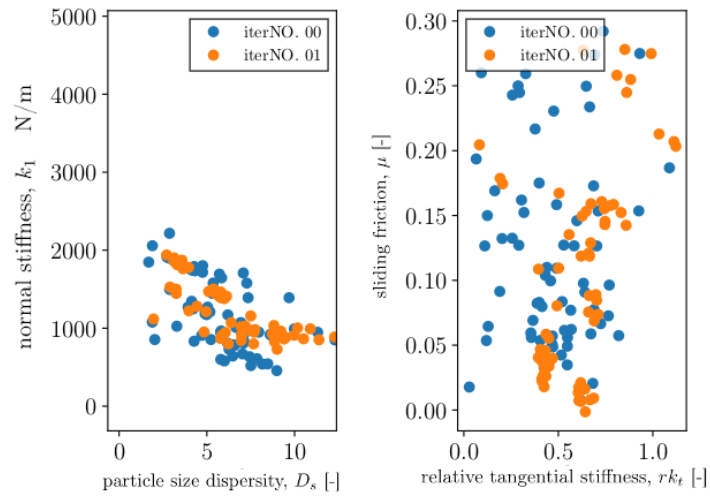


**(h)** *Section of stage 4.*

**Figure 4.7:** 3D plot frontal view of compression stages.

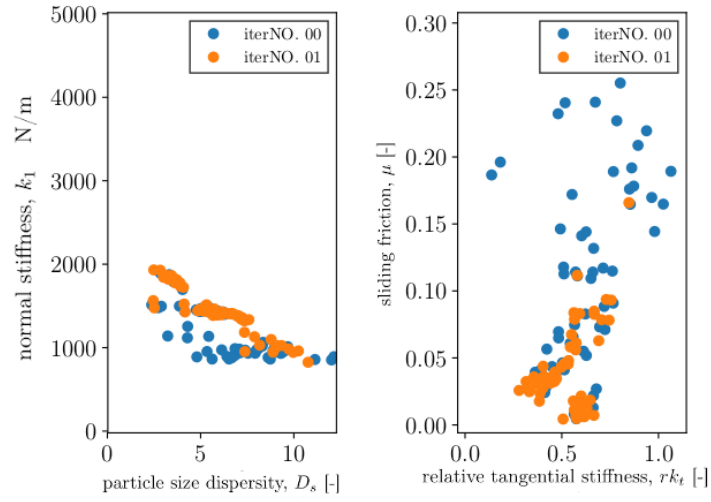


(a) *GrainLearning* parameter space iteration 1.



(b) *GrainLearning* parameter space iteration 2.

**Figure 4.8:** Evolution of parameter space.



(c) *GrainLearning* parameter space iteration 3.

**Figure 4.8:** Evolution of parameter space.

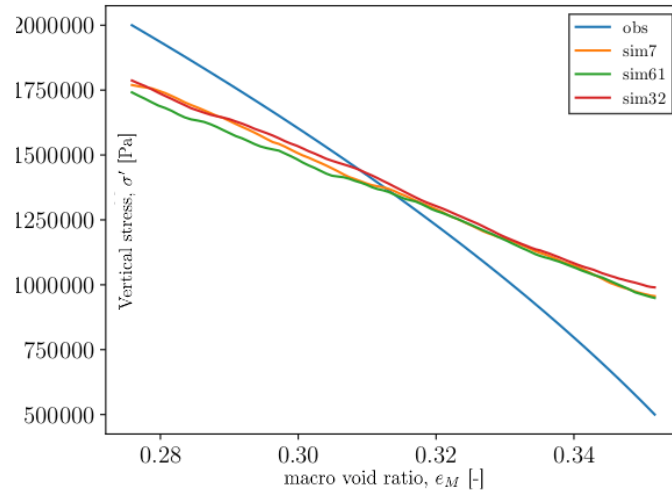


**Figure 4.9:** Results obtained by the third iteration of *GrainLearning*.

A few considerations anyway can be made analyzing the evolution of parameter space shown in the maps of Figure 4.8a, 4.8b and 4.8c, for each one of the tuned parameters:

- loading stiffness  $k_1$ : it is the parameter that has been most characterized. final values fluctuate between  $k_1 = 1 \cdot 10^3$  and  $k_1 = 2 \cdot 10^3$ ;
- particle size dispersity  $D_s$ : in all three iteration no effect of dispersity have been found. This parameter does not have evident effects during numerical simulations and therefore in the next studies it will be set to  $D_s = 1.2$
- relative tangential stiffness  $k_t$ : after three iterations optimal values for this parameter fluctuate between  $k_t = 0.4$  and  $k_t = 0.6$ . In double porosity simulation this parameter will again taken into account.
- sliding friction  $\mu$ : apparently an optimal value for this parameter has not been found. Anyway this could depend on the short initial range on which it has been tuned. In double porosity simulations it will be again taken into account with a wider range for intra-cluster interactions (i.e. between particles belonging to the same cluster).

### 4.3 Compression of clusters with water-like fluid

In this section, double porosity simulations will be discussed. Differently from the previous section, clay agglomerates will now be represented by spherical clusters defined in Chapter 3, and therefore micro and macro void ratio will be defined throughout the presentation. Regarding numerical simulations, these are set differently than in the case of single porosity, as they are carried with the following steps:

- deposition: clusters are placed in the domain with no interactions among them; they are then free to settle and rearrange thanks to the application of the strain rate that makes them deposit;
- first isotropic compression: the sample is compressed isotropically thanks to periodic boundaries in order to get the void ratio value corresponding to that of the beginning of the experimental tests,  $e = 0.96$ ;
- second isotropic compression: the sample is compressed isotropically thanks to periodic boundaries in order to get the stress  $\sigma$  corresponding  $\sigma = 20\sigma$  ( $e = 0.96$ ). This is done in order to simulate the process of clay sample compaction;
- system relaxation: periodic boundaries are moved in the opposite direction with the same strain rate in absolute value until void ratio is  $e = 1.02$ ;
- uniaxial compression: domain is compressed in the vertical direction in order to simulate the oedometric test, until  $e = 0.85$ . Results obtained during this step are compared with experimental data showed in figure 4.1 and Table 4.3;

Differently from single porosity simulations, as stated before, for each parameter two values has to be defined as interactions between elementary particles can be found both between particles belonging to the same cluster and between particles belonging to two different clusters; it is important to notice that all considerations made in the previous section will be now valid for inter-cluster values, as particles before were representative of a clay agglomerate. Here the choices made for each parameter will be detailed. Starting from particle size dispersity  $D_s$ , from the previous section it has been discovered that it has not a strong influence on numerical simulations and for this reason it will be set constant to:

$$D_s^i = 1.2, \quad D_s^I = 1.2;$$

the choice of imposing a size dispersity also between elementary particles has been made to avoid the creation of crystal lattice dispositions. Regarding contact model parameters different considerations have to be made in the two different cases. For intra-cluster parameters a linear-contact model have been imposed:  $k_1^i$ ,  $k_2^i$  and  $k_c^i$  are proportional to each other as

$$k_2^i = 5k_1^i, \quad k_c^i = \alpha k_2^i.$$

The reasons behind this choice is that after a few preliminary simulations it has been discovered that the ratio between  $K_1^i$  and  $k_2^i$  has no particular influence on the simulation, while setting  $k_c^i = \alpha k_2^i$  is necessary in order to tune cluster

**Table 4.4:** Normalised compression curve values

<i>Distilled water</i>		
$e$	$\sigma'$ [KPa]	$\frac{\sigma'}{\sigma_{ref}}$
$e_0 = 0.96$	500	1
$e_i = 0.93$	1000	2
$e_f = 0.85$	2000	4

behaviour, as with  $\alpha < 1$  the cluster is more fragile while with  $\alpha \geq 11$  it is stiffer. The only parameter tuned among these is  $\alpha$ , from now on referred to as *relative cohesive stiffness*  $rK_c = \frac{k_c}{k_2}$ , as  $k_2$  will be set constant to  $k_2 = 10KN/m$ : given the difficulty of the single porosity simulation in characterize the slope of the experimental data compression curve, target values will be normalised over a reference stress  $\sigma_{ref} = 500KPa$ , as shown in Table 4.4. In order to find the best parameters, during uniaxial compression values of vertical stress measured in numerical simulations will be also rescaled over a factor  $\sigma_{res} = \sigma'(e_0)$ . At the end of the process, in order to obtain a stress  $\sigma'(e_0) = 500KPa$  it will be enough to rescale  $k_1$ :

$$k_{2_{NEW}} = k_2 \frac{\sigma_{ref}}{\sigma_{res}}$$

and all other stiffness parameters accordingly. Regarding penetration depth  $\max \delta^i$ , from Table 4.3 the value of  $e_m = 0.45$  and so mass fraction  $\zeta = 0.31$ : reverting Eq. 3.4 and remembering that  $zeta_0 = 0.58$  it holds

$$\delta^i = \frac{\zeta - \zeta_0}{3\zeta_0^2} \simeq 0.123 .$$

Considering now the inter-cluster parameters  $k_1^I, k_2^I, k_c^I$  and  $\delta^I$  they have been defined according to the single porosity simulations:

$$k_1^I = k_2^I \Rightarrow k_c^i = 0, \delta^I = 0 .$$

In order to define their value it has been set

$$k_1^I = 5k_2^i ;$$

this decision has been driven by the fact that considering a cluster as a single entity it has a stiffness higher than the particles composing it: setting inter-cluster stiffness bigger than the intra-cluster one allows to have smaller a overlap between particles belonging to different clusters compared to the overlap of particles belonging to the same cluster and thus a better representation of the cluster as a single entity. Finally for friction parameters,  $\mu^i$  and  $rk_t^i$  will both be tuned, ranging in the interval  $[0, 1]$  while  $\mu^I$  and  $rk_t^I$  will both set to zero in order to allow clusters to deposit compactly. Regarding the radius of a single particle  $r$ , it has been computed starting from the size of the average cluster (i.e. a cluster composed by 50 particles) setting it equal to the average size of a clay

aggregate, from Eq. 4.3. Firstly the relative cluster radius is obtained from Eq. 3.3

$$\hat{R} = R_0 - R_0 \zeta_0 \delta^i = \sqrt[3]{\frac{N}{\zeta_0}} (1 - \zeta_0 \delta^i) = 4.10$$

and the radius  $r$  is then determined as:

$$r = \frac{r^{H_2O}}{\hat{R}} = 13.4 \mu m .$$

Finally as a value for strain rate  $\dot{\epsilon}$  the same value obtained for single cluster compression will be used, while for the number of clusters  $N = 300$  has been set. This value has been set because of computational time limits: considering 50 particles per cluster on average, indeed, leads to a total number of around 15000 particles and a total time of three days for each simulation.

### 4.3.1 Numerical simulation

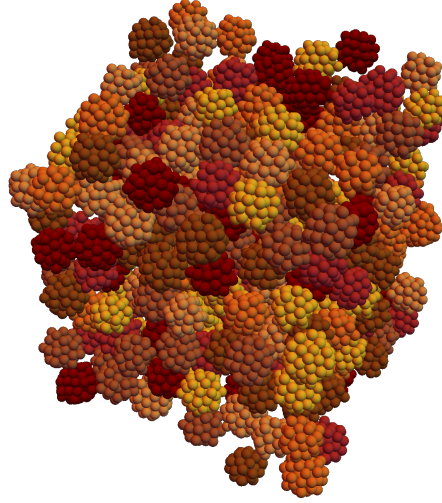


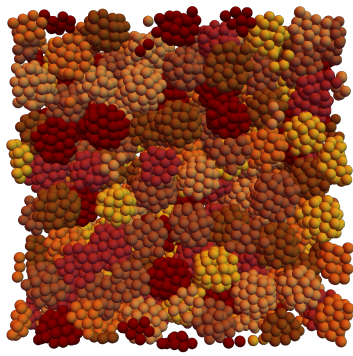
**Figure 4.10:** 3D view of the computational domain.

In this section double porosity numerical simulations results will be studied with particular interest in the comparison of results with the experimental data of Table 4.3. In Figure 4.10 it is possible to see an isometric view of the computational domain; it is important to remember that in the double porosity simulations the domain is defined by periodic boundaries and it has a cubic shape at the beginning of the simulation.

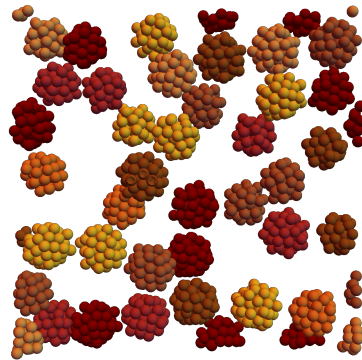
In Figure 4.11 all principal stages of the simulation are shown with a frontal view:

- first row, stage 1: it is possible to see clusters in the initial state; no inter-cluster interactions are present and the domain is in a gas-like state, Figure 4.11a and 4.11b;
- second row, stage 2: jamming point; clusters have got into contact but interaction forces are still low and their shape is still spheroidal, Figure 4.11c and 4.11d;
- third row, stage 3: compaction compression; the system has void ratio  $e \simeq 0.208$  and clusters have changed their shape, Figure 4.11e and 4.11f;
- fourth row, stage 4: relaxation; walls are moved in the opposite direction with a strain rate equal in modulus until  $e = 1.02$ , Figure 4.11g and 4.11h;
- fifth row, stage 5: uniaxial compression; the domain, which is not a cube anymore, is compressed uniaxially in order to simulate the experimental tests until  $e = 0.85$ , Figure 4.11i and 4.11j;

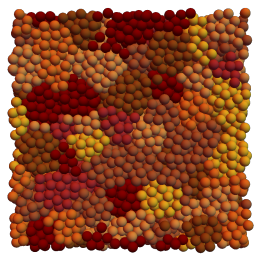
For each stage, moreover, a section is shown, showing only particles placed in a slice of the domain having width  $L = 2r^{H_2O}$ . In order to get the best results, three iterations of GrainLearning were necessary, after which good accordance was found between experimental data and simulations' results. In figure 4.12 the new parameterizations obtained after each iteration are shown: here parameter  $\log_{10} rk_c$  is the base-10 logarithm of  $rk_c$ . In this study, for each iteration of GrainLearning 140 numerical simulations have been run simultaneously. In all three subplots the blue points indicate the numerical values used for the simulations just performed, while the orange ones represent the new parameters with which the numerical simulations will subsequently be launched. For this reason blue points of Figure 4.12b match orange points of Figure 4.12a and blue points of Figure 4.12c match orange points of Figure 4.12b; blue points in figure 4.12a and orange points in 4.12c represent respectively the random starting set of values and the final best set of values. Finally the best three solutions obtained by the third and last iteration are shown in Figure 4.13. As it is possible to notice, this model has much more possibilities in reproducing experimental data, with respect to the single porosity model.



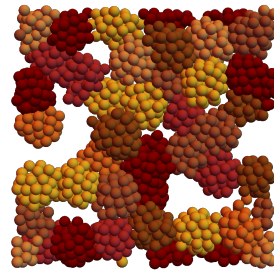
(a) *Front view of stage 1.*



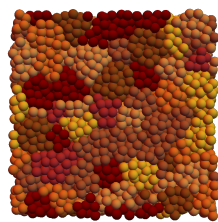
(b) *Section of stage 1.*



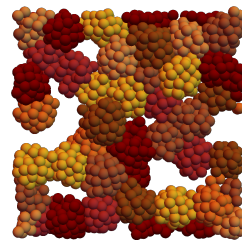
(c) *Front view of stage 2.*



(d) *Section of stage 2.*

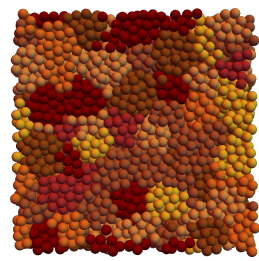


(e) *Front view of stage 3.*

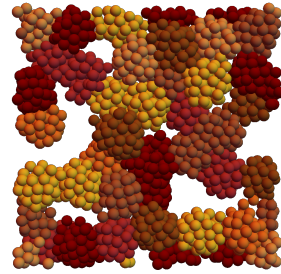


(f) *Section of stage 3.*

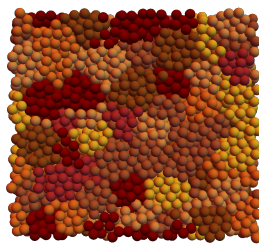
**Figure 4.11:** 3D plot frontal view of compression stages.



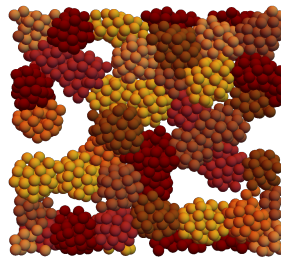
(g) Front view of stage 4.



(h) Section of stage 4.

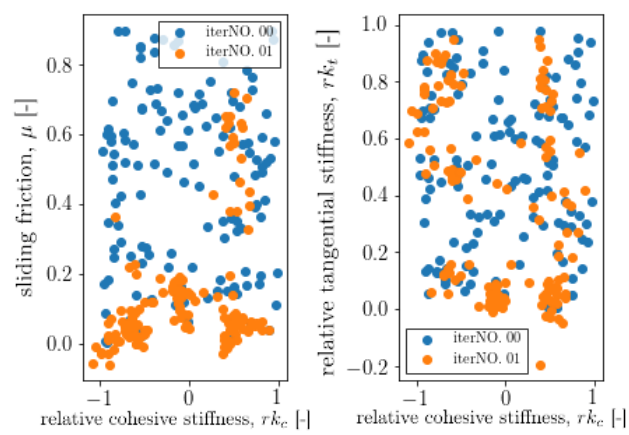


(i) Front view of stage 5.



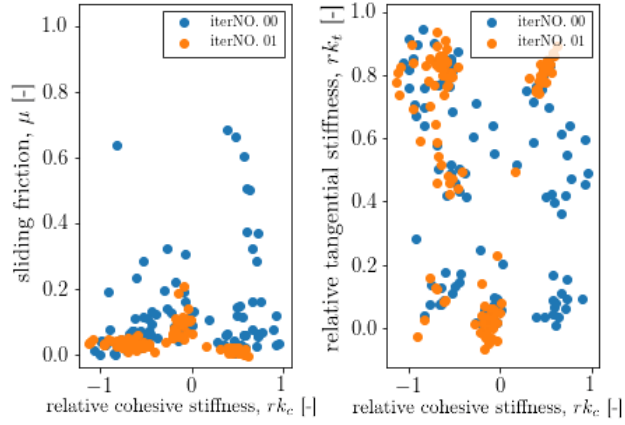
(j) Section of stage 5.

**Figure 4.11:** 3D plot frontal view of compression stages.

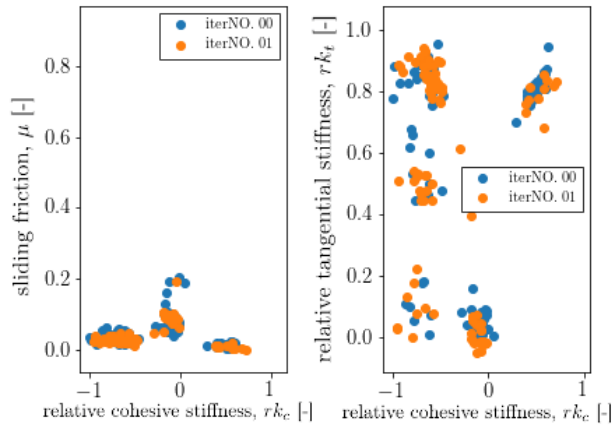


(a) GrainLearning parameter space iteration 1.

**Figure 4.12:** Evolution of parameterization during iteration



(b) *GrainLearning* parameter space iteration 2.



(c) *GrainLearning* parameter space iteration 3.

**Figure 4.12:** Evolution of parameterization during iteration

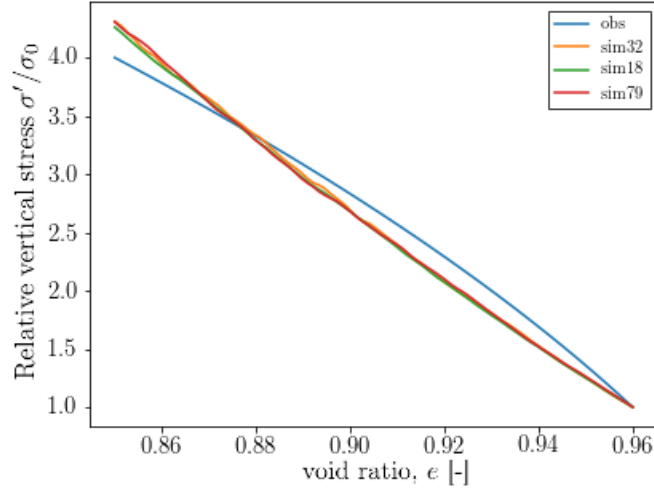


**Figure 4.13:** Results obtained by the third iteration of GrainLearning.

Optimal parameters for this simulation are shown in Table 4.5. It is interesting to notice that  $k_c$  is quite small if compared to other simulation parameters: this is because in order to obtain good results clusters had to be able to deform and so to allow changes in the macro-structure of the computational sample. It is also

**Table 4.5:** Optimal parameters' value, obtained by double porosity calibration.

<i>Simulation parameters</i>	
$rk_c^i$	0.019
$rk_t^i$	0.480
$\mu^i$	0.120
$\frac{\sigma_{res}}{\sigma_{ref}}$	6.114
<i>Relative parameters</i>	
$k_1^i$	327N/m
$k_2^i$	1637N/m
$k_c^i$	30N/m
$k_t^i$	157N/m
$k_1^I$	8185N/m
$k_2^I$	8185N/m
$k_c^I$	0N/m
$k_t^I$	0N/m
$\mu^I$	0

interesting that friction parameters have been set to quite low values (specially sliding friction  $\mu$ ). This is an indication that the compaction of clusters in the jamming point has to be dense in order to get good results. Concluding, it is important to remember that all parameters obtained from the simulation are

not directly relatable to clay physical parameters: taking into account stiffness parameters, for example, it is necessary to remember that they are computational stiffnesses.

### 4.3.2 Results analysis

In Figure 4.14 the whole simulation is showed, displaying variation of  $e$ ,  $e_M$  and  $e_m$ : after the compaction process, the computational sample is relaxed and then uniaxial compression takes place; it is interesting to notice that for low values of vertical stress the change in void ratio  $e$  is caused almost exclusively thanks to the decrease of macro void ratio  $e_M$ , while micro void ratio  $e_m$  remains constant. Furthermore, after relaxation  $e_m$  has a completely elastic recovery, while  $e_M$  exhibits a plastic behavior: this depends on the fact that, after the creation of a cluster, all the interactions present inside it are on the elastic branch of the constitutive model explained in Subsection 2.2.2, having all passed the value  $\delta^*$  during creation. For this reason clusters exhibit the elastic behavior evident in the figure 4.14c; on the other hand this behaviour does not prevent clusters from being deformable, confirmed by the fact that macro void ratio has a plastic behavior. In Figure 4.14b it is shown the detail of uniaxial compression. As noticed previously, there is a good accordance between numerical simulations and experimental data: for this reason in the next section a validation of the numerical method is proposed; proof that it had not been done in the case of single porosity simulations due to the poor agreement between numerical results and computational tests.

## 4.4 Validation: compression of clusters with salt water-like fluid

In this section a validation for the numerical double porosity model exposed before will be provided; in particular, setting the same parameters of the distilled water simulation, a new simulation will be started with the only changes being radius and mass fraction of clusters, tuned in order to resemble the presence of a saline solution as interstitial fluid. Starting from data in Table 4.3 the average value of  $e_m$  in case of saline solution as interstitial fluid is  $e_m = 0.2$ , and so  $\zeta = 0.83$ . Similarly to what has been done for distilled water it holds:

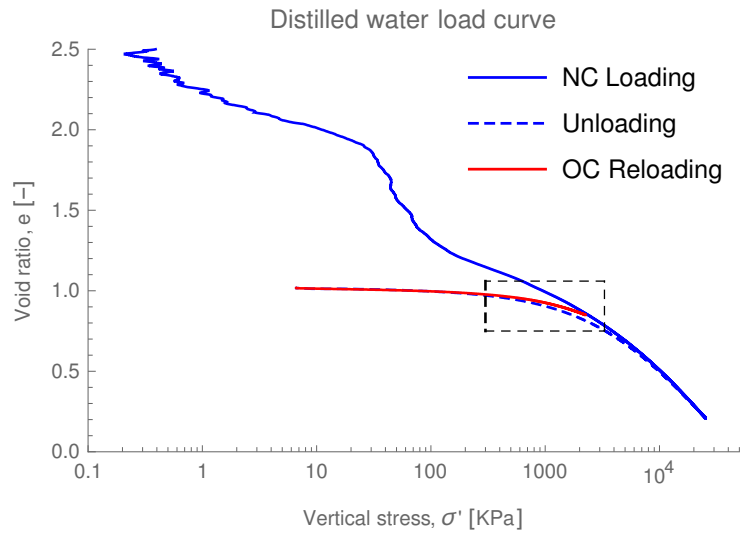
$$\delta^i = \frac{\zeta - \zeta_0}{3\zeta_0^2} \simeq 0.251 .$$

Regarding cluster radius it is already determined and can not be set equal to  $r^{NaCl}$ : the radius of an elementary particle has indeed been determined in the previous simulation and the relative cluster radius is automatically determined from the value of penetration depth  $\max \delta_i$ .

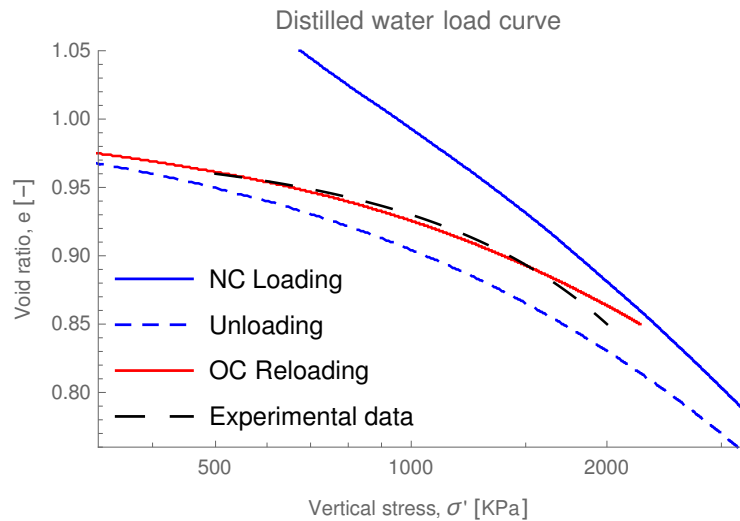
$$\hat{R} = R_0 - R_0\zeta_0\delta^i = \sqrt[3]{\frac{N}{\zeta_0}} (1 - \zeta_0\delta^i) = 3.77 ;$$

fortunately anyway this value is quite similar to the one determined in Chapter 3 given that

$$R = r\hat{R} = 50.6\mu m .$$



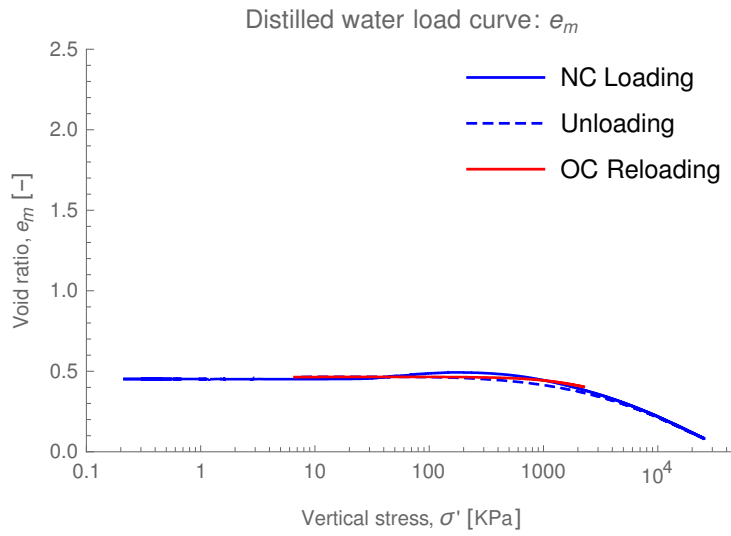
(a) Compression process of distilled water numerical clay sample.



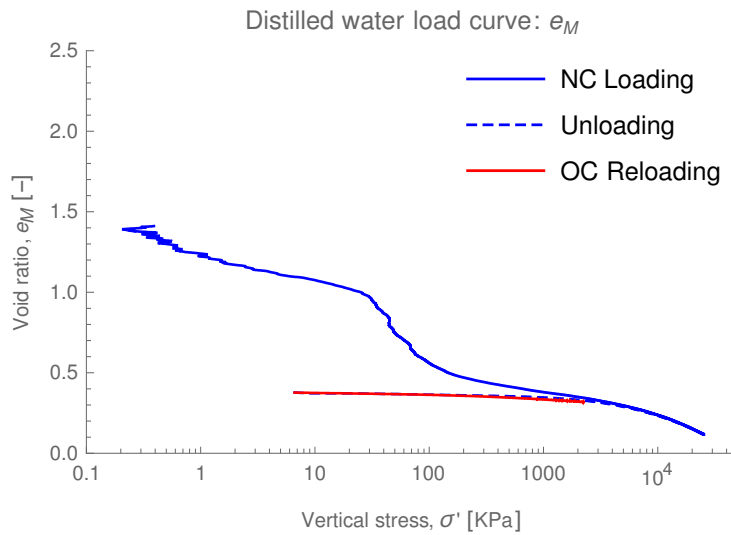
(b) Detail of uniaxial compression stage: comparison with experimental data.

**Figure 4.14:** Distilled water numerical simulation.

All the other parameters are the ones presented in Table 4.5. Results obtained with the numerical simulation are shown in Figure 4.15. As it is possible to see in Figure 4.15b there is a good accordance between experimental data and the numerical simulation of uniaxial compression. Similarly to the case of distilled water, for low values of vertical stress  $e$  is caused almost exclusively by the decrease of macro void ratio  $e_M$ , while micro void ratio  $e_m$  remains constant; moreover one more similarity is given from the fact that micro void ratio is completely elastic, while macro void ratio presents a plastic behaviour, an indication that clusters have undergone deformation following



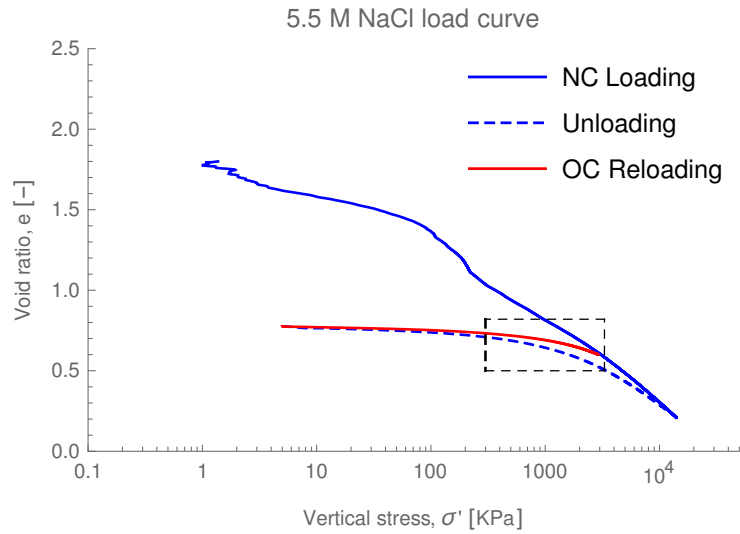
(c) Compression process of distilled water:  $e_m$ .



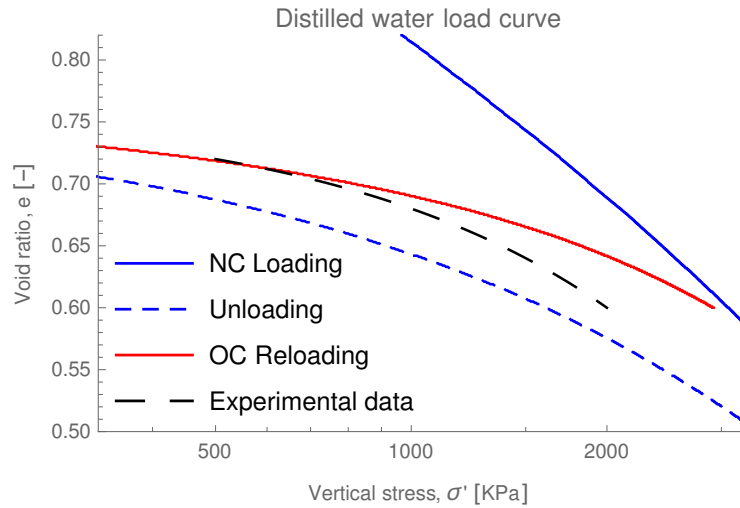
(d) Compression process of distilled water:  $e_M$ .

**Figure 4.14:** Distilled water numerical simulation.

isotropic compression. Given the good reproduction of the experimental results obtained, a set of preliminary analyses where more complex chemo-mechanical histories were imposed to the samples has been run: they are shown in the next chapter. before proceeding with their presentation it is essential to define changes in mechanical behaviour caused by a different interstitial fluid. Comparing the two mechanical compression simulations presented in this chapter, Figure 4.16, it is possible to notice that these simulations are highly influenced by the presence of a different interstitial fluid, in accordance to what has been said in Chapter 1; these differences are highlighted by the values of isotropic compression



(a) Compression process of saline solution numerical clay sample.

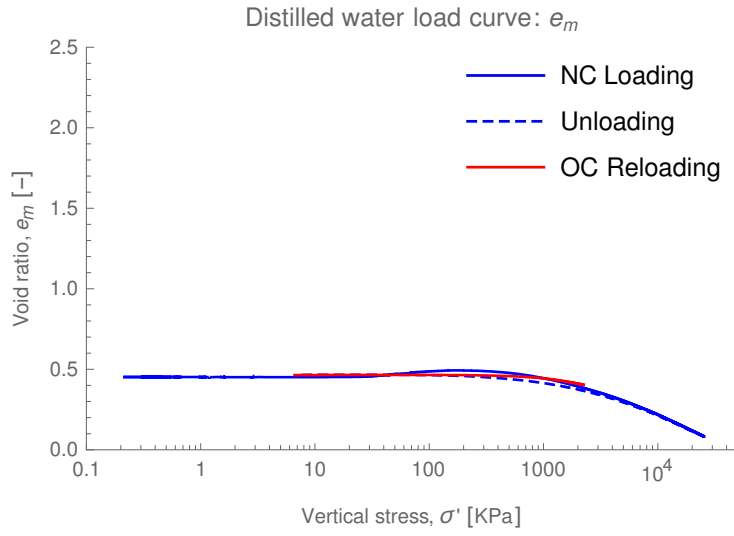


(b) Detail of uniaxial compression stage: comparison with experimental data.

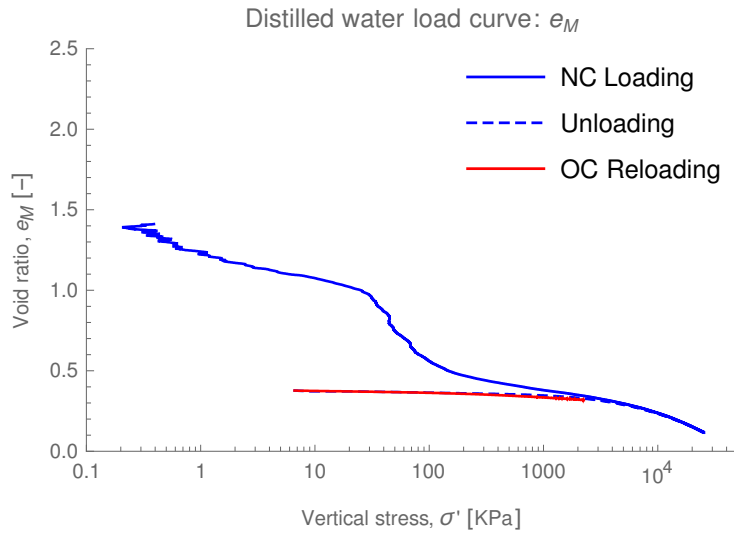
Figure 4.15: Saline solution numerical simulation.

Table 4.6: Comparison between isotropic parameters for *DW* and *NaCl* samples.

<i>sample</i>	$\lambda$	$k$	$N$
<i>DW</i>	0.679	0.076	3.210
<i>NaCl</i>	0.609	0.064	2.739



(c) Compression process of 5.5M NaCl:  $e_m$ .



(d) Compression process of 5.5M NaCl:  $e_M$ .

**Figure 4.15:** Saline solution numerical simulation.

parameters  $\lambda$ ,  $k$  and  $N$  shown in Table 4.6, where  $\lambda$  and  $k$  are respectively normal consolidated and overconsolidated compressibility index:

$$\lambda = -\frac{\Delta e_{NC}}{\log(\Delta\sigma_{NC}) - \log(\sigma_0)}, \quad k = -\frac{\Delta e_{OC}}{\log(\Delta\sigma_{OC}) - \log(\sigma_0)},$$

with  $\sigma_0 = 1\text{KPa}$ , and  $N$  is the known term of the normal compression line  $NCL$ , which is the line obtained from the linear regression of the normal consolidated compression curve in a semi-log scale:

$$e = N + \lambda(\log(\sigma) - \log(\sigma_0)).$$

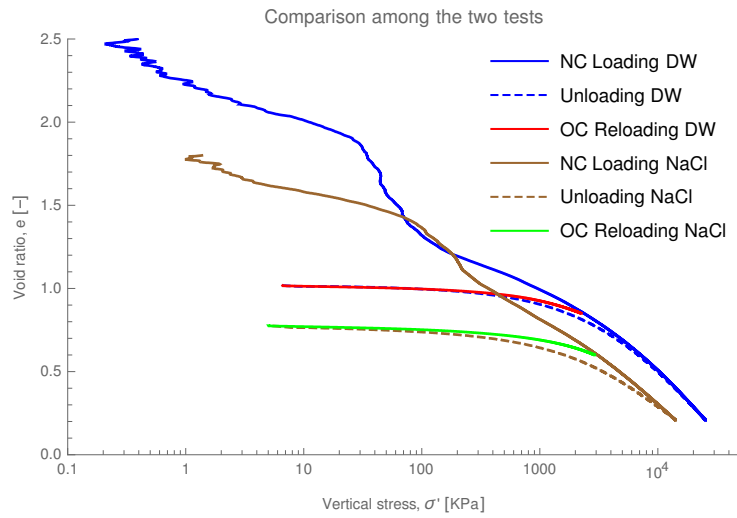


**Figure 4.16:** Comparison of load processes *DW* and *NaCl*.

The comparison between the two normal compression lines  $NCL_{DW}^0$  and  $NCL_{NaCl}^0$  is shown in Figure 4.17: in their notation, subscripts indicates the interstitial fluid present in the sample, while superscript 0 is added to stress the fact that it was also the interstitial fluid with which they were prepared. The complete notation for chemical load samples and their parameters will be stated in Chapter 5 . It is evident, therefore, that following the introduction of a saline solution as

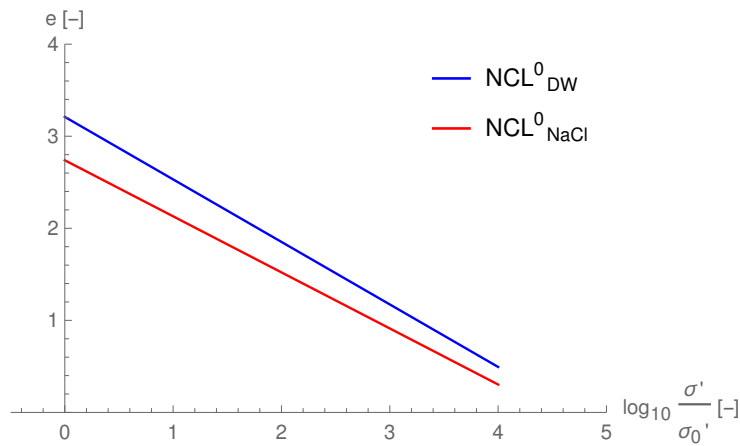


**Figure 4.17:** Comparison between  $NCL_{DW}^0$  and  $NCL_{NaCl}^0$ .

an interstitial fluid, in addition to micro-structural changes, variations on the macro-scale of the material are present, due to the decrease in compressibility  $\lambda$  shown by the *NaCl* sample.

## Chapter 5

# Chemical loading

As seen in Chapter 1, the interstitial fluid has a strong influence in clay behavior: it indeed not only influences double layer thickness and consequently repulsive forces among clay particles, but also the compressibility of the clay. Moreover, a chemical load, i.e. a change in molarity of the interstitial fluid, leads to further complex changes in the behavior of the clay sample during the oedometric compression. Given the good accordance obtained in the simulation of mechanical loads, in this chapter the possibility of characterizing chemical loads will be explored. Before proceeding with the analysis, given that a few different chemical and mechanical computational loading tests will be presented, it is necessary to define a notation that will be consistent throughout the chapter: from now on the completely mechanical tests obtained in Chapter 4 will be defined as *DW* and *NaCl* indicating respectively the distilled water and the 5.5*MNaCl* tests. Regarding the names of chemical load numerical simulations, they will be defined taking into account the following parameters:

- starting configuration: *DW* or *NaCl*;
- sample compression configuration: *NC* for the normal consolidated sample or *OC* for the overconsolidated sample;
- interstitial fluid change: *Sa* for salinisation, i. e. changing from *DW* to *NaCl* or *Des* for the other way around;
- single process or chemical cycle: respectively *Mo* or *Cy*;
- vertical stress measured at the starting of the process in *KPa*.

Moreover, when taking into account compression parameters  $\lambda$ ,  $k$ ,  $N$  and the normal compression line *NCL* This way a process of single salinisation starting from distilled water as interstitial fluid computed on a normal consolidated sample when  $\sigma' = 1600$  will be referred to as *DW\_NC\_Sa\_Mo\_1600*.

In order to characterise changes in the interstitial fluid, in Chapter 4 only one parameter has been changed in the simulation: penetration depth max  $\delta_0$ . In other words, in these simulations, a simple change in the contact model is enough in order to capture micro-structural changes given by a chemical process. For this reason a salinisation process is computed simply increasing or decreasing penetration depth max from  $\delta_0 = 0.123$  to  $\delta_0 = 0.251$  and/or viceversa, being

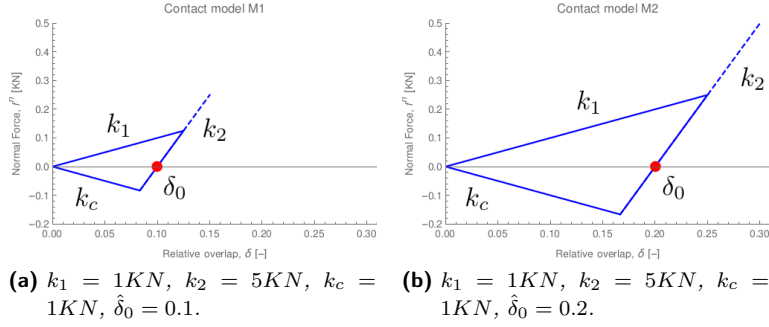


**Figure 5.1:** Contact models M1 and M2.

those the values describing the presence of distilled water and 5.5M NaCl saline solution respectively. In figure 5.1 the two resulting contact models are shown: from this figure it is evident that while  $\delta^i$  changes, all other contact model parameters  $k_1$ ,  $k_2$  and  $k_c$  are kept the same. The process itself of varying  $\delta^i$  is computed as slowly as possible: stopping the compression process ( $\dot{\epsilon} = 0$ ) when the stress is  $\sigma = \bar{\sigma}$ , where  $\bar{\sigma}$  is an arbitrary value, penetration depth max is modified in each iteration as:

$$\delta_{(n+1)}^i = (1 + \alpha)\delta_{(n)}^i$$

where subscript ( $n$ ) refers to the  $n$ -th time step and  $\alpha = \pm 10^{-6}$ , chosen taking into account computational time: this way a single chemical change requires a time of around one day. Finally, in order to keep  $\sigma = \bar{\sigma}$  a new adaptive strain rate  $\hat{\epsilon}$  is applied to the domain in all three directions, defined as:

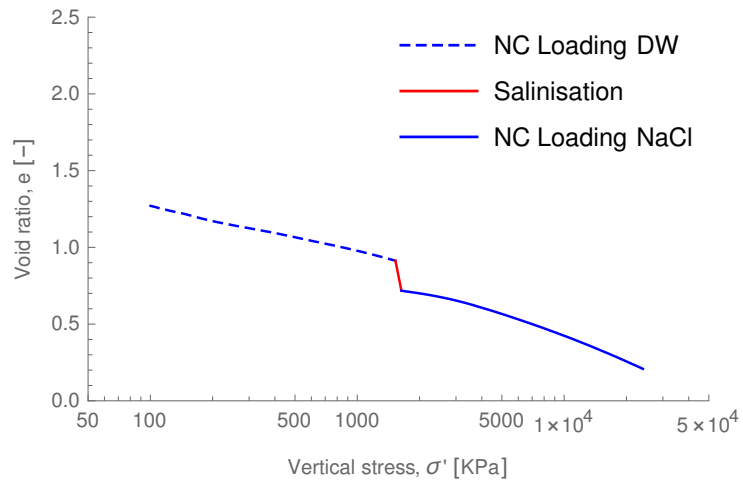
$$\hat{\epsilon}_x = \beta(\sigma_x - \bar{\sigma}_x), \hat{\epsilon}_y = \beta(\sigma_y - \bar{\sigma}_y), \hat{\epsilon}_z = \beta(\sigma_z - \bar{\sigma}_z),$$

where  $\beta = 10^{-7}$  is a gain factor. In the next section single chemical changes will be analysed.

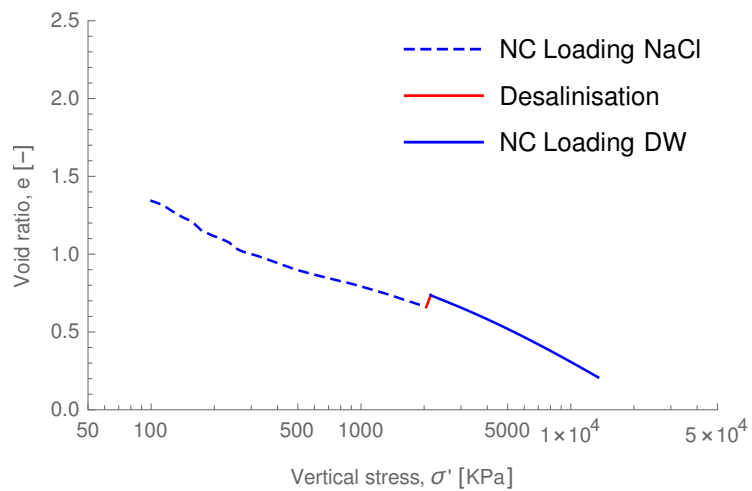
## 5.1 Single chemical load

In this section results obtained from numerical simulations of a single chemical load will be exhibited; in particular a single (and not cyclic) change in molar concentration will be simulated, varying from distilled water to 5.5M NaCl and the other way around. Moreover each one of this processes will be computed for two different values of vertical stress  $\sigma'$ . Four different simulations will then be discussed:

- DW\_NC\_Sa\_Mo\_1600,
- DW\_NC\_Sa\_Mo\_9600,
- NaCl\_NC\_Des\_Mo\_2100,
- NaCl\_NC\_Des\_Mo\_4100



(a) DW\_NC\_Sa\_Mo\_1600



(b) NaCl\_NC\_Des\_Mo\_2100

**Figure 5.2:** Single salinisation and desalinisation processes computed for low stress values on the normal consolidated sample.

**Table 5.1:** Comparison in micro and macro parameters for *DW\_NC\_Sa\_Mo\_1600* and *NaCl\_NC\_Des\_Mo\_2100*.

	<i>DW_NC_Sa_Mo_1600</i>	<i>NaCl_NC_Des_Mo_2100</i>
$\lambda$	0,516	0,711
$k$	0,047	0,067
$N$	2,483	3,152
$\Delta e$	-0,194	0,078
$\Delta e_m$	-0,129	0,074
$\Delta e_M$	-0,016	-0,014
$\sigma_0'$	1633	2149
$\sigma_C'$	2734	2518
$\frac{\sigma_0'}{\sigma_C'}$	1,674	1,172

In Figure 5.2 the salinisation and desalinisation computed at lower stress are shown. A crucial difference can immediately be noticed between them: right after the salinisation process *DW\_NC\_Sa\_Mo\_1600*, Figure 5.2a, shows a seemingly elastic behaviour before connecting back on the plastic path; this behaviour is less noticeable in *NaCl\_NC\_Des\_Mo\_2100*, Figure 5.2b, where the process is almost always plastic. Moreover, there is a difference in the variation of void ratio  $\Delta e$ , this being bigger in the case of salinisation. In order to investigate the reason behind these differences, the changes in the micro and macro parameters were measured: they are shown in Table 5.1. Of particular interest is the comparison between the ratio between the stress value on which the chemical change is computed  $\sigma_0'$  and the value of stress for which the loading can be considered on the plastic path again  $\sigma_C'$ . As expected, the value of  $\sigma_0'/\sigma_C'$  is bigger for *DW\_NC\_Sa\_Mo\_1600*. This results, as will be discussed in the following sections, can be associated with a shift in the yield curve happening during the desalinisation process of *NaCl\_NC\_Des\_Mo\_2100* which instead is absent for *DW\_NC\_Sa\_Mo\_1600*. Moreover, it is interesting to notice that the deformations that occur during desalination are accompanied by a variation in the macro-void ratio of negative (and so opposite) sign, further proof of the plasticity of the phenomenon: with the elastic expansive deformation a plastic compression deformation comes along.

**Table 5.2:** Comparison in micro and macro parameters for *DW\_NC\_Sa\_Mo\_9600* and *NaCl\_NC\_Des\_Mo\_4100*.

	<i>DW_NC_Sa_Mo_9600</i>	<i>NaCl_NC_Des_Mo_4100</i>
$\lambda$	0,534	0,712
$k$	0,046	0,067
$N$	2,554	3,151
$\Delta e$	-0,082	0,071
$\Delta e_m$	-0,071	0,061
$\Delta e_M$	0,004	-0,004
$\sigma_0'$	9680	4135
$\sigma_C'$	10090	4217
$\frac{\sigma_0'}{\sigma_C'}$	1,042	1,020

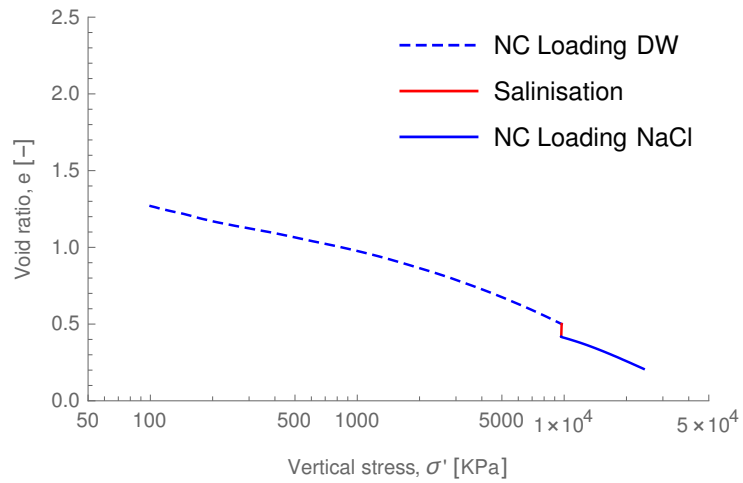
In Figure 5.3 the salinisation and desalinisation computed at higher stress are shown. Considering this two different loading processes, the differences spotted in the previous comparison are less evident; the reason behind this could be that for those values of stress the system is too dense and changes are not well characterised. Values for micro and macro parameters in this confrontation are shown in Table 5.2. Comparing these two simulations  $\sigma_0'/\sigma_C'$  is almost the same in both cases, and both present a change in  $e_M$  in opposite value with respect to  $\Delta e$

## 5.2 Chemical loading cycle on normal consolidated samples

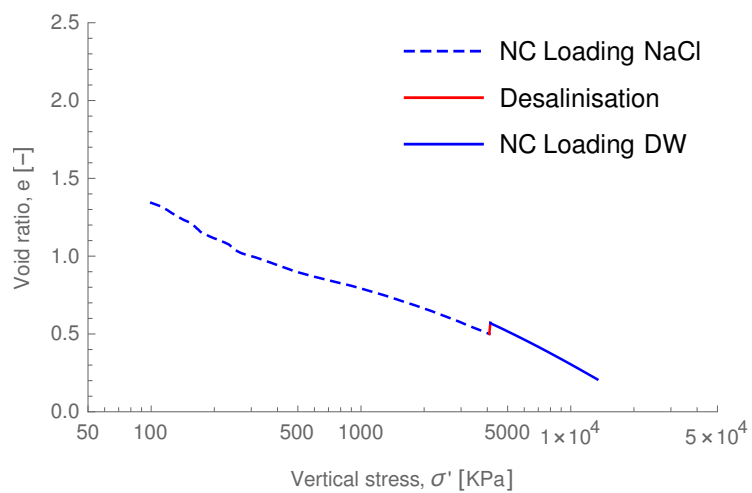
In this section results obtained from numerical simulations of a chemical loading cycle will be exhibited; in particular a double salinisation-desalinisation change in molar concentration will be simulated, varying from distilled water to 5.5M NaCl and back to distilled water, and the other way around. Moreover each one of this processes will be computed for two different values of vertical stress  $\sigma'$ . Four different simulations will then be discussed:

- *DW\_N\_Sa\_Cy\_1100*,
- *DW\_NC\_Sa\_Cy\_10300*,
- *NaCl\_NC\_Des\_Cy\_1800*,
- *NaCl\_NC\_Des\_Cy\_4200*

In Figure 5.4 the salinisation and desalinisation cycles computed at lower stress are shown. Just like the single salinisation processes, a crucial difference can immediately be noticed between them: right after the salinisation cycle *NaCl\_NC\_Des\_Cy\_1800*, Figure 5.4b, shows a seemingly elastic behaviour before connecting back on the plastic path; this behaviour is less noticeable in *DW\_N\_Sa\_Cy\_1100*, Figure 5.4a, where the process is almost always plastic. Given the presence of two chemical change processes it is necessary to define two

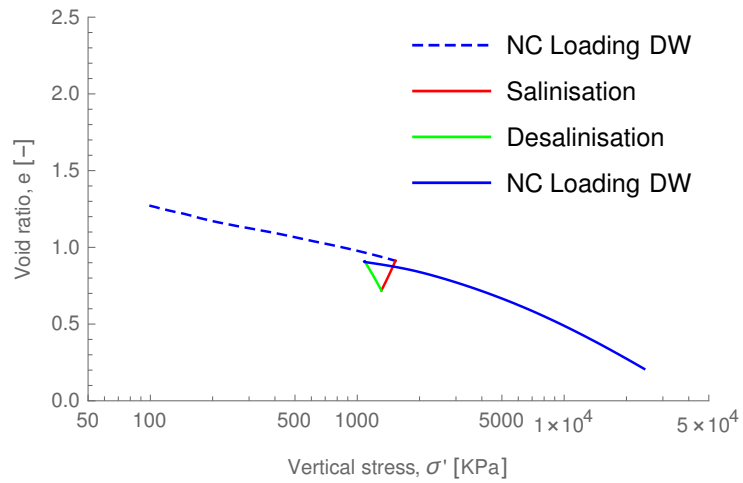


(a) DW\_NC\_Sa\_Mo\_1600

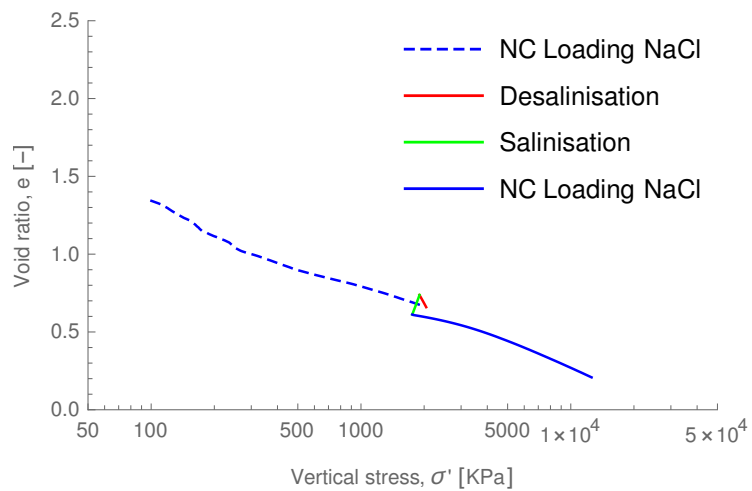


(b) NaCl\_NC\_Des\_Mo\_2100

**Figure 5.3:** Single salinisation and desalinisation processes computed for high stress values on the normal consolidated sample.



**(a)** *DW\_N\_Sa\_Cy\_1100*



**(b)** *NaCl\_NC\_Des\_Cy\_1800*

**Figure 5.4:** Salinisation and desalinisation cycles computed for low stress values on the normal consolidated sample.

**Table 5.3:** Comparison in micro and macro parameters for *DW\_N\_Sa\_Cy\_1100* and *NaCl\_NC\_Des\_Cy\_1800*.

	<i>DW_N_Sa_Cy_1100</i>	<i>NaCl_NC_Des_Cy_1800</i>
$\lambda$	0,658	0,574
$k$	0,072	0,068
$N$	3,113	2,565
$\Delta e^D$	0,19	0,078
$\Delta e_m^D$	0,131	0,074
$\Delta e_M^D$	0,01	-0,014
$\Delta e^S$	-0,194	-0,125
$\Delta e_m^S$	-0,128	-0,09
$\Delta e_M^S$	-0,016	-0,008
$\Delta e$	-0,004	-0,047
$\Delta e_m$	0,003	-0,016
$\Delta e_M$	-0,006	-0,022
$\sigma_0'$	1487	2046
$\sigma_C'$	2661	2818
$\frac{\sigma_0'}{\sigma_C'}$	1,790	1,377

different variations in void ratio:  $\Delta e^S$  will represent the variation obtained during the salinisation process while  $\Delta e^D$  will represent the variation obtained during the desalinisation process and the total change at the end of the process will be defined as  $\Delta e$ . A relevant difference in  $\Delta e$  is evident between the two different samples. In order to investigate the reason behind these differences, the changes in the micro and macro parameters were measured: they are shown in Table 5.3. In this case, the value of  $\sigma_0'/\sigma_C'$  is big for both samples but it is important to notice that for *NaCl\_NC\_Des\_Cy\_1800* the presence of a bigger and seemingly elastic path is confirmed by a lower value of  $\lambda$ . This results, as anticipated in the previous section, can be associated with a shift in the yield curve happening during the desalinisation process of *NaCl\_NC\_Des\_Cy\_1800* which instead is absent for *DW\_N\_Sa\_Cy\_1100*. Moreover, as for the single desalinisation, the deformations that occur during desalination of *NaCl\_NC\_Des\_Cy\_1800* are accompanied by a plastic (negative) variation in the macro-void ratio, further proof of the plasticity of the phenomenon.

**Table 5.4:** Comparison in micro and macro parameters for *DW\_NC\_Sa\_Cy\_10300* and *NaCl\_NC\_Des\_Cy\_4200*.

	<i>DW_NC_Sa_Cy_10300</i>	<i>NaCl_NC_Des_Cy_4200</i>
$\lambda$	0,712	0,538
$k$	0,073	0,069
$N$	3,334	2,419
$\Delta e^D$	0,053	0,071
$\Delta e_m^D$	0,058	0,061
$\Delta e_M^D$	-0,015	0,004
$\Delta e^S$	-0,082	-0,116
$\Delta e_m^S$	-0,071	-0,084
$\Delta e_M^S$	0,004	-0,01
$\Delta e$	-0,029	-0,045
$\Delta e_m$	-0,013	-0,023
$\Delta e_M$	-0,011	-0,006
$\sigma_0'$	10344	4223
$\sigma_C'$	10431	4514
$\frac{\sigma_0'}{\sigma_C'}$	1,008	1,069

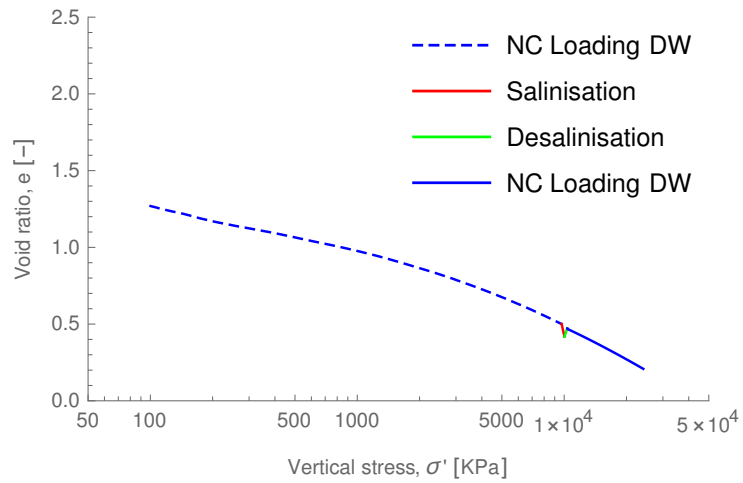
In Figure 5.5 the salinisation and desalinisation cycles computed at higher stress are shown. Considering this two different loading processes, the differences spotted in the previous comparison are less evident for the same reasons made explicit in the previous section. Values for micro and macro parameters in this confrontation are shown in Table 5.4. Comparing these two simulations  $\sigma_0'/\sigma_C'$  is almost the same in both cases, and both present small changes in void ratio.

### 5.3 Chemical loading cycle on overconsolidated samples

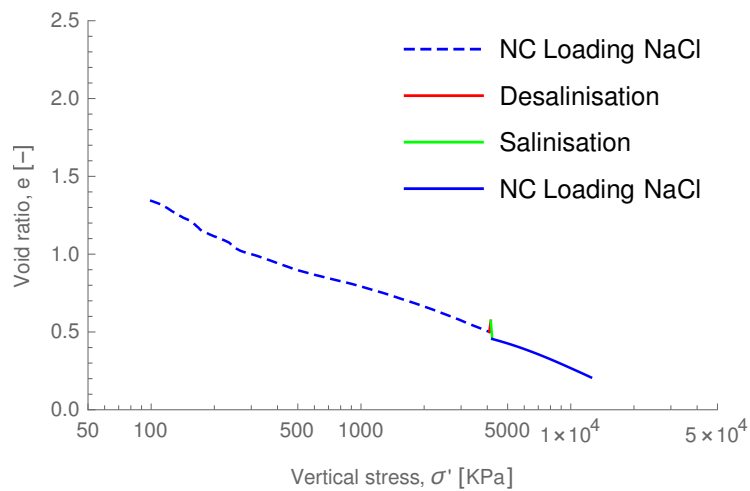
In this section results obtained from numerical simulations of a chemical loading cycle on the overconsolidated samples will be exhibited; in particular a double salinisation-desalinisation change in molar concentration will be simulated, varying from distilled water to 5.5M NaCl and back to distilled water, and the other way around. Two different simulations will then be discussed:

- *DW\_OC\_Sa\_Cy\_1100*,
- *NaCl\_OC\_Des\_Cy\_1100*,

In Figure 5.6 the salinisation and desalinisation cycles are shown. Considering these salinisation cycles, the biggest difference among the confrontations made in this work can be observed. Sample *DW\_OC\_Sa\_Cy\_1100* in fact present the expected behaviour: given that the sample is overconsolidated, the difference in void ratio at the end of the process is very small and the chemical cycle shows an elastic behaviour. On the other hand, after the desalinisation and salinisation cycle of *NaCl\_OC\_Des\_Cy\_1100* the change in void ratio is

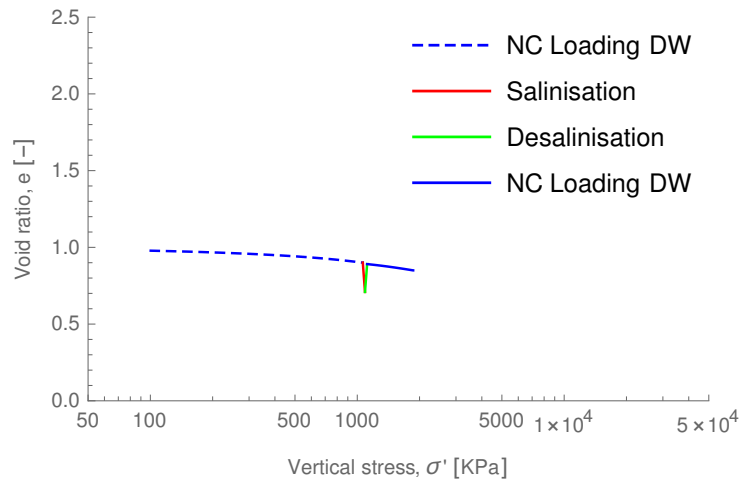


(a) *DW\_NC\_Sa\_Cy\_10300*

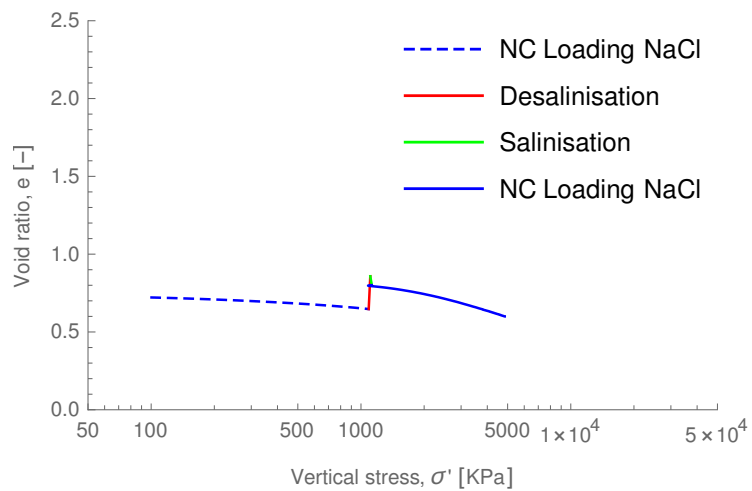


(b) *NaCl\_NC\_Des\_Cy\_4200*

**Figure 5.5:** Salinisation and desalinisation cycles computed for high stress values on the normal consolidated sample.



(a) *DW\_OC\_Sa\_Cy\_1100*



(b) *NaCl\_OC\_Des\_Cy\_1100*

**Figure 5.6:** Salinisation and desalinisation cycles computed for low stress values on the normal consolidated sample.

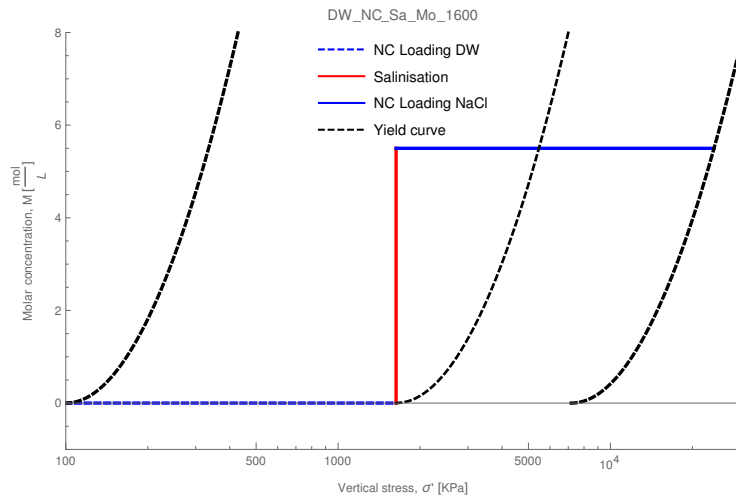
**Table 5.5:** Comparison in micro and macro parameters for *DW\_OC\_Sa\_Cy\_1100* and *NaCl\_OC\_Des\_Cy\_1100*.

	<i>DW_OC_Sa_Cy_1100</i>	<i>NaCl_OC_Des_Cy_1100</i>
$\lambda$	0,658	0,574
$k$	0,072	0,068
$N$	3,113	2,565
$\Delta e^D$	0,181	0,211
$\Delta e_m^D$	0,132	0,16
$\Delta e_M^D$	0,006	-0,002
$\Delta e^S$	-0,191	-0,058
$\Delta e_m^S$	-0,131	-0,098
$\Delta e_M^S$	-0,014	0,052
$\Delta e$	-0,01	0,153
$\Delta e_m$	0,001	0,062
$\Delta e_M$	-0,008	0,054

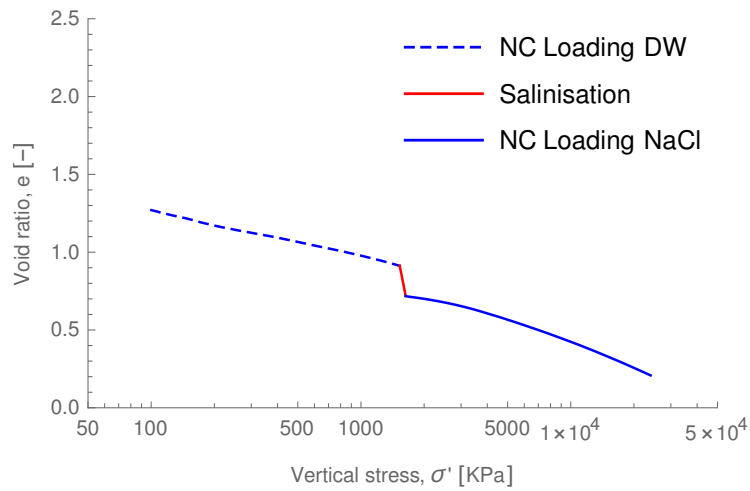
unexpectedly  $\Delta e > 0$ : this effect will not be explained in this work and will be the starting point for further investigations. Changes in the micro and macro parameters were measured: they are shown in Table 5.5: here the ratio  $\sigma_0'/\sigma_C'$  is not taken into account give the wildly unexpected results. Results in Table 5.5 are helpful to highlight the great difference in results obtained: while for *DW\_OC\_Sa\_Cy\_1100*, as expected,  $\Delta e$  is very small, being  $\Delta e = -0,01$ , for *NaCl\_OC\_Des\_Cy\_1100*  $\Delta e = 0,153$ .

## 5.4 Comparison of different numerical and chemical loading paths

In this section a further analysis on the results obtained for chemical loads simulations is carried on. In particular results will be compared with mechanical tests and finally with experimental tests present in literature. Taking into account the behaviour of simulations computed on normal consolidated samples, as anticipated before, there is a difference in the compression process following chemical loadings: in particular while sample *DW\_NC\_Sa\_Mo\_1600* presents an elastic reloading phase after the salinisation process, this is not true for *NaCl\_NC\_Des\_Mo\_2100*, presenting a plastic behaviour right after the desalinisation process. This suggests a qualitative characterisation of the yielding curve as the one proposed in Figure 5.7a: during the salinisation process the loading is not on the yielding curve anymore and for this reason a further mechanical loading is necessary in order to see a plastic behaviour in Figure 5.7b. On the other hand, considering the dual chemical load, i.e. the single desalinisation on a normal consolidated sample, Figure 5.8a shows that in this case the yielding curve is shifted by the desalinisation process and for this reason the loading curve showed in Figure 5.8b presents a completely plastic behaviour. This way of characterising the yielding curve is confirmed by the chemical loading cycles computed on the normal consolidated samples. Considering the *NaCl\_NC\_Des\_Cy\_1800* sample, the elastic phase showed after the chemical

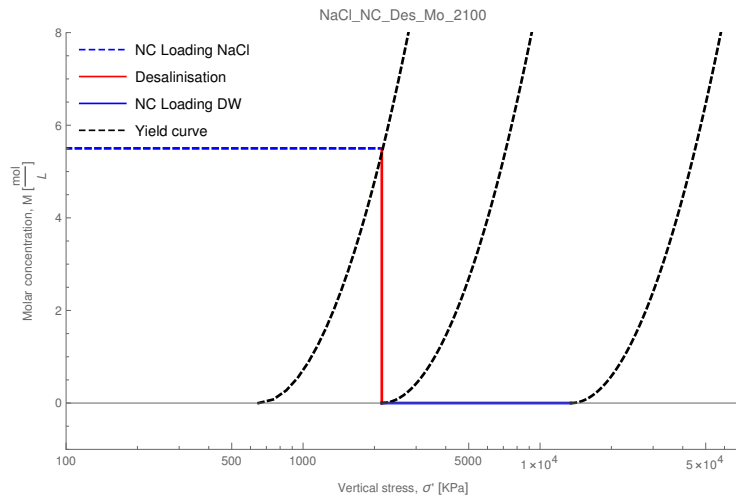


(a) *DW\_OC\_Sa\_Cy\_1100 loading scheme and yielding curve.*

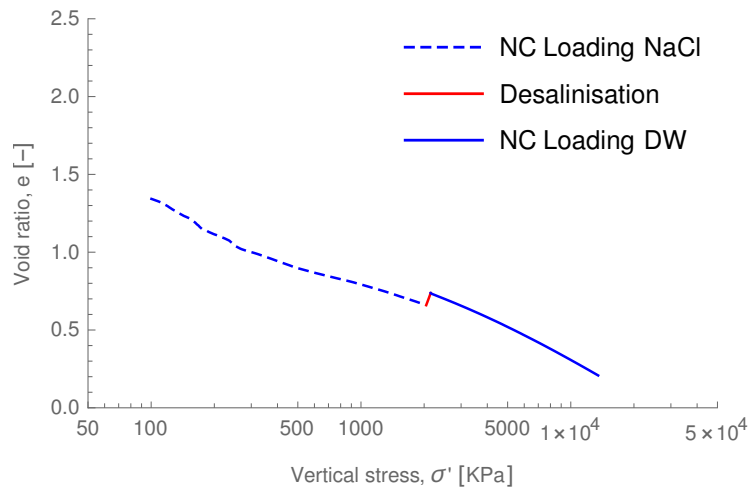


(b) *DW\_OC\_Sa\_Cy\_1100 chemical and mechanical loading curve.*

**Figure 5.7:** *DW\_OC\_Sa\_Cy\_1100 chemical and mechanical scheme and loading curve.*



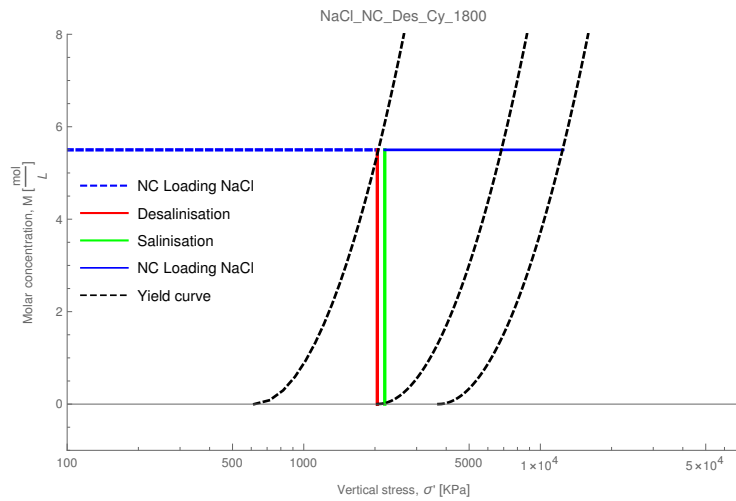
(a) *NaCl\_NC\_Des\_Mo\_2100 loading scheme and yielding curve.*



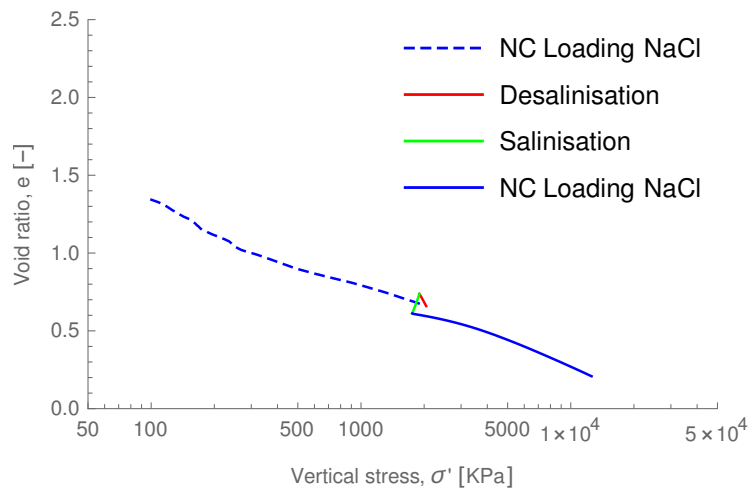
(b) *NaCl\_NC\_Des\_Mo\_2100 chemical and mechanical loading curve.*

**Figure 5.8:** *NaCl\_NC\_Des\_Mo\_2100 chemical and mechanical scheme and loading curve.*

cycle is justified by the shifting of the yielding curve caused by the desalinisation process. For this reason it is necessary a further mechanical load in order to get to the plastic path. The loading scheme and load curve are showed respectively in Figure 5.9a and Figure 5.9b. Once again, considering its dual sample, this behaviour is not present because the chemical cycle does not alter the position of the yielding curve. The loading scheme and load curve are showed respectively in Figure 5.10a and Figure 5.10b. Another very important result that can be noted is the strong influence of the preparation fluid on the numerical results. From now on isotropic compression parameters  $\lambda$ ,  $k$ ,  $N$  and  $NCL$  will be indicated with a subscript and a superscript, defining respectively the interstitial fluid present,  $DW$  or  $NaCl$ , and if it was the preparation fluid, with 0 if no chemical changes were computed, \* if the interstitial fluid is different from the preparation one and 00 if the fluid is the same of the one used during sample preparation but a chemical cycle had been computed. For example  $\lambda_{NaCl}^*$  refers to a sample prepared with distilled water which has undergone a chemical salinisation process. In Figure 5.11a and Figure 5.11b the effect of the preparation fluid can be noticed: after the chemical process, load curves tend to be similar with the mechanical loading test having the same interstitial fluid. This results are coherent with experimental tests exhibited by [3] and showed in Figure 1.12. Concluding, the same behaviour can obviously be noticed on chemical cycle simulations, as shown in Figure 5.12.

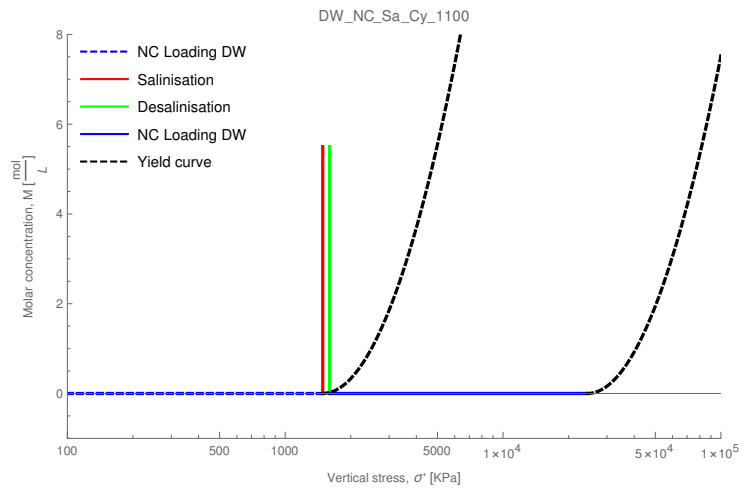


(a) *NaCl\_NC\_Des\_Cy\_1800 loading scheme and yielding curve.*

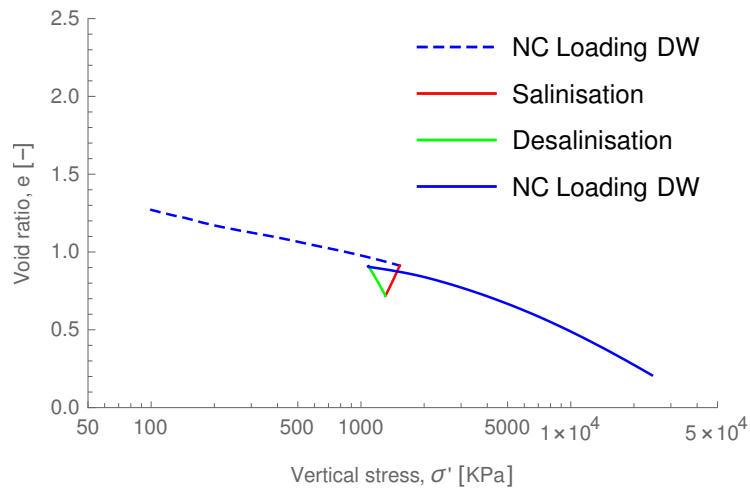


(b) *NaCl\_NC\_Des\_Cy\_1800 chemical and mechanical loading curve.*

**Figure 5.9:** *NaCl\_NC\_Des\_Cy\_1800 chemical and mechanical scheme and loading curve.*

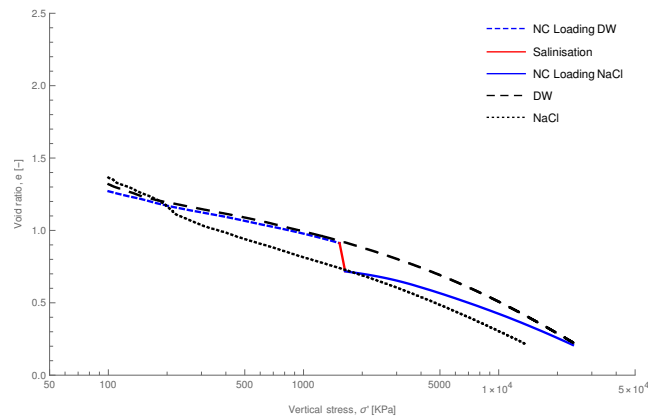


(a) *DW\_N\_Sa\_Cy\_1100 loading scheme and yielding curve.*

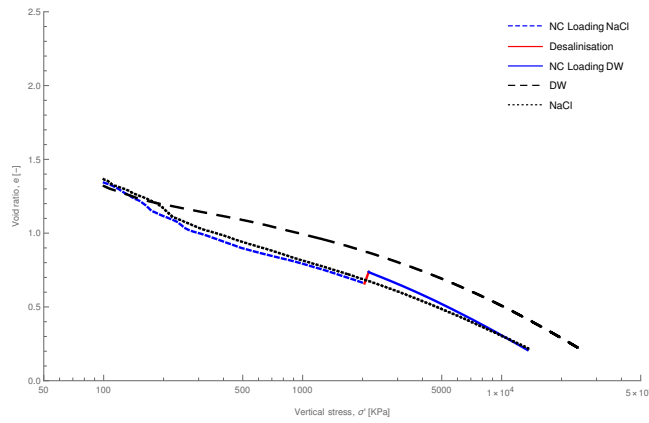


(b) *DW\_N\_Sa\_Cy\_1100 chemical and mechanical loading curve.*

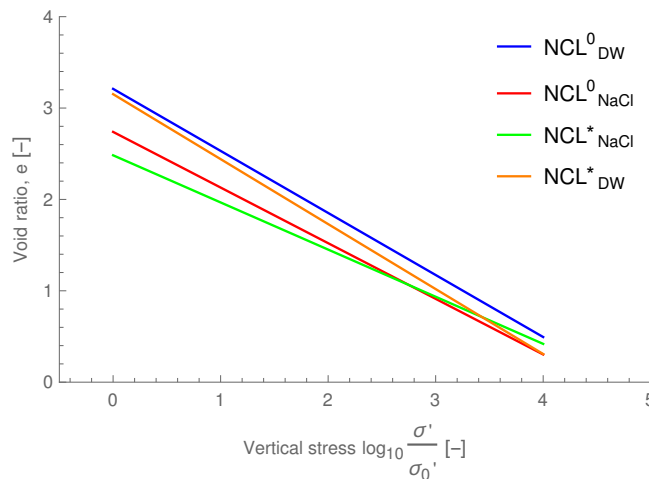
**Figure 5.10:** *DW\_N\_Sa\_Cy\_1100 chemical and mechanical scheme and loading curve.*



(a) Comparison among the mechanical loading tests and DW\_NC\_Sa\_Mo\_1600 sample.

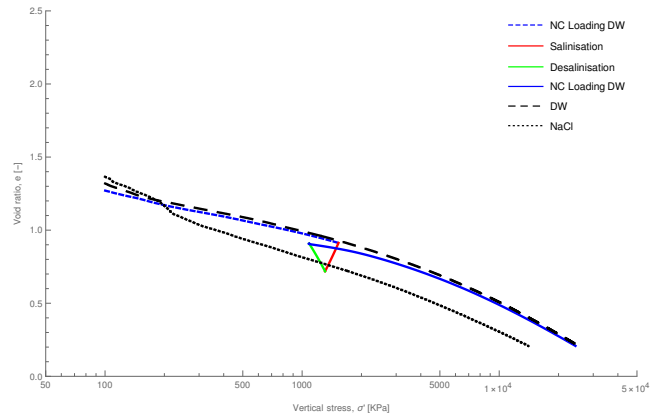


(b) Comparison among the mechanical loading tests and NaCl\_NC\_Des\_Mo\_2100 sample.

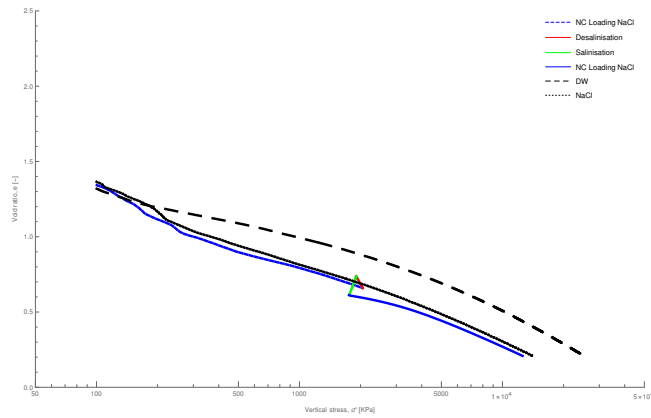


(c) Comparison among the NCL obtained by mechanical loading tests and single chemical change samples.

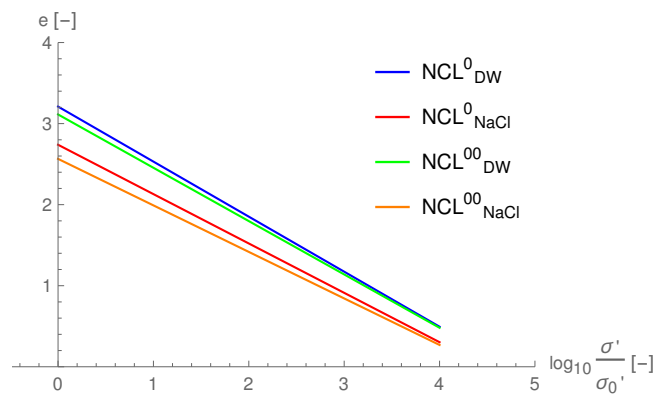
Figure 5.11: Single chemical loads compared with mechanical tests.



(a) Comparison among the mechanical loading tests and DW\_NC\_Sa\_Cy\_1100 sample.



(b) Comparison among the mechanical loading tests and NaCl\_NC\_Des\_Cy\_1800 sample.



(c) Comparison among the NCL obtained by mechanical loading tests and cycle chemical change samples.

Figure 5.12: Cycle chemical loads compared with mechanical tests.

## Chapter 6

# Conclusions and future work

Throughout this study the chemomechanical response of active clays was analyzed; in particular great importance was given to the influence of the interstitial fluid on microstructure, according to the DVLO theory. When immersed in distilled water, repulsive Coulomb forces are present among particles, but the permeation of a saline solution, or more generally of a non-aqueous fluid, with a dielectric constant lower than that of distilled water causes the collapse of the double layer and consequently the reduction of repulsive actions. For this reason great changes can be spotted in the two different configurations. This changes reflect on the macroscopic behaviour of active clays changing not only the size of micro and macro pores but also isotropic compression parameters like the compressibility of the material. This changes on the two scales have been successfully simulated through the Discrete Element Method (DEM). Porous aggregates have been characterised by conglomeration a elementary particles, obtaining in this way a structure that could represent porosity both among and inside clusters. After a calibration phase, good accordance was found between the numerical method and the experimental data. Moreover the method has been validated on a different set of experimental data, obtaining again good results. Finally, thanks to the change of the simple interaction law among particles, chemical changes were simulated, varying the size of pores inside particles agglomerates and consequently agglomerates sizes themselves. Different chemical loads were simulated; the qualitative behaviour obtained by these simulations allowed to characterise a preliminary definition for the yielding curve of the material. Future work will be the ulterior validation of the method on different clay samples, considering also remoduled clays. Moreover while salinisation processes showed a behaviour similar to the one expected from the theory, the same cannot be told regarding chemical loads on overconsolidated samples. This phenomenon will be investigated.

# Appendix A

## MercuryDPM

### A.1 Software overview

MercuryDPM is the code that has been used throughout this work. It is an open source program able to expertly operating both two-dimensional and three-dimensional discrete element simulations, with a user-friendly object-orientated code, written in C++. Simulations can be easily started setting the required specification before calling the *kernel* which runs the simulation: in it, indeed, all the information required and drivers are stored. Some of the specifications that could be set for the simulations are: particles positions, inflows, outflows, contact model, domain dimensions, walls or boundaries, etc.. The main features of the code include:

- User-friendly implementation (C++): the code is made by a series of classes whose usage can be easily understood. This gives the user the possibility to create complex simulations with simple implementations.
- Multiple contact models: Both linear and non-linear contact models are available and each element of the simulation (like particles or even walls) can be characterised by a single and unique specie. Interactions among different species can also be defined (useful when simulating mixtures).
- Built-in geometries: simulating chute flows, rotating drums, periodic boundaries and vibrating walls are just a few examples of the geometries that can be simulated using special classes. Moreover complex walls are available other than simple flat walls: the code indeed supports axial-symmetric, polyhedral and helical screw walls. Finally it is possible for users to define new types of walls themselves.
- Hierarchical grid: a neighborhood search algorithm able to detect interactions among the elements in the simulations with low computational efforts, even in case of elevated size dispersity. This is one of the best features of the code, which makes it unique and gives it its name (the name Mercury comes from the abbreviation of hierarchical grid, hg).
- Statistics package: during the simulation a lot of physical and statistical values can be extracted thanks to the MercuryCG package like density, velocity, structure and stress tensors.

- Access to continuum fields in real time: running the code in live statistics mode allows to have the macroscopic state of the simulation. This could be useful in those simulations in which the behaviour of a component (for example a wall) is determined by the pressure state of the system.
- Handlers: all elements in the simulation (particles, walls, boundaries, etc.) are stored in particular structures called handlers; this way all particles and all the information regarding them are stored in the *particleHandler*, walls in the *wallHandler* and so on. Thanks to this storage system the creation of new objects is simple and all objects of the same type are stored together even if their properties are different.
- Self-test suite and demos: the code can be tested with more than a hundred drivers which are useful both for checking the installation and as a tutorial and guide for beginner users.
- Simple restarting: it is possible to generate restart files that give the possibility to restart the simulation without compiling again in case of unexpected breaks of the simulation. This kind of files contain all information regarding the code: if a small modification has to be made in the code (for example changing a density value) the simulation can be easily restarted.
- Interface to other particle simulation codes: thanks to the restarting interface, external data can be also loaded in the simulation, such as: data from other DEM codes, data from molecular dynamics codes or even experimental data. They can then be post-processed with the MercuryCG tool.
- Visualisation: the output can be easily visualized by external programs like *Paraview*.

Finally a simple example of a code simulating a particle bouncing on a wall is showed. The implementation process inside MercuryDPM is quite simple: inside the method *setupInitialCondition* a spherical particle and a wall are placed inside the domain, while inside the *main* function general properties are set, such as domain's dimensions, time step and output settings. The simulation starts with *problem.solve()*.

**Listing A.1:** Simple code demo.

```

///[T3:headers]
#include <Species/LinearViscoelasticSpecies.h>
#include <Mercury3D.h>
#include <Walls/InfiniteWall.h>
///[T3:headers]

///[T3:class]
class Tutorial3 : public Mercury3D
{
public:

    void setupInitialConditions() override {
        SphericalParticle p0;
        p0.setSpecies(speciesHandler.getObject(0));
        p0.setRadius(0.005);
    }
};

```

```

    p0.setPosition(Vec3D(0.5 * getXMax(), 0.5 * getYMax(), getZMax()));
    p0.setVelocity(Vec3D(0.0, 0.0, 0.0));
    particleHandler.copyAndAddObject(p0);

    ///! [T3:infiniteWall]
    InfiniteWall w0;
    w0.setSpecies(speciesHandler.getObject(0));
    w0.set(Vec3D(0.0, 0.0, -1.0), Vec3D(0, 0, getZMin()));
    wallHandler.copyAndAddObject(w0);
    ///! [T3:infiniteWall]
}

};
///! [T3:class]

int main(int argc, char* argv[])
{
    // Problem setup
    Tutorial3 problem;

    problem.setName("Tutorial3");
    problem.setSystemDimensions(3);
    problem.setGravity(Vec3D(0.0, 0.0, -9.81));
    problem.setXMax(1.0);
    problem.setYMax(1.0);
    problem.setZMax(2.0);
    problem.setTimeMax(5.0);

    ///! [T3:speciesProp]
    // The normal spring stiffness and normal dissipation
    // is computed and set as for collision time tc=0.005
    // and restitution coefficient rc=1.0,
    LinearViscoelasticSpecies species;
    species.setDensity(2500.0); //sets the species type_0 density
    species.setStiffness(258.5); //sets the spring stiffness.
    species.setDissipation(0.0); //sets the dissipation.
    problem.speciesHandler.copyAndAddObject(species);
    ///! [T3:speciesProp]

    problem.setSaveCount(10);
    problem.dataFile.setFileType(FileType::ONE_FILE);
    problem.restartFile.setFileType(FileType::ONE_FILE);
    problem.fStatFile.setFileType(FileType::NO_FILE);
    problem.eneFile.setFileType(FileType::NO_FILE);

    problem.setXBallsAdditionalArguments("-solidf_v0");
    problem.setWallsWriteVTK(true);
    problem.setParticlesWriteVTK(true);

    problem.setTimeStep(0.005 / 50.0); // (collision time)/50.0
    problem.solve(argc, argv);

    return 0;
}

```

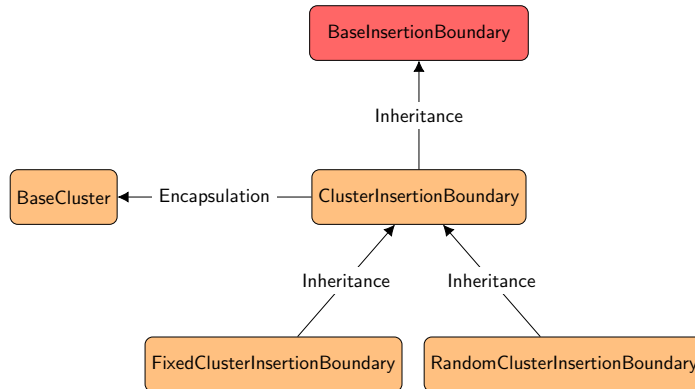


**Figure A.1:** Structure of the classes needed for the cluster implementation (in orange); *BaseInsertionBoundary* (in red) is an already existing MercuryDPM class.

## A.2 Implementation of the cluster creation process inside MercuryDPM

As a starting point for this work, the possibility to create a cluster has been implemented inside the MercuryDPM software. In accordance with the structure of the program, the insertion of clusters inside a domain is provided by an insertion boundary which is a sub-domain from which entities are inserted. In this way, if a starting velocity is set a flow of clusters can be created. Otherwise, if a fixed amount of cluster is needed, the user can specify positions and velocities for the insertion. In order to do so four classes have been created:

- *BaseCluster.h*: it is the core of the implementation and defines the process of cluster creation;
- *ClusterInsertionBoundary.h*: inherits from *BaseInsertionBoundary*, a base class of MercuryDPM, and defines the process of cluster insertion. An object of type *BaseCluster* is encapsulated in it;
- *RandomClusterInsertionBoundary.h*: this class, which derives from *ClusterInsertionBoundary.h* takes into account the random process necessary to the random insertion of clusters inside the domain;
- *FixedClusterInsertionBoundary.h* similarly to the previous one, this class derives also from *ClusterInsertionBoundary.h* and takes into account the process necessary to the insertion of clusters inside the domain in some specified positions.

A scheme of the architecture among these classes is shown in Figure A.1. In order to create a cluster just a few information are needed and they can be prescribed within function *set*, as can be seen in the snip of code reported below, in which the usage of *RandomClusterInsertionBoundary.h* is shown. Firstly, a Particle has to be created (*insertionBoundaryParticle*) and it will be used as a model for elementary particles composing the cluster: all physical properties will be copied from it; the second parameter in function *set* is *maxFailed*: it is a counter

which defines how many times the program will try to insert a cluster inside the simulation, checking that there are no interactions. After that the user has to specify minimum and maximum of domain, velocity and radius.

**Listing A.2:** Random Cluster Settings

```
void setupInitialConditions() override {
    SphericalParticle insertionBoundaryParticle;
    insertionBoundaryParticle.setSpecies(
        speciesHandler.getObject(0));

    CubeInsertionBoundary insertionBoundary;
    insertionBoundary.set(&insertionBoundaryParticle, maxFailed,
        getMin(), getMax(),
        velocityMin, velocityMax,
        radiusMin, radiusMax);
    boundaryHandler.copyAndAddObject(insertionBoundary);
}
```

If differently a fixed number of cluster is needed it is necessary to specify their positions and radii using *FixedClusterInsertionBoundary.h*, while there is no need anymore for the dimension of the boundary.

**Listing A.3:** Fixed Cluster Settings

```
void setupInitialConditions() override {
    SphericalParticle insertionBoundaryParticle;
    insertionBoundaryParticle.setSpecies(
        speciesHandler.getObject(0));

    CubeInsertionBoundary insertionBoundary;
    insertionBoundary.set(&insertionBoundaryParticle, maxFailed,
        positions, radii,
        velocityMin, velocityMax);
    boundaryHandler.copyAndAddObject(insertionBoundary);
}
```

If no velocity is specified, it will be automatically set to zero.

## Appendix B

# GrainLearning toolbox

Granular materials are characterised by a high number of particles and so of degrees of freedom; during compression tests this leads to wildly nonlinear behaviour, difficult to characterise. Moreover compression test results are often history dependent, adding another issue to an already complex matter. Fortunately Discrete Element Method (DEM) represent a valid tool in order to simulate granular material behaviour. Differently from continuum mechanics approach, like Finite Elements Method (FEM) for example, which need to be coupled with complex contact model in order to characterise efficiently the behaviour of granular materials, in DEM every microscopic and macroscopic value is easily accessible, and contact models behind it can be surprisingly simple. On the other hand the disadvantage of this numerical method is that, even if particles are defined with stiffness and friction, which are macroscopic parameters, these does not match any physical value in the actual material being simulated. They are indeed only numerical parameters and don't represent any macroscopic property. For this reason, the process of defining DEM parameters can be quite challenging. GrainLearning is a valid toolbox in order to avoid this problem [7]. Thanks to an iterative Bayesian filter and starting from results obtained with random parameter values, the best value for parameters can be obtained computing posterior distribution of the model, based on the accordance obtained by results with target data. For example starting from experimental results of oedometric compression tests stress, it is possible to define numerical parameters like stiffnesses, friction or even particle size dispersity. After each iteration of a DEM simulations set, parameter space, initially uniformly distributed, is updated, in order to define high probability parameter values. In Figure B.1 a scheme of Grain learning iterative process is shown. The hole idea behind the model is to define the posterior probability of parameter values starting from the expected value for probability:

$$E[f_t(x_t)|t_t] = \int f_t(x_t)p(x_t|y_t)ddx$$

where  $f_t$  is a  $p(x_t|y_t)$ -integrable function that describes a value of interest for the simulations, typically compared to experimental data,  $x_t$  represent augmented probabilities and  $y_t$  represents measurements. After computing the new probability parameter space, DEM simulations are computed again according to these values. Typically three iterations required to reach convergence; moreover

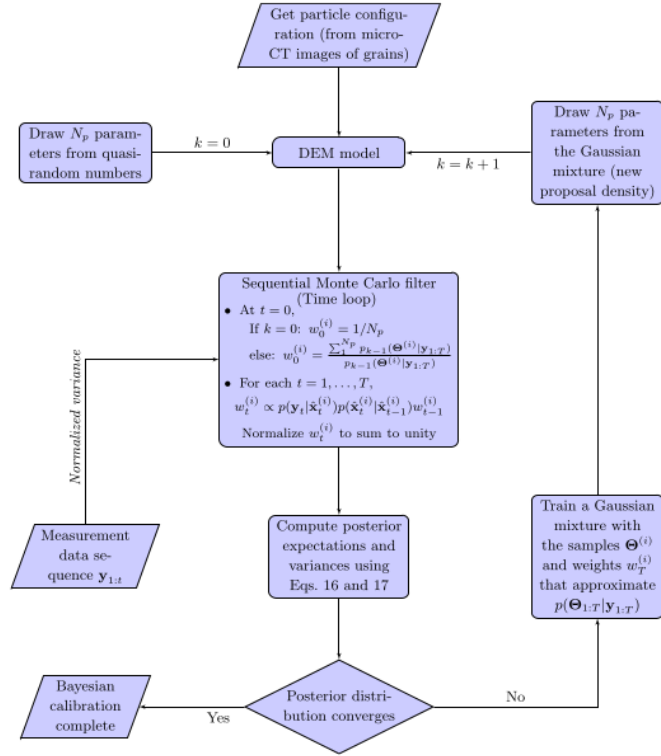


Figure B.1: Scheme of Grain learning iterative process. [7]

the beauty of this tool stands in the fact that if no improvement is found on the parameter space, it is highly likely that the chosen parameters are not able to reproduce the target values. Finally in Figure 4.12 an example of the iterating process effect on parameter space is shown.

# Bibliography

- [1] MercuryLab B.V. *The Fundamentals of Discrete Particles Simulations*. 2017.
- [2] Mařín D. “Double structure hydromechanical coupling formalism and a model for unsaturated expansive clays”. In: *Engineering Geology* (2013).
- [3] C. Di Maio. “Exposure of bentonite to salt solution: osmotic and mechanical effects”. In: *Géotechnique* (1996).
- [4] Castellanos E., Villar M.V., and Gens A. Romero E. Lloret A. “Chemical impact on the hydro-mechanical behaviour of high-density FEBEX bentonite”. In: *Physics and Chemistry of the Earth* (2008).
- [5] Musso G., Romero E., and Dellavecchia G. “Double-structure effects on the chemo-hydro-mechanical behaviour of a compacted active clay”. In: *Géotechnique* (2013).
- [6] Musso G. et al. “The role of structure in the chemically induced deformations of FEBEX bentonite”. In: *Applied Clay Science* (2003).
- [7] Cheng H. et al. “An iterative Bayesian filtering framework for fast and automated calibration of DEM models”. In: *ScienceDirect* (2019).
- [8] J. K. Mitchell and K. Soga. *Fundamentals of Soil Behaviour*. 2005.
- [9] in press Orefice L. “Clusters: generalities and structure properties”. In: (2020).
- [10] C. O’Sullivan. *Particulate Discrete Element Modelling*. Spon Press, 2011. ISBN: 9780415490368.
- [11] F. Radjai and F. Dubois. *Discrete-element Modelling of Granular Materials*. Wiley, 2011. ISBN: 9781848212602.
- [12] K. Taghizadeh, G. Combe, and S. Luding. *ALERT Doctoral School 2017*. 2017.
- [13] Beichuan Y. “Definition and Symmetry of Averaged Stress Tensor in Granular Media and its 3D DEM Inspection Under Static and Dynamic Conditions”. In: *International Journal of Solids and Structures* (2018).

# Acknowledgements

My gratitude goes to Professors Guido Musso and Vanessa Magnanimo for the constant support provided during the development of this project, both professional and personal.

My heartfelt thanks to my family, always supporting my choices and always by my side during my academic career.

Lastly a thought goes to those who shared this path with me, making it unforgettable.